ABSTRACT

Title of dissertation: LIQUID SODIUM MODEL OF EARTH'S OUTER CORE

Woodrow Shew, Doctor of Philosophy, 2004

Dissertation directed by: Professor Daniel P. Lathrop
Department of Physics

Convective motions in Earth's outer core are responsible for the generation of the geomagnetic field. We present liquid sodium convection experiments in a spherical vessel, designed to model the convective state of Earth's outer core. Heat transfer, zonal fluid velocities, and properties of temperature fluctuations were measured for different rotation rates Ω and temperature drops ΔT across the convecting sodium.

The small scale fluid motion was highly turbulent, despite the fact that less than half of the total heat transfer was due to convection. The typical length scale of convective motions decreases with rotation rate like $\Omega^{-1/3}$. These convective structures give rise to temperature fluctuations which decrease in amplitude with increasing rotation rate and grow linearly with the temperature drop; $\sigma_T \sim \Omega^{-1/3}\Delta T$. Convective heat transfer was observed to increase with both temperature drop and rotation rate proportional to $\Omega^{1/3}\Delta T$. Retrograde zonal velocities were measured at speeds up to 0.02 times the tangential speed of the outer wall of the vessel. These velocities scale linearly with rotation rate and imposed temperature gradient; $U_\phi \sim \Omega\Delta T$. Power spectra of temperature fluctuations exhibit a well defined knee at a frequency which is characterized by ballistic velocities. The knee frequency is thought to be associated with the convective motions (i.e. the energy injection scale for the underlying fluid motion). We observe a sensitive dependence of heat flux on an applied magnetic field: heat transfer concentrates in the equatorial region with an applied magnetic field parallel to the rotation axis.

In the context of Earth's outer core, our observations imply a thermal Rayleigh number $Ra = 10^{22}$ and a convective velocity near 10^{-5} m/s. There is likely a knee in the energy spectrum

of outer core fluid motions associated with convective length and time scales of 100 m and 2 days. Heat flux measurements suggest that persistent inhomogeneity in the geomagnetic field may cause inhomogeneities in the formation of the inner core.

LIQUID SODIUM MODEL OF EARTH'S OUTER CORE

by

Woodrow Shew

Dissertation submitted to the Faculty of the Graduate School of the
University of Maryland, College Park in partial fulfillment
of the requirements for the degree of
Doctor of Philosophy
2004

Advisory Commmittee:

Professor Daniel P. Lathrop, Chair/Advisor
Professor Peter Olson
Professor Thomas Antonsen
Professor Wolfgang Losert
Professor James Wallace, Deans Representative

ACKNOWLEDGMENTS

I owe a debt of gratitude to a great number of people, who have stood by me and helped me over the last several years. First and foremost, I would like to thank my lovely fiancee Rachel. No more than one week after I defend this dissertation she will graciously and mercifully take my hand in marriage. Not only did she help with editing my dissertation and keep me calm during the rather frequent anxious moments in the 2 months prior to my defense, but she also nearly single-handedly planned our wedding. Next I would like to thank my sister, father, and mother. Still today, I apply the knowledge that I learned in my fifth grade science project on the Bernoulli principle (largely motivated by my mom). Its good to get started in fluid dynamics at a young age. I'm certain that access to my dad's workshop and junkpiles cultivated my experimentalist tendencies. As for my sister, she reminded me that it's possible to work 65 hour weeks when necessary and still make time for exercise, so that I remain sane. I would also like to thank the following people for the following things:

Nate	boxed wine, boxing, poker, golf, mad editing skills
Colin	general rabblerousing
Matt	discussions of love and organic food
Brad	newfound respect for government agents
Philippe	an occasional ribbing
Bhavana	yogic flying lessons
Karl	very helpful discussions of time-travel
Frits	marrying Rachel and I
Nat	mon seulement ami en France
cousin Andy	plumbing tips
Peace corps people	keeping Rachel in line
Americorp people	keeping Rachel in line

I would also like to thank a handful of people who have more directly contributed to the work presented in this dissertation. First on this list is, of course, Dan Lathrop. In a broad sense, Dan has impacted my life immeasurably. Because of his advice and by his example I have learned enough that I am ready and excited for a career in experimental physics. Without Dan, I may not have realized that, when presented with a decision in life, there are almost always three options: one which is pretty reasonable, one which kind of sucks, and one which is totally impossible. He had a knack for making clear which was the first option. I am also grateful to count him as a friend. I thank Don Martin for two things. First, nearly all of my skills in the machine shop originated with a lesson from Don. Second, he machined, welded, soldered, and plumbed many of the essential parts of the experimental apparatus. The presented work would not have been possible without Don. I thank Nicolas Gillet for several helpful discussions and for providing me with numerical calculations of critical onset parameters. I thank Morgan Varner for constructing the magnet coils and the heater frame. I am grateful to Fred Cawthorne for his borderline-supernatural ability to debug electronics. I thank Zahir Daya for helpful conversations and notes about the Grossmann-Lohse theory for Rayleigh-Benard convection. I also owe all of my labmates thanks for helpful discussions and interesting lunch-time controversies.

I would also like to acknowledge the financial support of the National Science Foundation. This work was supported by the Geophysics Program and Earth Sciences Instrumentation Program.

TABLE OF CONTENTS

LIST OF FIGURES

Chapter 1

INTRODUCTION AND BACKGROUND

Fluid motions in Earth's outer core have a direct effect on several prominent features of our planet. Transfer of angular momentum between the core liquid and the mass lying above it may induce changes in the rotation rate of Earth, i.e. the length of day. Persistent spatial inhomogeneity in heat transfer due to outer core flow dynamics may be reflected in the behavior of the mantle, which may in turn affect the motion of the crust, i.e. plate tectonics. Perhaps most interesting, liquid motion in the outer core underlies the existence of Earth's magnetic field. It is likely that the dramatic reversals of the magnetic poles, as well as other magnetic field dynamics are tied to core fluid motions. The experiments described in this dissertation are motivated by the need for a better understanding of the dynamics of Earth's liquid outer.

The discussions in this chapter will be structured as follows. First, the interior of the Earth will be described in some detail, focusing on the fluid outer core. In the next section, we will discuss similarities and differences between the outer core and the experiments presented in this dissertation. Then, a review will be presented of previous centrifugal convection experiments and some congruent numerical and analytical work. Finally, a brief outline will be given of the remaining chapters.

1.1 Earth's interior and its magnetic field

How do we know the state of the inaccessible depths of Earth's interior? As of 2003, the deepest a person has ever ventured into Earth's core is 3585 meters in the East Rand mine of South Africa, a mere 5/1000 of the way to Earth's center. Knowledge of the deeper reaches has been obtained only by indirect means. For example, one may deduce that the Earth's density is inhomogeneous with the following reasoning. The mass of the Earth can be deduced from its orbital motion through the solar system; it is $5.97 \times 10^{24}\ kg$. The average density of rocks in the crust varies from 2.7 to 3.3 g/cm^3, which is less than the average density of the Earth, about 5.5 g/cm^3. Furthermore, measurements of Earth's precession and oblateness reveal that the moment of inertia of Earth is

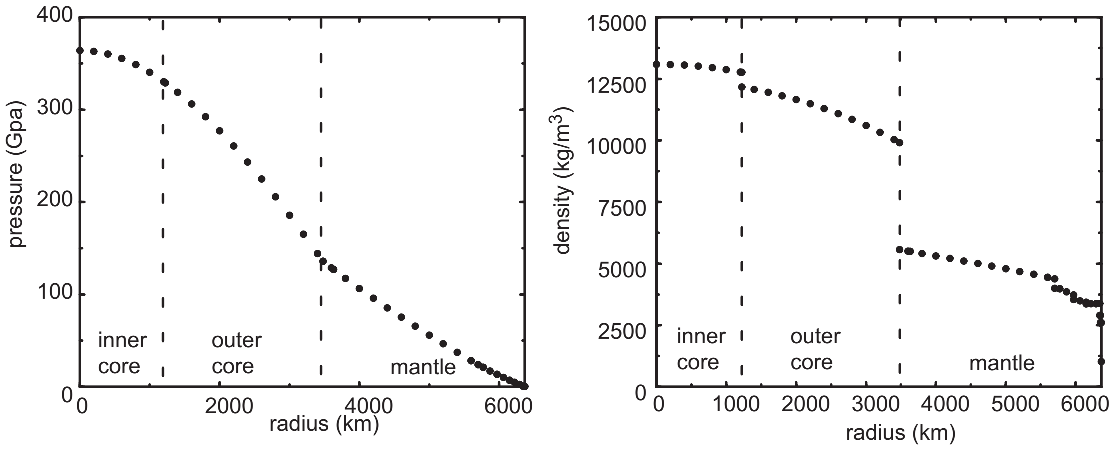

Figure 1.1: Radial profiles of pressure and density taken from the preliminary reference Earth model (PREM) [23].

$I = 0.33MR^2$, which is less than the value for a sphere of constant density $I = 0.4MR^2$. These facts imply that Earth's interior is inhomogeneous and of higher density towards its center. Perhaps this is unsurprising since the material at the center of the Earth is being compressed under the enormous weight of mass at larger radii. But compression alone appears not enough to account for the larger density at the deepest depths. This fact and a great wealth of more information about Earth's interior is obtained with measurements of seismic waves produced by earthquakes in the crust that propagate through the core.

Global arrays of three-component, broad-band seismographs have allowed great advances in knowledge of Earth's interior. Sound velocity vs. depth profiles and the period of free oscillation of the seismic waves are used to develop self consistent models, which specify the density, pressure, and elastic moduli as a function of depth. For example, fig. 1.1 shows radial density and pressure profiles. A recent and important example of such a model is called the preliminary reference Earth model (PREM) developed by Dziwolski and Anderson [23]. A good introduction to PREM is provided in a book by Poirier [50].

A fairly detailed picture of Earth's interior may be developed based on PREM or similar seismic models. I will first describe this picture and then describe the methods and assumptions from which the picture is arrived at from PREM data.

The volume of the Earth is divided into four main regions: a solid inner core of mostly iron, a iron-rich liquid outer core, a heterogeneous mantle composed of rock, and the crust at the surface. Seismological models like PREM indicate that the density increases with depth in a manner consistent with adiabatic compression until the bottom of the mantle. At that depth there is a sharp increase in density that must indicate a different material. Due to its abundance on Earth, the Sun, and meteorites, iron is the most likely material below the mantle [69]. The inner core boundary lies at a radius of 1220 km . Nearly three times this size, the core-mantle boundary is at a radius of 3480 km . The crust occupies only about top 25 km of the Earth's surface, which is 6371 km in mean radius. The boundaries between all of these regions are likely very rough and the above quoted radii are an approximate average over the boundary.

The inner core boundary is at a temperature of about 5000 K and a pressure 330 GPa . The outer core is predominantly iron, alloyed with one or more lighter elements. Some candidates for the lighter elements are silicon, sulfur, and oxygen. They comprise about 10 percent of the alloy by weight. The temperature at the core-mantle boundary is about 3800 K at a pressure of 130 GPa. There is a discontinuous jump in temperature ($\sim$800 K) crossing the boundary from the outer core to the mantle associated with a change in the chemical composition. The mantle is a solid capable of plastic deformation and is composed primarily of iron, magnesium, aluminum, silicon, and oxygen silicate compounds. Near the top of the mantle (700 km depth) the temperature is 1900 K and the pressure is around 20 GPa .

The method by which velocity and free oscillation periods of seismic waves are used to construct models relies on the approximations that Earth's interior is in spherically symmetric, hydrostatic equilibrium. The success enjoyed by these models suggests that the outer core is indeed in a nearly hydrostatic state. With these assumptions, The pressure P is related to the acceleration g and density ρ by

$$\nabla \bar{P}(r) = \bar{\rho}(r)\mathbf{\bar{g}}(r), \tag{1.1}$$

where here and throughout this section the overbar refers to quantities averaged over polar and azimuthal angle and bold characters represent vectors. The centrifugal acceleration causes a slight departure from spherical $\mathbf{g}$, but this feature is often ignored since, at most, the centrifugal acceleration is only 0.3% of gravitational acceleration. Seismological models also assume that the fluid outer core is isentropic and chemically homogeneous. This allows one to derive from eq. 1.1 relations for temperature, density, and chemical potential as a function of radius in the outer core. For example the pressure gradient of eq. 1.1 may be rewritten,

$$\begin{aligned} \frac{\partial P}{\partial r} &= \left(\frac{\partial P}{\partial T}\right)_S \frac{\partial T}{\partial r}, && (1.2) \\ \nabla P &= \frac{\rho c_p}{\alpha}\frac{\nabla T}{T}. && (1.3) \end{aligned}$$

where the basic thermodynamic relationship $(\partial P/\partial T)_S = \rho c_p/\alpha T$ is used to introduce the heat capacity c_p and volumetric thermal expansion coefficient α. Then combining eq. 1.1 and eq. 1.3 the so-called adiabatic temperature gradient in Earth's core is the solution to

$$\nabla \bar{T}(r) = \frac{\bar{\alpha}(r)\bar{T}(r)\bar{\mathbf{g}}(r)}{\bar{c}_p(r)}. \tag{1.4}$$

Similar manipulations using thermodynamic relationships yield first order differential equations for average density ρ and chemical potential μ,

$$\nabla \bar{\rho}(r) = \frac{\bar{\rho}(r)\bar{\mathbf{g}}(r)}{\bar{u}_s(r)^2}, \tag{1.5}$$

$$\nabla \bar{\mu}(r) = \bar{\alpha}^{\xi}(r)\bar{\mathbf{g}}(r). \tag{1.6}$$

where u_s is the speed of seismic compression waves, and α^{ξ} is the compositional expansion coefficient. With seismic measurements of u_s and a second equation relating $\mathbf{g}$ to ρ,

$$\nabla \cdot \bar{\mathbf{g}}(r) = -4\pi G\bar{\rho}(r), \tag{1.7}$$

one may in principle solve Eqns. 1.5 and 1.7 for $\mathbf{g}$ and ρ. G is the gravitational constant. Then using these solutions and assuming the expansion coefficients and specific heat are constant in the core, the other equations 1.1, 1.4, and 1.6 may also be solved to yield radial profiles similar to those shown in fig. 1.1.

Another source of information about the deep interior of the Earth is it's magnetic field. Depending upon the locale of the measurement, Earth's magnetic field is typically 5×10^{-5} T. In 1600, William Gilbert correctly suggested that the source of the magnetic field lies deep within Earth's interior [24]. Although not a perfectly spherical lodestone as Gilbert surmised, there are in fact three sources within the Earth which generate its magnetic field: permanent magnetism, magnetotelluric currents, and the geodynamo. Permanently magnetized minerals like iron and magnetite in the crust account for less than 0.1% of the observed field. Although the magnitude of local crustal magnetism may be comparable to 10^{-4} T, the spatial scales are disordered and small relative to the size of the planet. Therefore crustal permanent magnetism is highly unlikely to be responsible for a field with global structure. Furthermore, permanent magnetism is confined to the crust since just below the crust temperatures are above the Curie point.

Electric currents are induced in the core due to Earth's motion through the magnetic fields of other planets and the sun. These so-called magnetotelluric currents give rise to magnetic fields which make a small contribution to Earth's full magnetic field. Magnetotelluric magnetic fields are identified by their time dependence which is simply related to the orbits of the Earth, the sun, and other planets.

The third and dominant source of Earth's magnetic field is the geodynamo. Several centuries after Gilbert, Joseph Larmor, in 1919, was the first to suggest that the magnetic field of cosmic bodies may originate from the motion of electrically conducting fluid within the body, i.e. a dynamo [41]. The dynamo process is believed to be responsible for the magnetic field of most planetary, stellar, and galactic magnetic fields. The motion of electrical conductors, including fluids, in the presence of a magnetic field causes electric currents in the fluid. This is called Faraday induction. The induced currents are accompanied by magnetic fields, which may reinforce the original magnetic field. If so, a positive feedback loop can exist where a magnetic field induces currents, which in turn, produce more magnetic field, which induce more currents, and so forth.

In this case the zero magnetic field solution to the governing equations is unstable to a growing magnetic field solution. The fact that the Earth has a large scale dynamic magnetic field indicates that the liquid iron outer core is in motion. The kinetic energy of the flowing iron is converted into magnetic energy via the dynamo process and then dissipated as heat by Ohmic dissipation of the electric currents.

Observations of Earth's magnetic field provide more information than the simple fact that the fluid outer core is in motion. Measurements reveal broadband variations in time and space, which suggest that the outer core motion is turbulent. Decomposed into a sum of spherical harmonics, the current surface field is primarily dipole (about 70 % of the power in the observable field), but shows complicated structure up to spherical harmonic degree $l = 23$. An approximate expression for the power in the different degrees is [40]

$$log_{10} W_l \approx \begin{cases} -3.270 - 0.569l, & for \quad 2 \leq l \leq 12 \\ -10.83 - 0.0114l, & for \quad 16 \leq l \leq 23 \end{cases} \tag{1.8}$$

Permanent magnetism in the crust is thought to be responsible for the higher degree structure, $l \geq 16$. The $2 \leq l \leq 12$ structure is thought to originate from the outer core, having great enough spatial scale to avoid the filtering of the crust and mantle. This portion of field is referred to as the *main field.* In addition to the spatial structure, the main field varies on time scales between 1 and 10^5 years. These temporal dynamics are called *secular variation.* A salient feature of the secular variation is an overall westward drift of the spatial structure. The drift is latitude dependent and irregular in time. The westward drift may be caused by zonal flow (i.e. azimuthal flow) of the liquid in the outer core. An estimate of that velocity for mid-latitude is about 10^{-4} m/s. An excellent review of our current understanding of the main field and numerical simulations was written by Roberts and Glatzmaier [54].

What is the energy source for the fluid motion that is responsible for the rich dynamics observed in the main field? The answer to this question is the topic of ongoing research and to a large extent the topic of the work presented in this dissertation. One possible mechanism for driving fluid flow in the outer core is forces due to precession of Earth's rotation (e.g. [42]). A more likely candidate and the focus of the discussion here is buoyancy driven convection.

There are two types of convection in Earth's outer core: thermal and compositional. Let us first consider compositional convection, where the presence of less dense elements in the fluid give rise to buoyancy forces. The fluid in the outer core primarily consists of iron mixed with one or more lighter elements in an approximately 10:1 ratio by weight [1]. As heat is carried out of the core by the fluid motion and conduction, the temperature at the inner core is ever so slowly dropping. Since the pressure does not drop with the temperature, the boundary where iron becomes solid is pushed to larger and larger radii. That is to say, the inner core is growing. As the iron solidifies on the inner core boundary, fractionation causes an accumulation of the lighter elements in the liquid near the inner core. Buoyancy forces float this light-element-rich mix towards the surface of the outer core. In this way the growth of the inner core is self promoting. The more it grows, the more the light elements are released to stir the outer core. The more the outer core is stirred, the more heat is carried out of the core thereby lowering the temperature and promoting more inner core growth. It should be noted, that the low thermal conductivity of the mantle likely acts as a bottle neck for heat leaving the outer core, limiting the rate of cooling.

Thermal convection is similar to compositional convection, but slightly more complicated. There are several possible heat sources which may drive thermal convection in Earth's core. One is the heat of fusion which is released at the inner core boundary as it grows. Another possibility is simply the original heat from the formation of Earth. In this case, the Earth is still hot, but cooling off via convection and conduction through the core and mantle and radiation from the surface. A third possibility, which is more controversial, is the existence of radioactivity in the core. It is known that the vast majority of heat flux through the crust is due to radioactive decay in the mantle. It is debated to what extent radioactive elements (particularly potassium-40) add to heat production in the core [53]. Another possible heat source is viscous dissipation of motion, perhaps due to tidal forces caused by the moon's gravity.

In order for thermal convection to occur in some region of the Earth's core, it is necessary that the local temperature gradient have a steeper slope than that of the local adiabatic tem-

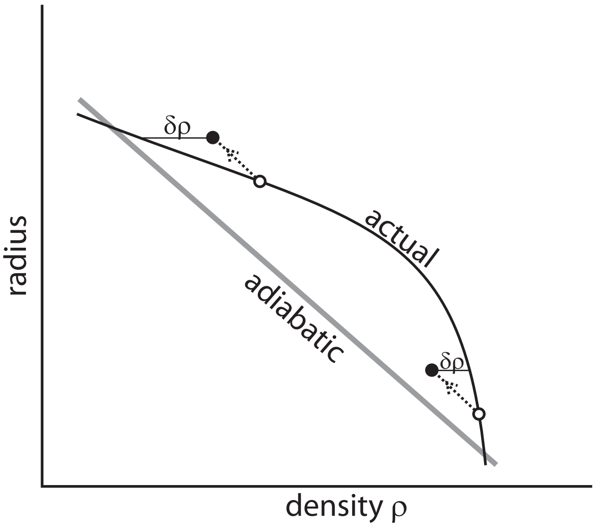

Figure 1.2: Illustration of fictitious density and adiabatic gradients. The gradient is unstable to convection at small radii and stable at large radius.

perature gradient. The adiabatic temperature gradient is the temperature profile solely due to compression, the solution of eq. 1.4. Even without considering convection the adiabatic gradient conducts a great deal of heat out of the core. The heat sources in the core must exceed the heat conducted along the adiabatic gradient for convection to occur. To better understand this idea, consider a fluid parcel displaced a distance δr from its starting point to a larger radius. Adiabatic expansion will decrease its density by $\delta\rho$ (and also its temperature by δT). If the actual density (temperature) gradient is shallower than the adiabatic gradient, then the fluid parcel will be heavier than the surrounding fluid and sink back to where it started. If the actual density (temperature) gradient in the fluid is steeper than the adiabatic gradient, then the fluid parcel will be less dense than the surrounding fluid and experience a buoyant force to rise to even larger radius. The first case describes a stable gradient, while the second is unstable to convection. This concept is illustrated in fig. 1.2.

There are several questions hovering about the idea of convection as an energy source for the geodynamo. How much power must the convective motions supply to sustain the geodynamo? One might form a minimum guess based on the Ohmic dissipation that would occur in Earth's core due to the magnetic field which is observable at the surface. Roberts et al. estimate from 6 MW [53]. Speculating about how much more dissipation might occur due to smaller scale magnetic field structure, which we cannot measure at the surface, Roberts et al. estimate up to 2 TW. Total heat flux leaving the outer core is estimated to be in the range 1-10 TW (e.g. [9], [39]). Is this enough power to drive the geodynamo? How much of this is due to convection and how much due to conduction down the adiabat? How much power is in the small scale magnetic field within the core? This genre of questions motivates the experiments presented in this dissertation. We hope to shed some light on the mechanisms of convection in rotating, spherical systems. We also touch upon the interaction of magnetic fields with the convective state.

To summarize, the basic state of Earth's outer core is close to hydrostatic equilibrium. The fluid motion which drives the geodynamo is a relatively small departure from this adiabatic base state. Nonetheless, the structure and dynamics of the main geomagnetic field suggest the core is highly turbulent with strong zonal flow as well. Turbulent convection with strong zonal flow and large conductive heat transfer are characteristics observed throughout the experiments presented in this dissertation.

1.1.1 *Equations of motion*

Before continuing further I will present the equations of motion governing the fluid motion in the core. These are taken from an analysis by Braginsky and Roberts [8].

$$\partial_t \rho = -\nabla \cdot (\rho \mathbf{v}), \tag{1.9}$$

$$\rho \partial_t \mathbf{v} + \rho(\mathbf{v} \cdot \nabla)\mathbf{v} = -\nabla p + \rho \mathbf{g} - 2\rho \mathbf{\Omega} \times \mathbf{v} + \rho \mathbf{F}^B + \rho \mathbf{F}^\nu, \tag{1.10}$$

$$\rho \partial_t S + \rho(\mathbf{v} \cdot \nabla) S = -\nabla \cdot \mathbf{I}^S + \sigma^S, \tag{1.11}$$

$$\rho \partial_t \xi + \rho(\mathbf{v} \cdot \nabla)\xi = -\nabla \cdot \mathbf{I}^\xi, \tag{1.12}$$

$$\nabla \cdot \mathbf{B} = 0, \tag{1.13}$$

$$\partial_t \mathbf{B} + (\mathbf{v} \cdot \nabla)\mathbf{B} = \nabla \times (\mathbf{v} \times \mathbf{B}) - \nabla \times (\eta \nabla \times \mathbf{B}). \tag{1.14}$$

The first equation is the continuity equation, expressing conservation of mass with ρ and $\mathbf{v}$ representing density and fluid velocity. The second is the Navier-Stokes equation with buoyancy force $\rho\mathbf{g}$, Lorentz force $\rho\mathbf{F}^B = \mathbf{J} \times \mathbf{B}$, and Coriolis force $-2\rho\mathbf{\Omega} \times \mathbf{v}$ included. The pressure, gravitational acceleration, and rotation vector of the Earth are p, $\mathbf{g}$, and $\mathbf{\Omega}$ respectively. The viscous force is

$$\rho\mathbf{F}^\nu = \nabla \cdot \pi^\nu, \tag{1.15}$$

where

$$\pi^\nu_{ij} = 2\rho\nu(e_{ij} - \frac{1}{3}e_{kk}\delta_{ij}) \tag{1.16}$$

and $e_{ij} = \frac{1}{2}(\nabla_i v_j + \nabla_j v_i)$ is the strain rate tensor and ν is the kinematic viscosity of the fluid. The Navier-Stokes equation is a statement of conservation of momentum in the fluid. The third equation governs entropy S, with $\mathbf{I}^S$ representing entropy flux and σ^S representing entropy production. The mass fraction is ξ and $\mathbf{I}^\xi$ is the mass flux. The magnetic field $\mathbf{B}$ is solenoidal, i.e. there are no magnetic monopoles. This fact is embodied in eq. 1.13. The dynamics of the the magnetic field is governed by the induction equation (eq. 1.14), wherein η is the magnetic diffusivity.

1.2 **Experiment compared to the Earth**

The experimental apparatus consists of a 60 *cm* diameter outer sphere and a concentric 20 *cm* diameter inner sphere. In the space between the spheres is 110 kg of sodium. The inner sphere is cooled by pumping kerosene at a constant temperature through its interior. The outer sphere is heated with an array of heat lamps. The spheres co-rotate at rotation rates up to 25 RPS. The centrifugal acceleration due to the rotation and the temperature gradient between the cool inner and hot outer sphere cause buoyancy forces to drive convective motion in the liquid sodium.

In principle, the equations of motion are the same for the experiment as those for Earth's outer core (eqs. 1.9 - 1.14), but some simplifications may be made. The fluid may be approximated as incompressible, $\nabla \cdot \mathbf{v} = 0$, except for in the buoyancy force term of the Navier-Stokes equation (Boussinesq approximation). (At the highest rotation rates of the apparatus, there actually is compression in the fluid which gives rise to density changes of order 0.1%.) For the buoyancy force, compressibility manifests in the simple equation of state, $\rho = \rho_0(1 - \alpha(T - T_0))$. The resulting buoyancy force is

$$\mathbf{F}^{bouyancy} = (\rho - \rho_0)\Omega^2 r\hat{\mathbf{r}} = -\rho_0\alpha\tilde{T}\Omega^2 r\hat{\mathbf{r}}, \tag{1.17}$$

where $\tilde{T} = T - T_0$ is the deviation of the temperature from the conductive heat profile T_0. The centrifugal acceleration is $\Omega^2 r\hat{\mathbf{r}}$, where $\hat{\mathbf{r}}$ is the cylindrical radial unit vector. The entropy equation may be recast in terms of temperature, perhaps an easier form to interpret. The mass fraction equation is omitted since there is no compositional convection in our experiment; the medium is pure sodium and motion is due solely to thermal convection. It should be noted that centrifugal compositional convection experiments in the same geometry as the presented experiment show very similar character of flow [14]. The dimensional equations of motion for the experiment are then,

$$\begin{aligned}
\nabla \cdot \mathbf{v} &\approx 0, && (1.18)\\
\partial_t \mathbf{v} + (\mathbf{v}\cdot\nabla)\mathbf{v} &= -\frac{\nabla p}{\rho_0} - \alpha\Delta T\Omega^2 r\hat{\mathbf{r}} - 2\,\mathbf{\Omega}\times\mathbf{v} + (\nabla\times\mathbf{B})\times\mathbf{B} + \nu\nabla^2\mathbf{v}, && (1.19)\\
\partial_t T + (\mathbf{v}\cdot\nabla)T &= \kappa\nabla^2 T, && (1.20)\\
\nabla\cdot\mathbf{B} &= 0, && (1.21)\\
\partial_t\mathbf{B} &= \nabla\times(\mathbf{v}\times\mathbf{B}) + \eta\nabla^2\mathbf{B}. && (1.22)
\end{aligned}$$

The diffusive term in the induction equation has been simplified using vector identities and the fact that the magnetic field is solenoidal, $\nabla\cdot\mathbf{B} = 0$. These equations may be made dimensionless with the substitutions,

$$\begin{aligned}
t &\rightarrow t'\frac{D^2}{\nu}, && (1.23)\\
v &\rightarrow v'\frac{\nu}{D}, && (1.24)\\
r &\rightarrow r'D && (1.25)\\
\tilde{T} &\rightarrow \tilde{T}'\Delta T\frac{\nu}{\kappa}, && (1.26)\\
B &\rightarrow B'\frac{\nu B_0}{D\sqrt{\Omega\eta\mu_0}}, && (1.27)
\end{aligned}$$

where D is the size of the gap between the inner and outer sphere (20 cm), ΔT is the temperature drop from the inner sphere to the outer sphere. B_0 is the strength of the applied magnetic field, and μ_0 is the magnetic permeability of sodium. Dropping the primes the resulting equations are

$$\nabla \cdot \mathbf{v} \approx 0, \tag{1.28}$$

$$\partial_t \mathbf{v} + (\mathbf{v} \cdot \nabla)\mathbf{v} = -\nabla p - Ra\tilde{T}r\hat{\mathbf{r}} - E^{-1}\hat{\mathbf{k}} \times \mathbf{v} + \Lambda \nabla \times \mathbf{B} \times \mathbf{B} + \nabla^2 \mathbf{v}, \tag{1.29}$$

$$\partial_t T + (\mathbf{v} \cdot \nabla)T = Pr^{-1}\nabla^2 T, \tag{1.30}$$

$$\nabla \cdot \mathbf{B} = 0, \tag{1.31}$$

$$\partial_t \mathbf{B} = \nabla \times (\mathbf{v} \times \mathbf{B}) + Pm^{-1}\nabla^2 \mathbf{B}, \tag{1.32}$$

where $\hat{\mathbf{k}}$ is a unit vector aligned with the rotation axis. There are now five dimensionless numbers which characterize the problem: Ekman number E, Rayleigh number Ra, Elsasser number Λ, Prandtl number Pr, and magnetic Prandtl number Pm.

$$E = \frac{\nu}{2\Omega D^2}, \tag{1.33}$$

$$Ra = \frac{\alpha \Delta T \Omega^2 D^4}{\nu \kappa}, \tag{1.34}$$

$$\Lambda = \frac{B_0^2}{\rho \eta \Omega \mu_0} \tag{1.35}$$

$$Pr = \frac{\nu}{\kappa}, \tag{1.36}$$

$$Pm = \frac{\nu}{\eta}. \tag{1.37}$$

The Ekman, Rayleigh, and Elsasser numbers are nondimensionalizations of the three control parameters used in the experiment, which are respectively, the rotation rate, the temperature drop across the gap between the spheres, and the applied magnetic field. The Ekman number is a nondimensionalization of rotation rate with the viscous diffusion time. It is an important parameter in the dynamics of viscous boundary layers in rotating flows. The Rayleigh number characterizes the competition between convection and diffusion. One way to interpret Ra is as a ratio of the convective fluid velocity squared to the diffusive velocities due to viscosity and temperature diffusion. That is, the ballistic estimate for a fluid element at a temperature ΔT colder than its neighbors is $v_b = D\Omega\sqrt{\alpha \Delta T}$, the viscous diffusive velocity is $v_\nu = \nu / D$ and the thermal diffusive velocity

	experiment	**Earth's outer core**
Ekman	4.6×10^{-7} to 5.5×10^{-8}	10^{-15} [22]
Rayleigh	4.2×10^{6} to 2.8×10^{9}	10^{20} to 10^{30} (e.g. [32], [48])
Elsasser	0 to 1.9×10^{-4}	1
Prandtl	0.01	$10^{-1}$to 10^{-2} (e.g. [53], [48])
magnetic Prandtl	1.2×10^{-5}	10^{-6} [53]

Table 1.1: Comparison of values of dimensionless numbers in the experiments and Earth estimates.

is $v_\kappa = \kappa/D$. The Raleigh number is then $Ra = v_b^2/v_\nu/v_\kappa$. The Elsasser number is the ratio of Lorentz forces to Coriolis forces. The two Prandtl numbers are properties of the fluid which remain very close to constant throughout the experiments. Table 1.1 shows a comparison of the nondimensional numbers of the experiment and Earth's outer core.

Two obvious differences between the Earth's outer core and our experiment are the direction of gravitational acceleration and the temperature gradient. Opposite the Earth, the experiment is cooled at its center and heated on the outside. Earth's gravitational acceleration is directed radially inward with spherical symmetry while the centrifugal acceleration in the experiment is radially outward with cylindrical symmetry. However, since both the temperature gradient and direction of acceleration are reversed, the buoyancy forces are mathematically nearly equivalent; two negative signs in the buoyancy term in the Navier-Stokes equation cancel. What about the difference between spherical and cylindrical "gravity"? This difference is mediated by the effects of rotation. In particular, Coriolis forces tend to confine the motion of the fluid to planes perpendicular to the rotation axis. In other words, the components of spherical gravity which are not cylindrically radial are inhibited by rotation to do significant work on the fluid. This fact is made clear by the Taylor-Proudman theorem. If the two dominant terms in the Navier-Stokes equation are pressure and the Coriolis force, a *geostrophic* balance, we have

$$2\rho\mathbf{\Omega} \times \mathbf{v} = -\nabla p. \tag{1.38}$$

Taking the curl of this equation and assuming an incompressible fluid, $\nabla \cdot \mathbf{v} = 0$ we're left with a mathematical restatement of the Coriolis force effects mentioned above,

$$(\mathbf{\Omega} \cdot \nabla)\mathbf{v} = 0. \tag{1.39}$$

The Taylor-Proudman theorem is embodied by eq. 1.39. The theorem states that there may be no gradients in velocity along the direction of the rotation axis; the motion is two dimensional in planes perpendicular to $\mathbf{\Omega}$. The Taylor-Proudman theorem as manifested in rotating convection was demonstrated in a direct comparison of spherical and cylindrical gravity in numerical simulations by Glatzmaier and Olson [27]. They found very similar character of convection in both cases. Further support for the idea that geostrophic convection takes a two dimensional form is provided in asymptotic analyses by Roberts (1968) [52] and Busse (1970) [10].

In addition to the difference in shape between cylindrical and spherical gravity, the experiment is subjected to Earth's gravity, vertical and anti-parallel with the rotation vector of the experimental vessel. In the absence of rotation, this acceleration due to Earth's gravity would drive so-called natural convection between the spherical shells. The expected power-law dependence between natural convective heat transfer and the Rayleigh number is $h \sim Ra^{\alpha}$ with α between 0.25 and 0.3. For example, an experimental study with liquid sodium convection around a heated cylinder far from boundaries is [34]

$$Nu = 0.53(RaPr)^{1/4}, \tag{1.40}$$

Where Nu is the Nusselt number, defined as the ratio of total heat transfer to that due solely to conduction. Then $Nu - 1$ represents the dimensionless convective heat transfer. For air in the annular gap between concentric spheres (like our geometry) the exponent is slightly higher $Nu \sim Ra^{0.276}$ [7]. Neglecting the differences between vertical plates and concentric spheres, the onset of natural convection for our apparatus occurs at a temperature drop of order 10^{-4} °C. In other words, unless it is suppressed by Taylor-Proudman type constraints, natural convection is likely to be present for even the lowest temperature drops and rotation rates attained in the experiment. One might expect a cross-over from natural convection to centrifugal convection at some ΔT for a given rotation rate. In our results presented later, this cross-over is assumed to be at or before the predicted onset of centrifugal convection.

Another significant difference between Earth's outer core and the experiment is that the extremely high pressure in the outer core gives rise to effects related to compressibility as discussed in the introduction. Although not absent, these effects are much less severe in the experiment. It is straightforward to compute the effects of compression in the experiment since the centrifugal acceleration is known, $a_c = \Omega^2 r$. Using eq. 1.4 with cylindrical radius r instead of spherical r and substituting a_c for g,

$$\nabla \bar{T} = \frac{\alpha \bar{T} \Omega^2 r}{c_p}. \tag{1.41}$$

Assuming the boundaries are also cylindrically symmetric, one may integrate this to find the adiabatic temperature profile,

$$\bar{T}(r) = T_i exp \left(\frac{\alpha \Omega^2 (r^2 - r_i^2)}{2c_p} \right), \tag{1.42}$$

where T_i and r_i are the temperature and radius of the inner sphere. With the inner sphere at a typical temperature of 107 °C, the resulting temperature profiles for a variety of rotation rates are shown in fig. 1.3. (It is perhaps interesting to note that at the highest rotation rate attained with the experiment, 25 Hz, the centrifugal acceleration at the largest radius of the experiment is nearly $1000g$.) Typical temperature drops reached in the experiment are between 2 and 20° C. The adiabatic temperature difference is 0.63° C at 25 Hz and is therefore significant for the lowest temperature drops.

Perhaps the most significant difference between the experiment and Earth's core is the lack of a dynamo in the experiment. Some of the presented experiments were conducted with magnetic fields applied with external Helmholtz coils in an attempt to compensate for the lack of a dynamo. The magnetic field in Earth's core certainly plays an important role in the dynamics of the fluid motion. It is nonlinear interactions between the velocity field and magnetic field which sets the magnitude of the main field around 10^{-4} T. One can imagine a thought experiment in which the magnetic field is reset to zero magnitude. If the zero field solution is unstable in the fluid motion of the outer core, the magnetic field would begin to grow. It would continue to grow until Lorentz forces are large enough to modify the fluid flow in such a way as to stem further growth, but

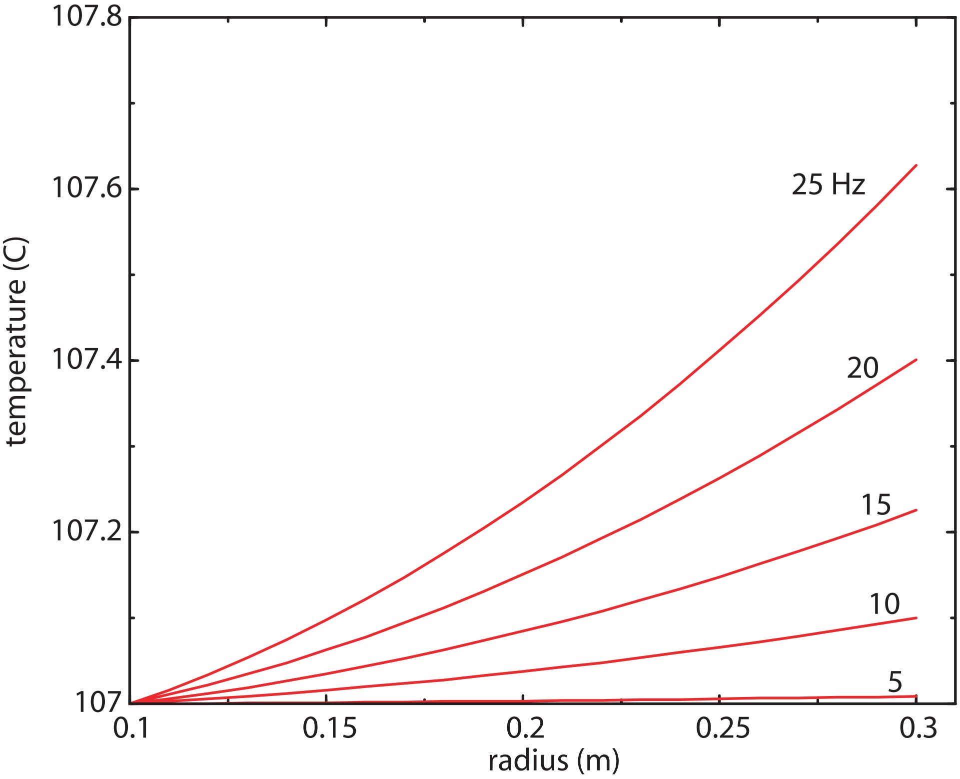

Figure 1.3: Adiabatic temperature profiles for the different rotation rates investigated, assuming a typical inner sphere temperature of 107° C. The inner sphere radius is 0.1 m and the outer sphere radius is 0.3 m.

maintain it's current value. This is presumably the current situation in the Earth's core; there is a balance between Lorentz forces and the driving forces of fluid motion. Some suggest that there is a three way balance between Lorentz, Coriolis, and buoyancy forces (e.g. [57]). For most of the measurements taken in the experiments, magnetic field is absent, in which case the force balance is between Coriolis and buoyancy or inertia and buoyancy. For the experiments with an imposed magnetic field the Elsasser number is, at most, about 10^{-4}. At this level, the magnetic field has some influence, although not very dramatic, on the observed dynamics.

1.3 Review of related work

The first experimental investigation of centrifugally driven convection as a model of planetary cores was conceived and implemented by Busse and Carrigan in 1976 [17] [18]. Since then, there have been a number of similar experiments, which I will divide into two categories: close to onset and fully developed convection. The experiments near onset (Busse and colleagues [17], [18], [19], [21], [5], Chamberlain and Carrigan [20], and Jaletzky [35]) have largely confirmed the early analytical work of Busse [10] and Roberts [52]. These studies were mostly in water, with a few in mercury.

The character of fluid flow near onset is two dimensional and periodic in space and time. The spatial periodicity manifests in an array of column-like vortices which form a belt around and tangent to the inner sphere. The region where the vortices form is often called the *tangent cylinder.* The diameter of the vortices is smaller than the shell gap and decreases as rotation rate increases. The flow is approximately two-dimensional outside of thin boundary layers on the outer sphere. That is, the columnnar vortices extend from the outer boundary of the bottom hemisphere to the outer boundary of the top hemisphere with any slice through the flow perpendicular to the rotation axis revealing a very similar flow pattern. These columns also tilt in a prograde sense with respect to the sphere rotation and precess around the inner sphere in time. Busse (1970) predicted the columnar structure, while the frequency, length scales, and critical value of Rayleigh number for convection onset come from asymptotic analysis by Roberts (1968),

$$\omega_c \quad \sim \quad E^{-2/3}, \tag{1.43}$$

$$\delta \sim DE^{1/3}, \tag{1.44}$$

$$Ra_c \sim E^{-4/3}. \tag{1.45}$$

It should be noted that these scaling laws are obtained for very small Ekman numbers and large Prandtl number (≥ 1). Zhang 2000 [70] presented the expected scalings for very low Prandtl number (10^{-4}) and Ekman number,

$$\omega_c \sim 1, \tag{1.46}$$

$$\delta \sim D, \tag{1.47}$$

$$Ra_c \sim E^{-1/2}. \tag{1.48}$$

The Prandtl number of sodium is $Pr_{Na} = 0.01$. As will become apparent in the chapters on experimental results, the observed behavior in our experiments are not entirely consistent with either extreme.

Experiments conducted far beyond the onset of convection, have been conducted in a variety of fluid media: in order of decreasing Prandtl number, silicon oil (Pr=13), water (Pr=7), gallium (Pr=0.03), and sodium (Pr=0.01). Cordero did experiments to investigate convection in transition from the regime of regular patterns described above to irregular turbulent convection [21]. Cardin and Olson [14] did compositional convection experiments in water and a more dense mixture of water and sucrose. They found qualitatively similar results to those observed in thermal convection. They also did thermal convection experiments which they modelled with a quasi-geostrophic numerical code [15]. They observed turbulent convection characterized by ribbon-like plumes near the equatorial plane and mean zonal flows driven by Reynolds stresses. The typical length scale of the turbulent plumes was found to remain close to that predicted near onset of convection. They observed retrograde zonal flows at the inner sphere and prograde at the outer.

Sumita and Olson have conducted a series of experiments in a hemispherical geometry at an Ekman number $E = 4.7 \times 10^{-6}$. They studied the effects of inhomogeneous heating on the vessel boundary [59], [60]. They found that a large scale spiral flow with a sharp front develops. This front was suggested as a cause for certain features of the secular variation in Earth's main field. They suggested flow in the outer core may be composed of fast jets and slower zonal flows caused by inhomogeneous heat transfer at the core-mantle boundary. In water experiments with homogeneous boundary heating, they observed convection from onset up to 45 times the critical Ra [61]. Increasing Ra, convection first developed at the inner sphere in the form of prograde spiralling, 2-D turbulent plumes. For higher Ra, plumes also develop at the outer sphere, mixing with the inner sphere plumes to create a fine scale geostrophic turbulence. The results obtained with water were suplemented by using silicon oil, which allows for much higher values of Ra. They report values of $Ra \leq 600 Ra_c$. A scaling for heat transfer was obtained from the combined results of water experiments and those with silicon oil, $Nu \sim Ra^{0.41\pm0.02}$. They also did two-layer convection experiments with silicon oil and water and measured heat flux for different thickness ratios of the two fluids.

In the experiments by Cardin, Olson, and Sumita, the convecting fluid and the vessel were transparent. This allowed for qualitative flow visualization with dyes and reflective flakes. In our experiment, and in much of the work I will describe in the next paragraph, the working fluids are liquid metals, which are unfortunately opaque. Therefore other means are necessary for obtaining flow dynamics.

Aubert, Gillet and colleagues in Grenoble have conducted convection experiments in a vessel with a spherical outer wall and a cylindrical inner boundary. They used gallium and water [2]. They reach Ekman numbers down to 7×10^{-7} and Ra up to 80 times critical in water and 4 times critical for gallium. They used ultrasonic Doppler velocimetry to obtain scaling laws for velocities and vortex size as a function of Ekman, Rayleigh, Prandtl, and Nusselt numbers. They found that their measurements agreed well with scaling laws derived from a quasi-geostrophic model similar to that used by Cardin and Olson in the numerical work mentioned above. They found

$$u_r = \frac{\nu}{D^2}\left(\frac{Ra_Q}{Pr^2}\right)^{2/5} E^{1/5}, \tag{1.49}$$

$$\delta_r = D\left(\frac{Ra_Q}{Pr^2}\right)^{1/5} E^{3/5}, \tag{1.50}$$

$$\frac{u_{zonal}}{u_r} = Re_l^{2/3} E^{1/6}, \tag{1.51}$$

(1.52)

where u_r and u_{zonal} are the radial and zonal velocities, δ_r is the radial size of vortex structures, $Re_l \equiv u_r\delta_r/\nu$ is the local Reynolds number, and $Ra_Q \equiv RaNu$ is the heat flux based Rayleigh number. In addition to these scaling laws, they observed that zonal flows were much larger in magnitude in gallium than in water. Supplementing their experiments, they found the scaling laws in good agreement with results from a quasi-geostrophic numerical model [3]. Gillet in collaboration with Chris Jones has more recently used this model to develop a scaling law for u_r in terms of the Nusselt number of the form [25],

$$Pe_l = \frac{u_r L}{\kappa} = \left(\frac{Ra}{Ra_c}Nu - 1\right)^{1/2}. \tag{1.53}$$

Quantitative comparisons of results of the gallium experiments and certain aspects of the Sumita and Olson experiments to the results of our experiment will be presented in chapter 4.

A great deal of numerical work has addressed the problem of convective flows in rotating spheres and possible resulting dynamo action. Good reviews of these works are given by Busse [11], Zhang and Schubert [70], and Roberts and Glatzmaier [54]. A recent review of experimental work related to dynamos, but not limited to convection experiments is presented by Nataf [46].

1.4 Outline of this dissertation

Chapter 2 is a description of the experimental apparatus. It is written in extreme detail for the sake of reproducibility and future grad students who inherit the apparatus. The third chapter, also packed with technical detail, delineates the data acquisition systems and methods for processing the data. The experimental results and accompanying interpretations are given in chapter 4. These results are divided into five sections: temperature standard deviation, temperature probability density functions, zonal velocity, heat transfer, and power spectra. Finally in chapter 5, the experimental results are summarized and extrapolated to predict certain quantities and behavior in the outer core of the Earth.

Chapter 2

EXPERIMENTAL APPARATUS AND METHODS

This chapter is a detailed description of the apparatus and methods used in the experiments. The first section describes the vessel in which the convecting sodium resides. Each of the following four sections is devoted to one of the peripheral systems necessary for running the experiments: cooling, heating, rotation, and magnetic fields. The last section describes the process by which the sphere is filled with sodium. A schematic of the vessel and many of the stationary peripheral parts is shown in fig. 2.1. The physical properties of sodium and how they depend upon temperature are delineated in table 2.1. The data in table 2.1 comes from the *Handbook of thermodynamic and transport properties of alkali metals* edited by Roland W. Ohse [47].

2.1 **Rotating assembly**

Throughout the description of the device I will use names for its parts in analogy to the Earth. For example, equator refers to the intersection of the surface of the spheres with the plane perpendicular to the rotation axis midway between the top and bottom of the spheres (the equatorial plane). The poles are the two points where the rotation axis intersects the surface of the sphere.

The outer sphere is composed of two thick hemispherical shells which both screw into a ring at the equator. (The hemispheres, the ring and the inner sphere were machined by Bechdon corporation). A teflon-encapsulated silicon o-ring is compressed between the mating surfaces of the two hemispheres. The walls are 2.54 cm thick aircraft alloy titanium (Ti-6Al-4V). The equatorial ring which binds the two hemispheres together is the same titanium alloy, but is plated with nickel to prevent gauling in the threads.

The bottom hemisphere has a 8.89 cm diameter, hollow titanium shaft extending from the south pole towards the center. The inner sphere screws into this bottom shaft so that it is spherically concentric with the outer sphere. A metal gasket coated with Loktite 515 forms a seal impervious to sodium and kerosene where the inner sphere meets the bottom shaft. The top hemisphere, likewise, has a shaft extending from the north pole towards the inner sphere. A pair

T	$\nu \times 10^3$	ρ	c_p	k	$\alpha \times 10^4$	κ	Pr
(K)	(cm^2/s)	(g/cm^3)	(J/gK)	(W/cmK)	$(1/K)$	(cm^2/s)	
371	7.3	0.923	1.43	0.911	2.36	0.69	0.011
380	7.12	-	-	-	-	-	-
390	6.81	-	-	-	-	-	-
400	6.51	0.917	1.41	0.878	2.38	0.68	0.0096
410	6.25	-	-	-	-	-	-
420	6.01	-	-	-	-	-	-
430	5.78	-	-	-	-	-	-
440	5.58	-	-	-	-	-	-
450	5.39	0.906	1.38	0.834	2.42	0.67	0.0081
460	5.21	-	-	-	-	-	-
470	5.05	-	-	-	-	-	-
480	4.90	-	-	-	-	-	-
490	4.76	-	-	-	-	-	-
500	4.62	0.895	1.35	0.798	2.47	0.66	0.007
510	4.50	-	-	-	-	-	-
520	4.38	-	-	-	-	-	-
530	4.28	-	-	-	-	-	-
540	4.17	-	-	-	-	-	-
550	4.08	0.884	1.33	0.767	2.51	0.65	0.006

Table 2.1: Properties of sodium and their temperature dependence [47].

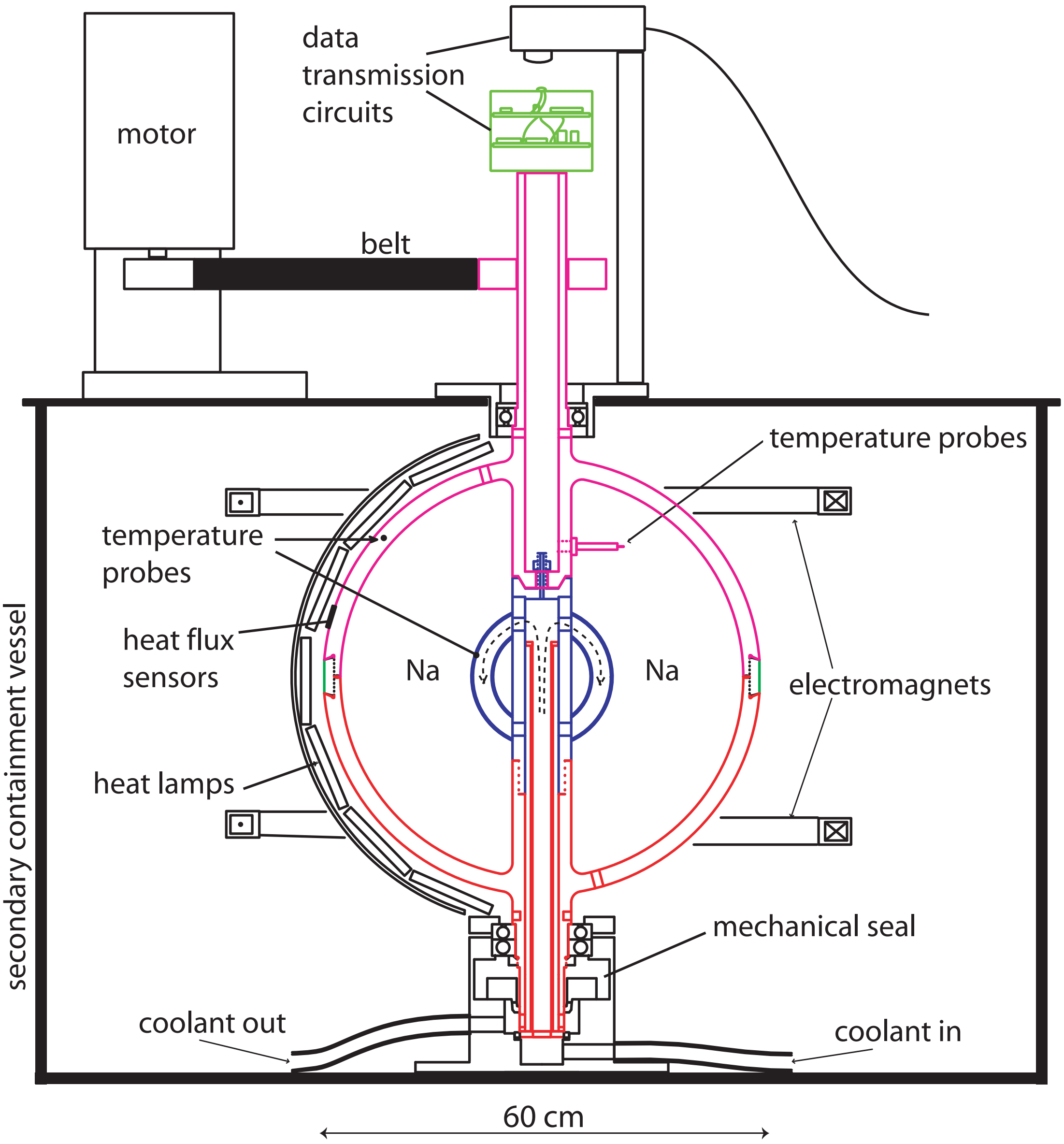

Figure 2.1: The experimental apparatus consists of co-rotating, concentric spherical shells, between which sodium convects.

of teflon-encapsulated silicon o-rings seal the seam between the top shaft and the inner sphere.

Heat is extracted from the system by pumping kerosene through the inner sphere at a constant temperature and flow rate. The inner sphere is made of stainless steel. The wall between the sodium and kerosene is 0.25 cm thick. Inside the inner sphere is another spherical shell with a 15 cm diameter. As indicated by the dashed lines in fig. 2.1, the kerosene flows in the 2.54 cm gap between this innermost sphere and the inner sphere wall. A stainless steel tube with 3.81 cm diameter inserts into the hollow bottom shaft (5.08 cm diameter bore). The kerosene enters the inner sphere through this tube and exits through the anular gap between the tube and the bottom shaft wall.

The bottom shaft spans the distance from the inner sphere, through the outer sphere wall at the south pole, and further down to a pair of bearings and a mechanical seal. The bearings are two angular contact ball bearings (SKF 7216 BE) placed back-to-back, seated in a stainless steel base. Also housed in the stainless steel base, the mechanical seal (John Crane type 613) provides a fluid coupling between the stationary coolant hoses and the rotating bottom shaft.

The top shaft also extends past the upper surface at the north pole of the outer sphere. The leads from six thermocouples located on the inner sphere pass through the hollow of the top shaft. These wires connect to a data processing circuit mounted to the top of the shaft. Leads from instrumentation on the outer sphere also pass through a hole in the wall of the top shaft just above the outer sphere surface and continue up to the data processing circuit. On the exterior surface of the top shaft are bearings, slip rings for powering the data circuit, and a pulley. The pulley is a 6 inch diameter, 48 tooth, L-series timing belt pulley for driving the rotation of the sphere. The slip rings are simply constructed from adhesive backed copper strips over several electrically insulating layers of Kapton tape.

The bearing on the top shaft (SKF 6016) and the stainless steel base are attached to a secondary vessel; it is a stainless steel cylinder with 0.95 cm thick walls and floor. A 1.27 cm thick stainless steel removable lid captures the outer race of the top bearing. The vessel is liquid tight up to a height sufficient to contain all 110 l of sodium in the unlikely event of a catastrophic rupture of the sphere. There are three removable acrylic windows in the sides. The base bolts to the floor of the cylinder and the outer race of the top bearing is seated in the lid.

2.2 **Cooling**

The cooling system provides an approximate constant temperature boundary condition at the inner sphere surface. As mentioned above, kerosene is pumped through the interior of the inner sphere at a constant temperature and flow rate. The temperature of the kerosene is modulated (between 50 and 100 C) with a heat exchanger to a chilled water loop and also flexible strap heaters wrapped around part of the coolant piping. The temperature was controlled to within 0.2 ° C. Implemented in a Labview program, a PID algorithm controls a valve in the chilled water line feeding the heat exchanger. The trottle valve is a needle valve with about 6 turns from closed to fully open position. The valve stem is rigidly coupled to a stepper motor with a 4:1 gear ratio so that 1560 steps equals one full turn of the valve. The stepper motor is controlled by the Labview program using the parallel port of the computer for digital output. The process variable for the control algorithm is provided by a Keithley 2182 nanovoltmeter/thermocouple meter reading a thermocouple attached to the outside of a copper pipe in the kerosene loop. A National Instruments GPIB card provides communication between the computer and the Keithley 2182. A pair of thermocouples is also used to measure the temperature difference between the kerosene entering and exiting the sphere. This measurement can be used to approximate the global heat transfer through the system. The flow rate of the kerosene is not actively controlled, rather the pump is allowed to run at full speed with no changes in the kerosene loop plumbing. The only causes for variability in flow rate are changes in the pressure drop across the sphere when the rotation rate is changed and different amounts of entrained gas in the kerosene. These differences affect the flow rate from day to day, but not during the collection of data for a given steady state measurement. Most of the pipes in the kerosene loop are insulated with flexible polyethylene foam tubes to reduce heat loss to room air when the kerosene is very hot (up to 98 ° C for the lowest temperature drops between the inner and outer sphere). The lower limit for the temperature drop across the sodium is determined by how hot

Rotation rate (Hz)	ΔT (°C)	Rayleigh number
3	2.1-19.8	$4.2 \times 10^6 - 3.8 \times 10^7$
5	2.9-20.4	$1.6 \times 10^7 - 1.1 \times 10^8$
10	1.7-18.9	$3.8 \times 10^7 - 4.2 \times 10^8$
15	0.7-18.1	$3.5 \times 10^7 - 9.1 \times 10^8$
20	1.1-16.0	$9.8 \times 10^7 - 1.4 \times 10^9$
25	0.6-14.7	$8.4 \times 10^7 - 2.8 \times 10^9$

Table 2.2: Range of temperature drops and Rayleigh numbers achieved for different rotation rates. The lower limit for ΔT was set by the maximum temperature of the cooling fluid, which was limited by heat loss to room air in the coolant pipes. The upper limit for ΔT was set by the power of the heater or the cooling capacity of the kerosene heat exchanger, depending on the rotation rate.

the kerosene is. It is therefore imperative to minimize heat loss from the piping when taking low temperature drop data.

2.3 Heating

The outer surface of the sphere is maintained at an approximate constant heat flux boundary condition with an array of stationary heat lamps. The total heat transfer through the system is limited by the heaters. Table 2.2 shows the range of temperature drops and Rayleigh numbers reached for each rotation rate.

Heat is provided by up to 10 kilowatts of infrared short wave heat lamps (Heraeus 63061). Twenty 500 Watt bulbs are fixed to a stationary, curved frame about 2.54 cm from the surface of the sphere. The bulbs are arranged so that the average heat flux over the surface of the sphere is close to uniform as the sphere rotates past the bulbs. That is, the light intensity is in an approximate sine distribution in polar angle. The heat lamp array is located on one side of the sphere. As long as the rotation period is small compared to the thermal diffusion time for the outer wall of the sphere, the heating is also constant in azimuthal angle. The outer wall is 2.54 cm thick titanium (thermal diffusivity 0.029 cm^2/s) so it's thermal diffusion time is of order 100 s. Data was never collected at a rotation rate lower than 3 Hz, hence the heating was azimuthally uniform. The heat lamp array is fixed to a frame surrounding the sphere made from extruded aluminum posts (from 80/20, Inc.). The members of the frame form the edges of a cube. Also mounted on each of the four sides of the frame are thin stainless steel walls. The purpose of these walls is to minimize heat transfer between the hot rotating sphere and the cooler walls of the secondary containment vessel. They reduce the heat transfer due to turbulent air stirred by the rapidly rotating sphere and they reflect more of the radiation of the heat lamps towards the sphere.

The heaters are powered by a 40 A, 300 V TCR power supply. The power supply is controlled by a computer with a PCI 6031E National Instruments data acquisition card and running a Labview program. The Labview program uses a PID algorithm to control the temperature of the outer sphere based on measurements from a thermistor embedded halfway through the outer sphere wall. The current and voltage of the heater power supply are recorded with the same Labview program for an approximate measure of the global heat flux into the system.

For experiments with the largest heat transfer, a second array of heaters was added to the setup. This six-bulb auxiliary array is very similar to the main array described above. With both the main array and auxiliary array on at full rated power, about 13 kW is delivered to the heaters.

2.4 **Rotation**

A range of rotation rates of the sphere between 3 and 25 RPS were controlled within 0.75 - 0.05 percent (better control for higher rotation rates). This allowed us to access Ekman numbers in the range $E = 4.6 \times 10^{-7} - 5.5 \times 10^{-8}$. The rotation of the sphere is maintained by a 3.35 kW DC electric motor and another PID control program. The motor is mounted to the top of the lid of the secondary containment vessel. An L series timing belt and pulley system couples the motor to the top shaft of the sphere with a 2:1 gear ratio. The rotation rate of the system is obtained using a Accu-read optical encoder (755A-07-5-1000-R-OC-1-5-STN). A 2.54 cm diameter rubber wheel is attached to the shaft of the optical encoder and is kept in contact with the outside of the drive belt. The optical encoder outputs 10000 TTL pulses/revolution. These pulses are applied to the input of CD4040 counter used to divide the pulse rate to a low enough frequency to be sampled using a National Instruments LabPC+ data acquisition card. A Labview program on a third computer counts pulses from the encoder/counter circuit and computes the rotation speed of the sphere. The program then uses this speed measurement in a PID control algorithm to control the motor power supply (2182 Lambda 80 A, 36 V). The power supply only allows for unity gain remote voltage control. Since the LabPC+ card is only capable of outputting 0-10V, it is necessary to use an amplifier between the card and the power supply to access the full 0-36V range of the supply. This amplifier is diagrammed in fig. 2.2 and is powered by a Model HV-1547 1-3000 V, 40 mA power supply (Power Designs Pacific, Inc.).

As delivered from the machine shop the sphere was axisymmetric enough to spin up to about 10 Hz before shaking due to out-of-balance was too severe to run. The sphere was balanced in-house for rotation rates up to 30 Hz. Attached to the outside of the secondary containment vessel, an accelerometer was used to measure the frequency and amplitude of the out-of-balance oscillations. At the same time, an optical sensor produced a signal with one pulse for each rotation of the sphere. By observing the phase difference between of the accelerometer signal and the optical signal and carefully adding weights to the equator of the sphere, the out-of-balance was reduced to acceptable levels for 30 Hz rotation. Two weights were added: 106g and 156g separated by $\pi/2$ in azimuthal angle around the equator.

It is perhaps of interest to the reader that the termination of data collection for this dissertation project was due to the failure of a balancing weight. That is, at around 30 Hz rotation rate, one of the weights came free from the sphere causing considerable destruction. The weights are thin slabs of lead, held onto the sphere by one 10-24 screw and a 16th inch thick stainless plate covering the lead part. At 30 Hz, experiencing about 1000 g centrifugal acceleration, the stainless plate began to bend. It bent to a large enough radius that it began to collide with heaters and

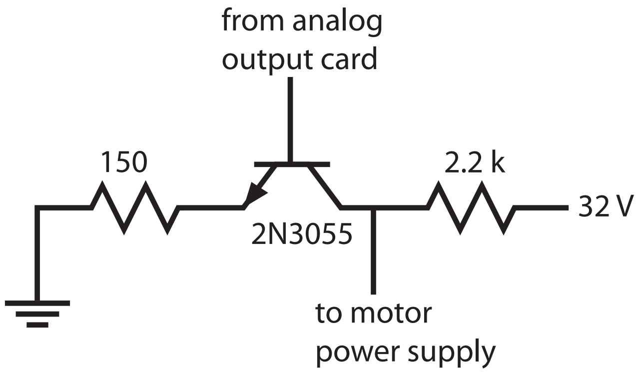

Figure 2.2: Amplifier circuit used to control motor power supply.

finally the aluminum frame around the sphere, at which point the screw holding it in place was sheared off entirely, freeing the weight. The secondary containment vessel did its job well, limiting the destruction to within its walls. It was a very loud and violent punctuation to about 1 year of data collection.

2.5 **Applied magnetic field**

In addition to the rotation rate and temperatures of the inner and outer spheres, a third control parameter is the applied magnetic field. Magnetic fields up to 3 mT were applied to the system, which for typical velocities reached in the flowing sodium, provides an Interaction parameter of order $N \equiv B^2LD/\rho\mu_o\eta U = 3.6 \times 10^{-2}$ and an Elsasser number up to $\Lambda \equiv B^2/\rho\mu_o\eta\Omega = 1.9 \times 10^{-4}$. A pair of electromagnetic coils in a Helmholtz configuration are fixed to the stationary frame so that they are concentric with the rotation axis and equidistant from the equator. They are 86 cm in diameter, each with 300 turns of 18 AWG magnet wire. Though temperature dependent, the typical maximum current through the coils, each with a 150V power supply, is around 4A.

2.6 **Filling the sphere**

The spherical vessel is filled with sodium from a 55 gallon fused drum as supplied by Dupont. The procedure followed during this transfer process is described here. There are two 1/2 inch NPT tapped holes through the outer surface or the sphere; one at the bottom and one at the top.

The bottom hole is plumbed to the drum of sodium with heated copper tubing. The top hole is plumbed to a nitrogen gas system. There is a heated stainless steel dip-tube extending to near the bottom of the sodium drum. The drum is also plumbed to the nitrogen handling system. Prior to transfer the drum and sphere are heated until the both the sodium and the sphere are near 120 C. During this phase, the sphere is pressurized, the drum is vented, and the fill line between the drum and sphere is kept cold. When the sodium and sphere reach 120 C and nitrogen gas can freely bubble through the sodium, the fill line heaters are turned on. After the fill line reaches 130 C, the sphere is vented and the drum is pressurized with about 4 PSI, thus beginning the transfer of sodium to the sphere. The plumbing from the top hole on the sphere has a section of coiled tubing (the so-called pigtail) close to the sphere. The pigtail is kept very cold with dry ice acting as a one-time shutoff valve for sodium. As the sodium is transferred to the sphere, the pigtail allows nitrogen to pass freely, but immediately freezes sodium into a solid plug when the sphere is full. When this point is reached, the sodium in the sphere is further heated to 150 C with the filling tube still full of liquid sodium (higher than the highest expected temperature during any experiment). This ensures that the sodium will never expand to a volume larger than the volume of the sphere (a sure way to cause a leak). With the sphere full of 150 C sodium, the fill line is frozen by applying dry ice. Sphere heaters are then turned off allowing the sodium to cool and contract for about five minutes. Finally the plumbing in the top hole in the sphere is replaced by a stainless steel plug. The next day after all the sodium has returned to a solid state, the fill line in the bottom hole is replaced by another plug and the filled sphere is ready to run.

Chapter 3

DATA ACQUISITION AND PROCESSING

3.1 Heat flux, temperature, and magnetic field measurements

Measurements of heat flux were made with several methods. Two heat flux sensors (Thermonetics) are attached to the outer surface of the outer sphere near the equator, separated by 50 cm azimuthally. Estimates of global heat flux were obtained by measuring the power used by the heater power supply and by measuring the temperature drop of the cooling fluid entering and exiting the sphere. The heater power overestimates the system heat flux because of losses in heating the air and secondary containment vessel. The cooling fluid temperature difference method was unreliable because no means of measuring the flow rate of the fluid was implemented. The primary and most reliable measurement of heat flux comes from a pair of thermistors at two different depths in the outer sphere wall: one at 1.35 cm from the outer surface, the other at 2.03 cm. Knowing the thermal conductivity of titanium and the temperature difference between the probes, one may estimate the heat flux with a simple calculation.

Temperature measurements were made at many locations in sphere: on the outer sphere, in the fluid bulk, and near inner sphere. A schematic of the probe locations is shown in fig. 3.1 and tables 3.1 and 3.2. Three thermistors are embedded in the wall of the outer sphere. Two of these (used for the heat flux measurements mentioned above) are located at a polar angle of $\pi/4$ and separated azimuthally by 10.6 cm. A third thermistor is embedded in the wall of the bottom hemisphere at a polar angle of $3\pi/4$. It is 2.03 cm through the wall and located at the same azimuthal angle as the thermistor at the same depth in the upper hemisphere. The thermistors in the outer wall are YSI 43A74 Veco medium beads. They are 0.1 cm in diameter. Each thermistor is placed at the bottom of a hole drilled perpendicular to the surface of the titanium wall. They are kept in place with Kapton tape, which also secures their leads flat on the surface of the sphere up to a hole in the top shaft.

A group of three thermistors (Betatherm 10MCD27) and four type E thermocouples (Omega EMQSS-035U) measure the temperature in the bulk of the convecting sodium. Located in the

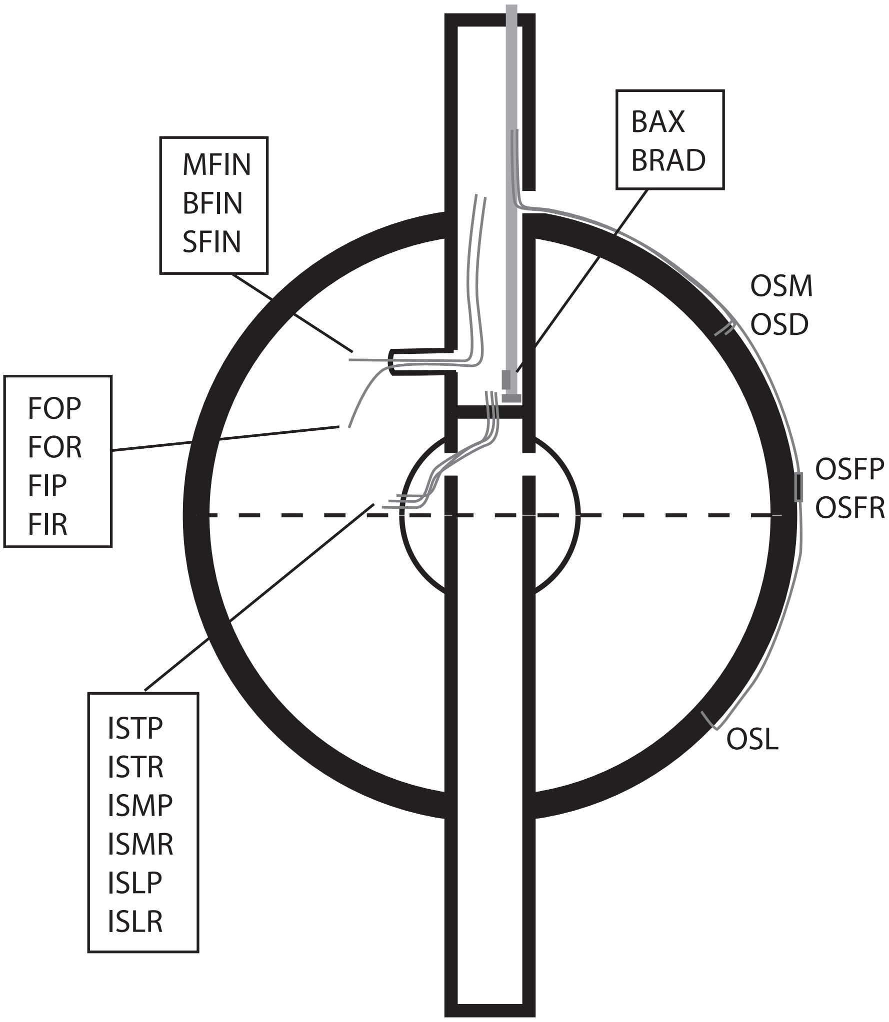

Figure 3.1: Measurements of temperature, heat flux, and magnetic field are made at locations indicated. See tables 3.1 and 3.2 for more precise position information and definitions of the labels.

probe name	**description**	**location**
MFIN	Betatherm thermistor	10.5 cm in radius from upper shaft wall 180° azimuthally from fill hole
BFIN	Betatherm thermistor	0.32 cm below MFIN
SFIN	Betatherm thermistor	0.32 cm retrograde from MFIN
FOR	thermocouple	3.43 cm directly below MFIN
FOP	thermocouple	0.23 cm prograde azimuthally from FOR
FIR	thermocouple	0.23 cm radially inward from FOR
FIP	thermocouple	0.23 cm prograde azimuthally from FIR
OSM	YSI thermistor	1.35 cm deep in outer sphere wall 45° up from equator 180° azimuthally from top fill hole
OSD	YSI thermistor	2.03 cm deep in outer sphere wall 10.64 cm prograde azimuthally from OSM
OSL	YSI thermistor	2.03 cm deep in outer sphere wall at same azimuthal angle as OSD, 45° down from equator

Table 3.1: Description and location of temperature probes in the outer wall of the vessel and in the bulk of the sodium. See fig. 3.1 for a supplementary diagram.

probe name	**description**	**location**
ISTP	thermocouple	3.08 cm above equator of inner sphere
		0.24 cm away radially from inner sphere surface
ISTR	thermocouple	0.63 cm retrograde azimuthally from ISTP
ISMP	thermocouple	2.69 cm above equator
		0.77 cm away from inner sphere surface
ISMR	thermocouple	0.63 cm retrograde from ISMP
ISLP	thermocouple	2.31 cm above equator
		1.60 cm away from inner sphere surface
ISLR	thermocouple	0.63 cm retrograde from ISLP
OSFR	heat flux sensor	2.54 cm above equator
		same azimuthal angle as OSD
OSFP	heat flux sensor	50 cm azimuthally prograde from OSFR
BAX	axial hall probe	on axis of rotation, 5 cm above inner sphere
BRAD	radial hall probe	same position as BAX

Table 3.2: Description and location of inner sphere temperature probes, heat flux sensors, and hall probes. See fig. 3.1 for a supplementary diagram.

upper hemisphere, the seven probe assembly extends into the sodium from the top shaft 13.1 cm above the inner sphere. The three thermistors are at a cylindrical radius of 16 cm. They are fixed inside of closed end, 0.165 cm diameter, stainless steel tubes. The four thermocouples are at the same cylindrical radius 3.4 cm below the thermistors. The thermistors are positioned such that two are in a vertical plane and two are in a horizontal plane perpendicular to the rotation axis.

The four thermocouples are in horizontal plane each at the corner of a square. Two pairs are approximately at equal cylindrical radius and two pairs at equal azimuthal angle. The pairs of probes are separated by 0.23 cm. Correlations between these thermocouples are used to estimate fluid velocities. The thermocouples are in ungrounded stainless steel sheaths 0.089 cm in diameter. Both the thermocouples and thermistors are silver-soldered into a the end of a 0.95 cm diameter, hollow, stainless steel tube which is mounted into a hole in the top shaft with a Swagelok pipe fitting. The leads from the probes pass through the interior of the top shaft to the data processing circuit mounted at the top of the shaft.

Six additional thermocouples are positioned near the surface of the inner sphere. They are the same type as the above mentioned thermocouples. The outer diameter of the sheaths is 0.089 cm, allowing good time response. In water the time to reach 67% of a step change in temperature is < 0.25 sec. Since sodium has a thermal conductivity which is much larger than that of water, the response time is decreased even further. The probes are silver-soldered into holes through the surface of the inner sphere. All six probes are located in a group just above the equator, arranged like the dots on the six-side of dice. One pair is 1.6 cm away from the inner sphere surface separated by 0.63 cm azimuthally. A second pair at a slightly higher polar angle is 0.77 cm away from the surface also separated 0.63 cm azimuthally. The third pair is 0.24 cm from the surface with the same azimuthal spacing. The stainless steel sheaths containing the thermocouple leads extend from where they are soldered into the inner sphere surface through its hollow interior and then through six holes at the top of the inner sphere. They are silver soldered into these holes also so that only stainless steel sheaths are exposed to the sodium and kerosene. The thermocouple leads then pass through a hole in top shaft where it meets the inner sphere and continue up to the data processing circuit.

Magnetic field measurements are made possible with hall probes (Honeywell SS94A1F) positioned just above the inner sphere inside the top shaft. Two components of magnetic field are measured with an axial probe and a radial probe.

3.2 Data processing

During an experiment, the data from ten of the probes described above is transmitted from the rotating assembly to computers, stationary in the laboratory, via an infrared link. A rotating data processing circuit, designed in-house specifically for this experiment, is mounted to the top of the top shaft. The circuit converts ten analog measurements to 12 bit digital signals. The heart of the rotating circuit is a PIC16C773 Microchip microcontroller. This small programable computer (the PIC code and instructions for burning new chips are in appendix B) is responsible for analog to digital conversion, multiplexing, and serial transmission of the data. The PIC chip has 10 analog inputs, each acquired at 50 samples/sec. The remainder of the circuit consists of amplifiers, a DC/DC converter, several voltage regulators and voltage references, and protection diodes and low pass filters for the PIC chip inputs. Mechanically, the circuit consists of three boards, stacked and mounted to an aluminum carriage which bolts to the top of the shaft. The top level of the stack is an aluminum plate with a hole on center in which the IR transmission LED is mounted.

The top circuit board in the stack provides power for the components on the other two boards. A Datel 5/1000-15/200-D12A DC/DC converter is used to produce negative voltages. It outputs -15 V, which is then passed to negative voltage regulators to create -12 V for the bottom rail of the amplifiers and -2.5 V for the hall probes. The voltages produced by the DC/DC converter were too noisy to be used without passing through a voltage regulator. Other positive voltage regulators produce 5 V for the PIC chip, 12 V for the top rail of the amplifiers, and 5 V for the hall probes. All the regulators and the DC/DC converter are fed 15.4 V from slip rings on the top shaft. When none of the protection diodes are tripped and the sodium temperature is greater than the reference temperature the circuit uses about 220 mA at 15.4 V (a useful fact for circuit debugging).

The middle board in the stack houses the PIC chip. The PIC chip has no internal overvoltage protection. Therefore, each analog input is protected with external diodes which clamp the input voltages between 0 and 5 volts. Each input also has a RC low pass filter with a cutoff frequency of about 100 Hz. The TX pin of the PIC chip is capable of directly driving the IR LED with up to 25 mA. This produces a sufficiently powerful signal as long as the receiving photodiode is not more than about 2.54 cm away. An external 20 kHz crystal is used for the PIC's clock. Also on the middle board are four sockets for AD624 or AD524 amplifiers. These were used for heat flux sensors.

The bottom board in the stack contains all the circuitry for measuring temperatures. There are four 5V voltage references for thermistors. Each thermistor is set up in a voltage-divider bridge to convert their temperature sensitive resistance into a voltage for the PIC chip. There are four AD524 instrumentation amplifiers which are used to amplify the thermocouple signals. The reference junction for the thermocouples is also on the bottom board. This consists of a 1 cm x 1 cm block of copper bolted to the board. A thermistor measures the reference temperature inside a hole in the copper block. A reference thermocouple is also in thermal contact with the copper block. Figure 3.2 shows a schematic of the circuits for the thermistors and thermocouples.

Given the temperature of the reference junction, one can deduce the temperature of the other thermocouples as follows. The temperature of a type E thermocouple junction is related to the Seebeck voltage (voltage across the T/C junction) by

$$T(V) \approx -45 + 30295V - 117000V^2. \tag{3.1}$$

Likewise the approximate Seebeck voltage for the reference thermocouple can be deduced from the measured reference temperature (thermistor measurement) with the formula

$$V_{ref}(T_{ref}) \approx 5.867 \times 10^{-5} T. \tag{3.2}$$

Since the voltage V at the amplifier inputs is the sum of V_{ref} and the voltage from the

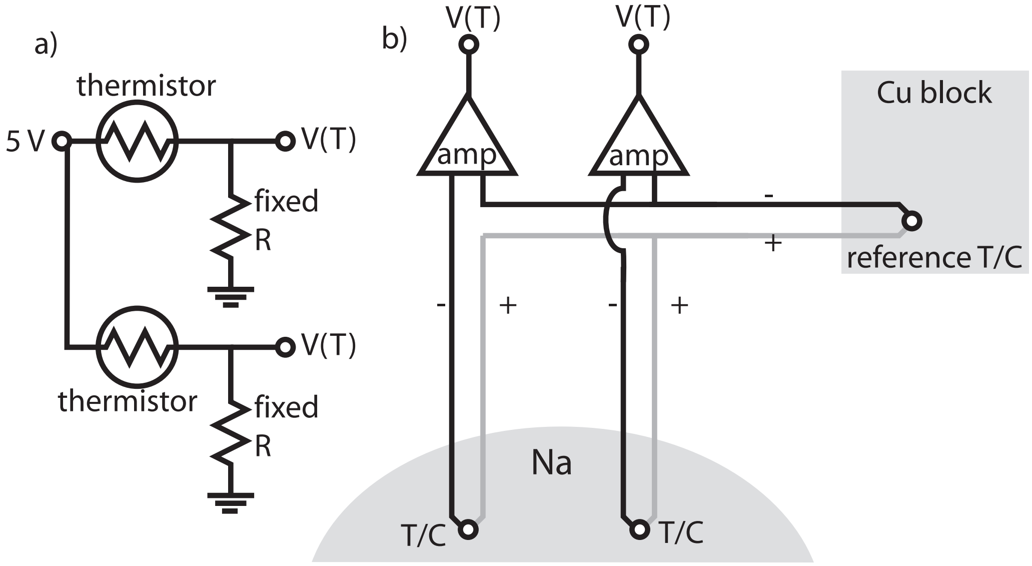

Figure 3.2: Circuit schematics for (a) thermistors and (b) thermocouples.

measuring thermocouple V_m, the temperature at the measurement location is

$$T_m(V, V_{ref}) = T(V - V_{ref}) \approx -45 + 30295(V - V_{ref}) - 117000(V - V_{ref})^2 \tag{3.3}$$

Equations 3.1 and 3.2 are approximations of NIST polynomials for Type E thermocouples. These conversion formulas are accurate enough to maintain a level of uncertainty in temperature measurements on the level of factory calibration. More precise individual calibrations are necessary to achieve ±0.2 °C. Calibration procedures are described in the next section of this chapter.

The transmission IR LED is parallel to and coaxial with the rotation axis pointing straight up. Just above the rotating, emitting LED in the stationary frame there is a receiving circuit with a photodiode (Phontonic Detectors, Inc. Type PDB-C140). The receiving circuit basically consists of a the photodiode, a comparator, and a TTL to RS232 converter. The digital signal from the rotating circuit is captured by the photodiode, brought back to TTL levels (0-5V) with the LM311 comparator and then converted to RS232 levels (+-12V) with the MAX232 converter. The signal is then passed to a PC through the serial port. The incoming data on the PC is handled by a Labview program. The Labview program (see appendix B for the code) collects a four second time

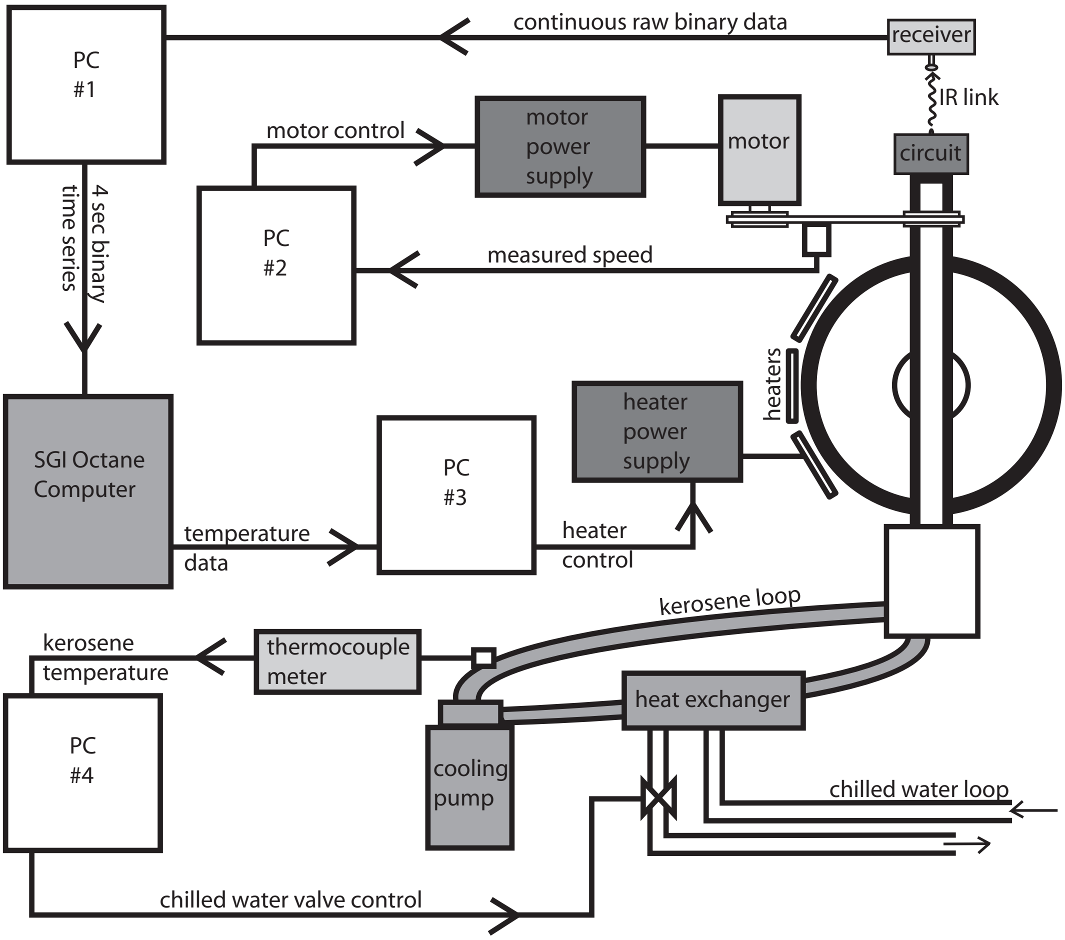

Figure 3.3: Data processing and system control block diagram.

series from the serial port and writes the binary data to a temporary location on an SGI Octane on the network. The Octane converts the raw binary data to ASCII and writes it to disk. In addition the Octane computes temperatures on-the-fly from the voltage data which is then sent to the PC which controls the heater power supply. The same Labview code that controls the heaters on this PC also displays the temperature data in real time and writes heater power measurements to disk on the Octane. Both the Labview code and the PID algorithm (also coded in Labview) are presented in appendix B. A block diagram of the entire data collection and control system is shown in figure 3.3.

3.3 Calibrating temperature probes

In order to make accurate measurements of heat flux, it is necessary to measure accurate differences between two temperature probes. This accuracy is also critical for determining the Rayleigh number for small temperature drops from the innner to the outer sphere. As supplied from the manufacturer, both thermistors and thermocouples are generally not accurate enough (within about 5% of factory calibrations). Therefore, in-house calibration was performed for all the temperature probes discussed in above sections.

With all the probes in the position where they would remain during experiments, the sphere full of sodium was heated up to 130 °C with strap heaters fixed onto the outside of the sphere with Kapton tape. The temperature was never above 130 °C in steady state for the presented experiments. The sphere was then wrapped tightly with 2 layers of R-19 fiberglass insulating batting and one layer of aluminum foil. The heaters were then shut off and the temperature of all the probes in the system was monitored for about 12 hours. During this period the temperatures slowly drifted down with the system in a nearly isothermal state. From the rate of change of the temperature and the thermal mass of the system an estimate of the heat loss and maximum temperature gradients between probes may be calculated. The system typically took 6.7 hours to drop about 15 °C. The power lost to cooling is then related to the change in temperature ΔT of the sodium and the titanium vessel,

$$\begin{aligned} \frac{Q_{tot}}{Time_{tot}} &= \frac{(mc_p\Delta T)_{Na} + (mc_p\Delta T)_{Ti}}{Time_{tot}} && (3.4) \\ &= \frac{(110000g)(1.42J/g^{\circ}C)(15^{\circ}C) + (150000g)(0.526J/g^{\circ}C)(15^{\circ}C)}{2.4\times 10^4 s} && (3.5) \\ &= 147W. && (3.6) \end{aligned}$$

Spread over the surface of the sphere, this is 0.0130 W/cm^2. The largest temperature gradient is expected in the titanium wall since it is a worse heat conductor than the sodium. This implies a drop in temperature of about 0.1 °C between the probes (OSM and OSD) embedded in the outer sphere which are used for the heat flux measurements. With the maximum gradient in mind, all the probes are calibrated with respect to the factory calibration of one of the thermistors (OSM).

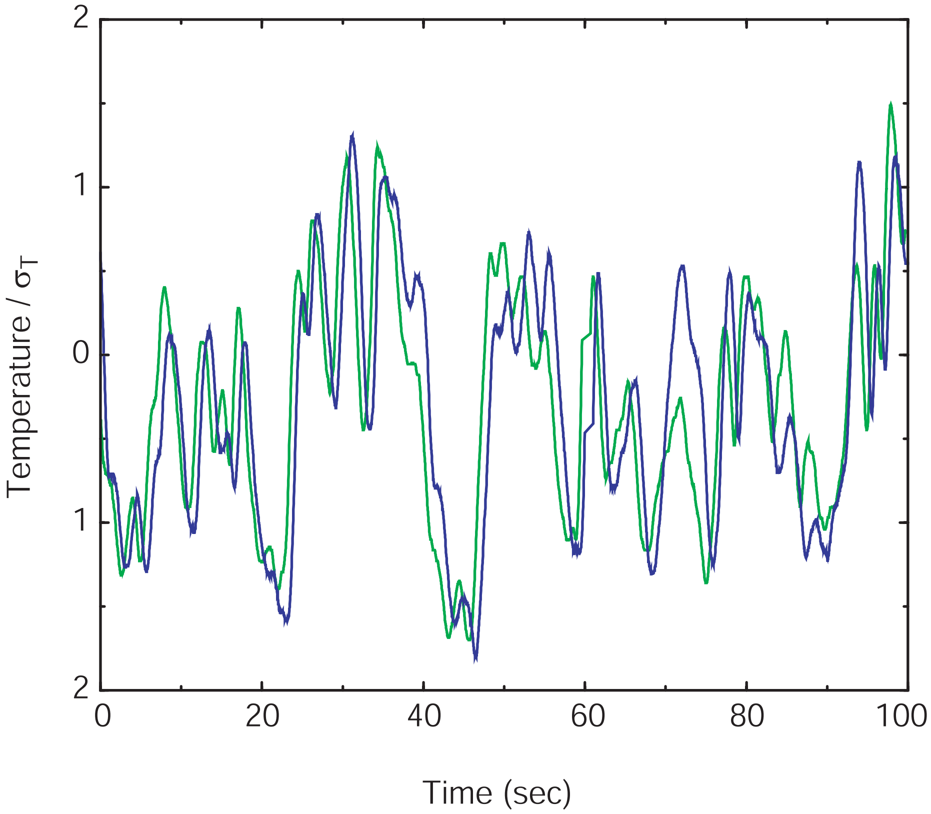

Figure 3.4: Two typical time series from closely spaced temperature probes. We interpret the delay between the the signals to be caused by the zonal fluid velocity as it sweeps temperature structures past the probes.

The result is that all probes are correct with respect to each other to within 0.2 °C but only as good as the factory calibration for absolute temperature measurements.

3.4 **Velocity measurements**

Time series of temperature at two nearby positions in the sodium may be used to obtain local estimates of the fluid velocity. Closely spaced groups of temperature probes are located near the inner sphere surface and also in the bulk of the flow as described in the previous section. As temperature structures are swept past a pair of temperature probes, the time series of one probe closely resembles the other, but with a slight time delay. Fig. 3.4 shows a short sample of two such time series. This delay is approximately the time it takes for the fluid velocity to carry the temperature field across the distance d between the probes.

One may be confident that the time delay in the temperature time series truly reflect the fluid velocity for several reasons. First, the time series are highly irregular due to the turbulent nature of the convection. This is true as close to the onset of convection as the apparatus allows measurement. This means that one need not worry that the correlations between the time series are due to spatial or temporal periodicity. Furthermore, temperature variations in a single time series are often much slower than the peak delay in mutual information. This ensures that the correlations are not spurious. A drawback to this method is that it is not possible to detect the difference between a fast moving temperature structure and a temperature structure that is moving at some angle with respect to the line between the probes. That is, a temperature front which hits the probes at the same time, approaching from right angles to the line between the probes will appear to have zero delay, or infinite velocity. A second problem with the technique is that resolution of velocity measurements decreases as velocity increases. The higher the fluid velocity, the shorter is the delay time. Thus, the highest velocity one could hope to measure is limited by the time resolution of the data acquisition. The velocity is

$$v = \frac{d}{\tau}, \tag{3.7}$$

which implies the error in v is

$$|\delta v| = \frac{d}{\tau^2}\delta\tau. \tag{3.8}$$

The delay is obtained using an algorithm which computes difference vectors constructed from short sections of the time series. Given two discrete time series A_t and B_t two m-dimensional vectors $\mathbf{a}_n$ and $\mathbf{b}_{n+\tau}$ are constructed,

$$\mathbf{a}_n = (A_n, A_{n+1}, ...A_{n+m}) \tag{3.9}$$

$$\mathbf{b}_{n+\tau} = (B_{n+\tau}, B_{n+1+\tau}, ...B_{n+m+\tau}). \tag{3.10}$$

Here $\mathbf{b}_{n+\tau}$ is constructed with a delay of τ points with respect to $\mathbf{a}_n$. The magnitude ϵ of the difference vector is then

$$\epsilon = |\mathbf{a}_n - \mathbf{b}_{n+\tau}| = \sqrt{(A_n - B_{n+\tau})^2 + (A_{n+1} - B_{n+1+\tau})^2 + ...(A_{n+m} - B_{n+m+\tau})^2}. \tag{3.11}$$

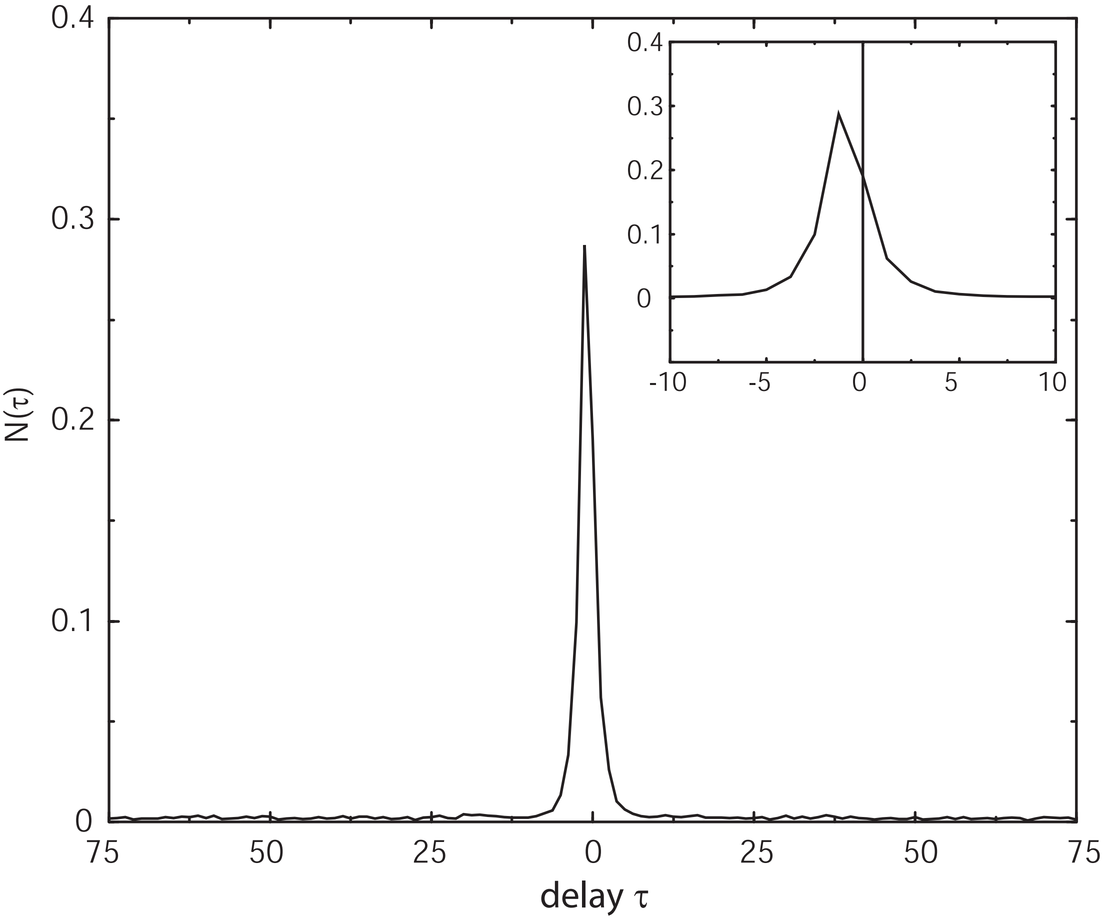

Figure 3.5: A typical distribution of τ delays. The inset shows a blowup of the peak, clearly offset from zero indicating an average fluid velocity which carries temperature structures from one probe to another.

For a given $\mathbf{a}_n$ the difference vector is computed for every value of τ, so that $\mathbf{b}$ is a moving boxcar sweeping through the full length of B_t. This process is repeated such that $\mathbf{a}$ also sweeps through all of A_t. Throughout the computations a running tally is kept of number of occurrences with $\epsilon < 0.1$ for each value of τ. The end result is a histogram or probability density function for delay times τ. An example τ distribution is shown in fig. 3.5. The expectation value of is computed for values of τ with a count of more than 80 percent of the count of the most probable τ. This value is used to determine the peak of this histogram with better resolution the original sampling rate size. The probe separation divided by this peak τ is taken as the mean velocity of the fluid.

The velocity measurements presented in this dissertation are taken from pairs of probes at equal radius and height, separated azimuthally. That is, they probe the azimuthal component of velocity. The probe configuration is motivated by the prevalence of strong azimuthal or zonal flows in rotating convecting flows such as the experiment presented here. One pair of probes is located near the inner sphere surface. The other pair is located in the bulk of the flow approximately halfway between the inner sphere and outer sphere.

Chapter 4

RESULTS AND INTERPRETATIONS

4.1 General features and observations

The data presented in this chapter are the product of many experiments conducted with the apparatus and instrumentation described in chapters 2 and 3. All the data was recorded while the system was in steady state. A typical day's experiment involved running at a constant rotation rate Ω and varying in steps the temperature drop ΔT from the outer to the inner sphere. Some experiments were also done at constant Ω and ΔT while varying an applied magnetic field. Reaching a steady state was a rather slow process, typically taking between 40 minutes and 1 hour. This settling time, although not measured, seems to decrease for higher rotation rates of the spherical vessel, consistent with the fact that at higher Rayleigh number, convection more vigorously mixes the fluid. This is not obvious since Coriolis forces also increase with rotation rate and tend to inhibit the convective motions. Perhaps the fact that buoyancy wins out is simply because buoyancy forces increase as Ω^2 while Coriolis forces increase only linearly in Ω. The system was considered to be in a steady state when the mean temperatures at the inner sphere, mid-gap, and outer sphere as well as heat flux at the outer sphere remained unchanging for more than 20 minutes. Once in a steady state, time series were acquired, typically around 900 seconds long with a sample rate of 50 Hz. It was necessary to monitor all three temperatures, because the radial dependence of average temperature was observed to change with rotation rate and ΔT. Specifically, the temperature was always within 20% of the value expected for a conductive temperature profile, but at low ΔT, the midgap temperature is closer to the outer sphere temperature and decreases towards that of the inner sphere as the convection becomes more vigorous. This effect is evident in fig. 4.1. This results in an increased settling time, which is consistent with the idea that to reach a steady state, one must wait for the excess heat to be extracted by the cooling system as the bulk of the fluid approaches a lower mean temperature. In fig. 4.1, the temperature drop from mid-gap to inner sphere divided by the full temperature drop ΔT is plotted for different ΔT and rotation rates. These results are in contrast with measurements of average temperature as a function of radius for

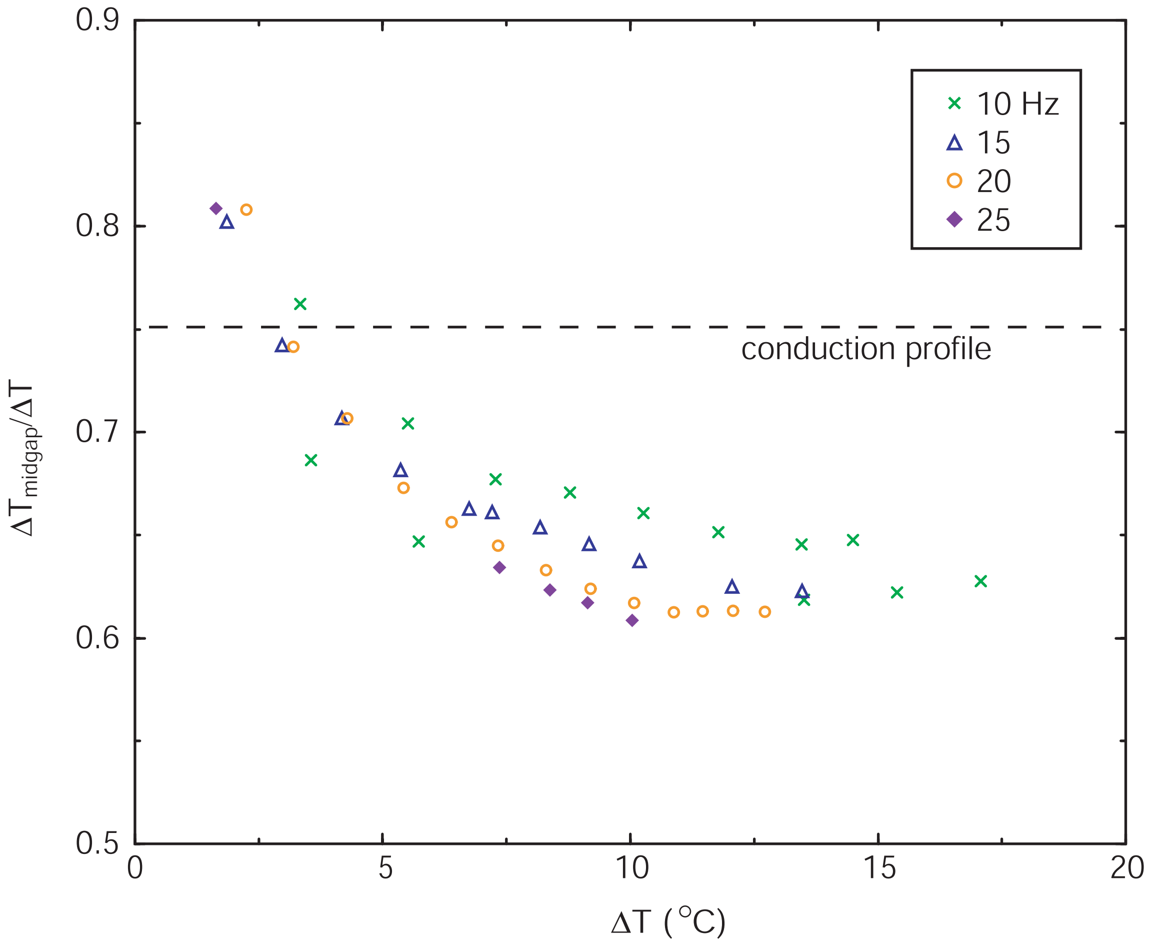

Figure 4.1: The temperature field rearranges for different rotation rates and temperature drops, but is always near the conduction profile (dashed line). The ordinate data is $\frac{T_{midgap}-T_{inner}}{\Delta T}$.

Rotation rate (RPS)	m_c	ΔT_c	Ra_c
3	11	6.88	1.38×10^7
10	19	2.52	5.61×10^7
15	21	1.71	8.57×10^7
20	23	1.30	1.16×10^8
25	23	1.07	1.49×10^8
30	25	0.91	1.82×10^8
40	28	0.72	2.57×10^8

Table 4.1: These critical values of wavenumber and ΔT were computed by Gillet using a quasi-geostrophic model with our parameter values and geometry.

similar experiments in water and silicon oil by Sumita and Olson. [61], [62]. They observed the opposite trend in mean temperature of the bulk fluid: it approached the outer sphere temperature as Ra was increased. The most obvious difference between our experiment and theirs is that the Prandtl number of sodium is 0.01 compared to 7 and 14 for water and silicon oil respectively. We also spun the sphere at much higher rotation rates, thus achieving lower Ekman numbers.

It should be noted that the apparatus is not well suited for measurements near the onset of convection. At all observed ΔT values, above and below the expected onset of centrifugally driven convection, turbulent fluctuations of temperature were observed. This is probably due partially to the nature of low Prandtl number convection and partially to some form of natural convection, which, ignoring Coriolis effects has a much lower critical ΔT as discussed in chapter 1. The expected values for the onset of convection in our system were calculated for us by Nicolas Gillet [26] using the quasi-geostrophic code developed by Aubert, Gillet, and Cardin [3]. His results for the critical ΔT and azimuthal wavenumber m are shown in figs. 4.2 and 4.3 and tabulated in table 4.1. The wavenumber results are consistent with Roberts' asymptotic theory, while the critical ΔT results seem to fall in between the Roberts scaling for large Pr and the Zhang scaling

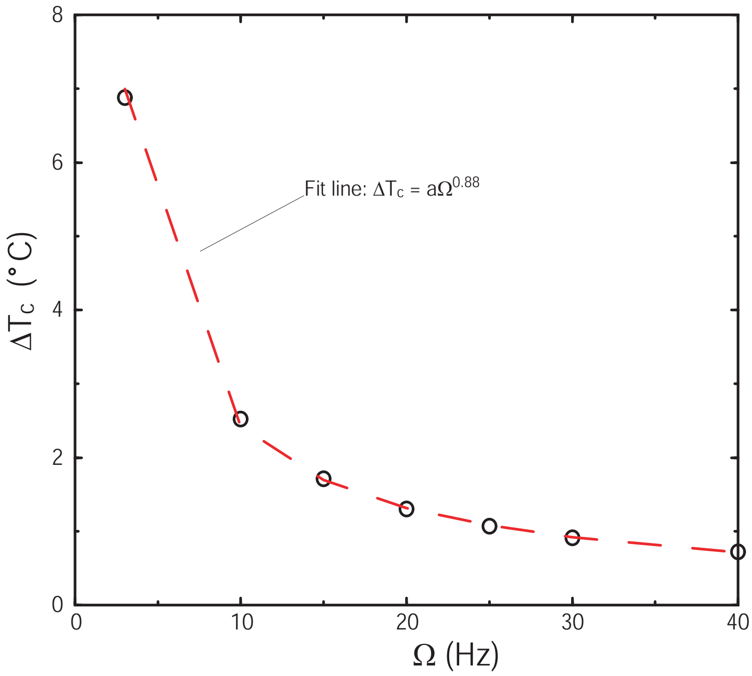

Figure 4.2: Shown are the onset values of ΔT for centrifugal convection at different rotation rates. The data were computed by Gillet [26] using a quasi-geostrophic numerical model with our parameter values and geometry.

for very small Pr. Gillet's results were

$$m_c \quad \propto \quad \Omega^{0.35} \sim E^{-1/3}, \tag{4.1}$$

$$\Delta T_c \quad \propto \quad \Omega^{-0.88} \Longrightarrow Ra_c \sim E^{-1.12}. \tag{4.2}$$

$$\tag{4.3}$$

In other experiments ([61], [2]) where flow visualization was possible (either with dye or flakes in water or with ultrasound in gallium) it has been observed that the typical size of vortices that form at onset remains close to the typical length scale for more complicated motion as the convection becomes more vigorous. For this reason $1/m_c \sim D\Omega^{-1/3}$ will be used as a typical length scale in several of the arguments used to understand the data in later sections of this chapter. The critical values of ΔT provided by Gillet will also be used.

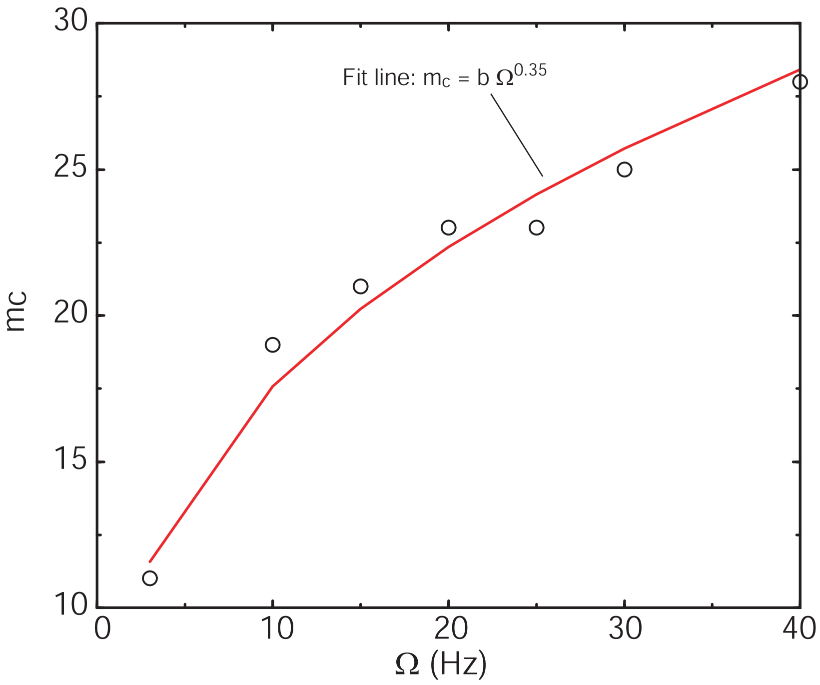

Figure 4.3: The critical azimuthal wavenumbers are shown for flow structures at the onset of centrifugal convection. The data were computed by Gillet [26] using a quasi-geostrophic numerical model with our parameter values and geometry.

4.2 The big picture: some conjectures

Considered together, the results in upcoming sections of this chapter suggest a general picture of the velocity and temperature dynamics for these experiments. Let me describe the general picture before delving into the supporting details. The velocity field seems to be well described by two parts: a large scale retrograde zonal wind and a smaller scale turbulent velocity responsible for the convective heat transfer. The scale of the zonal flow is characterized by $U_\phi \sim \Omega D \alpha \Delta T$, which suggests a balance between Coriolis and buoyancy forces (or possibly the presence of thermal winds). The smaller scale convective velocities seem to scale as $U_c \sim \Omega D \sqrt{\alpha \Delta T}$, which suggest a balance between inertial and buoyancy forces. The velocity field is most active near the inner sphere and seems to be characterized by a persistent length scale $\delta \sim E^{1/3} D$. A likely scenario is that buoyancy drives outward radial motion near the inner sphere where heat flux per unit area is greatest and these radial motions are deflected by Coriolis forces into a zonal flow. Since sodium has such a low viscosity (0.007 cm^2/s) the slightest shear in the flow caused by the buoyant motions or the zonal motions induce turbulence. A Reynolds number $Re \equiv UL/\nu$ based on the typical zonal flow is around 40000. In spite of the turbulence, the heat transfer is still not more than twice that due to conduction. The mean radial temperature profile is within 20% of the conductive profile throughout our measurements. The turbulence of the velocity field creates fluctuations in temperature, which are swept around the vessel by the zonal flow. It is analysis of these temperature fluctuations that provide the majority of our results.

4.3 Temperature standard deviation

Measurements of temperature in these experiments are the backbone of most of the results presented in this chapter. This section is devoted to presenting and explaining the behavior of the magnitude of the temperature fluctuations. I will first show some typical time series for different rotation rates and ΔT values. These sample time series were measured very close to the equator of the inner sphere (ISTP as defined in chapter 2). As is evident in fig. 4.4 the size of temperature fluctuations increase as ΔT is raised and decrease as Ω is increased. The Coriolis forces apparently suppress the fluctuations, while buoyancy forces excite them.

The standard deviation of temperature fluctuations for many different rotation rates and temperature drops are shown in fig. 4.5. The trends suggested by the sample time series in fig. 4.4 are clear. A simple argument based on advection of temperature structures by a mean zonal velocity may be used to explain the observed behavior in standard deviation of temperature. Consider velocity structures in the flow of size $\delta \sim E^{1/3}D$ which are swept past the temperature probe. If the velocity structures are mixing a fraction δ/D of the full temperature drop ΔT, then we can expect temperature fluctuations of size

$$\sigma_T \sim \frac{E^{1/3}D}{D}\Delta T, \tag{4.4}$$

$$\sigma_T \sim E^{1/3}\Delta T. \tag{4.5}$$

This scaling is borne out clearly in fig. 4.6. The dashed line in fig. 4.6 is a linear fit with the following equation

$$\sigma_T = 4.0\ E^{1/3}\Delta T. \tag{4.6}$$

4.4 Temperature probability density functions

The probability density function (PDF) for a passive scalar in turbulent convection has been shown to exhibit Gaussian statistics for Rayleigh numbers that are small enough (e.g. [16], [63], [51]). For greater Rayleigh numbers, in the so-called *hard turbulence* regime, the PDF often exhibits exponential tails (e.g. [33], [28]). A review of passive scalars in turbulent flows is given by Warhaft [68].

Temperature PDFs for two rotation rates, 3 and 15 Hz, are shown in figs. 4.7 and 4.8. The PDFs are constructed from time series acquired close to the inner sphere equator. For the lower rotation rates the PDFs are more skewed to towards negative temperatures. For higher rotation rates the PDFs are still slightly skewed, but closer to Gaussian, though slightly super-Gaussian in the positive tail. In general, it seems that low amplitude cooler-than-mean events are most

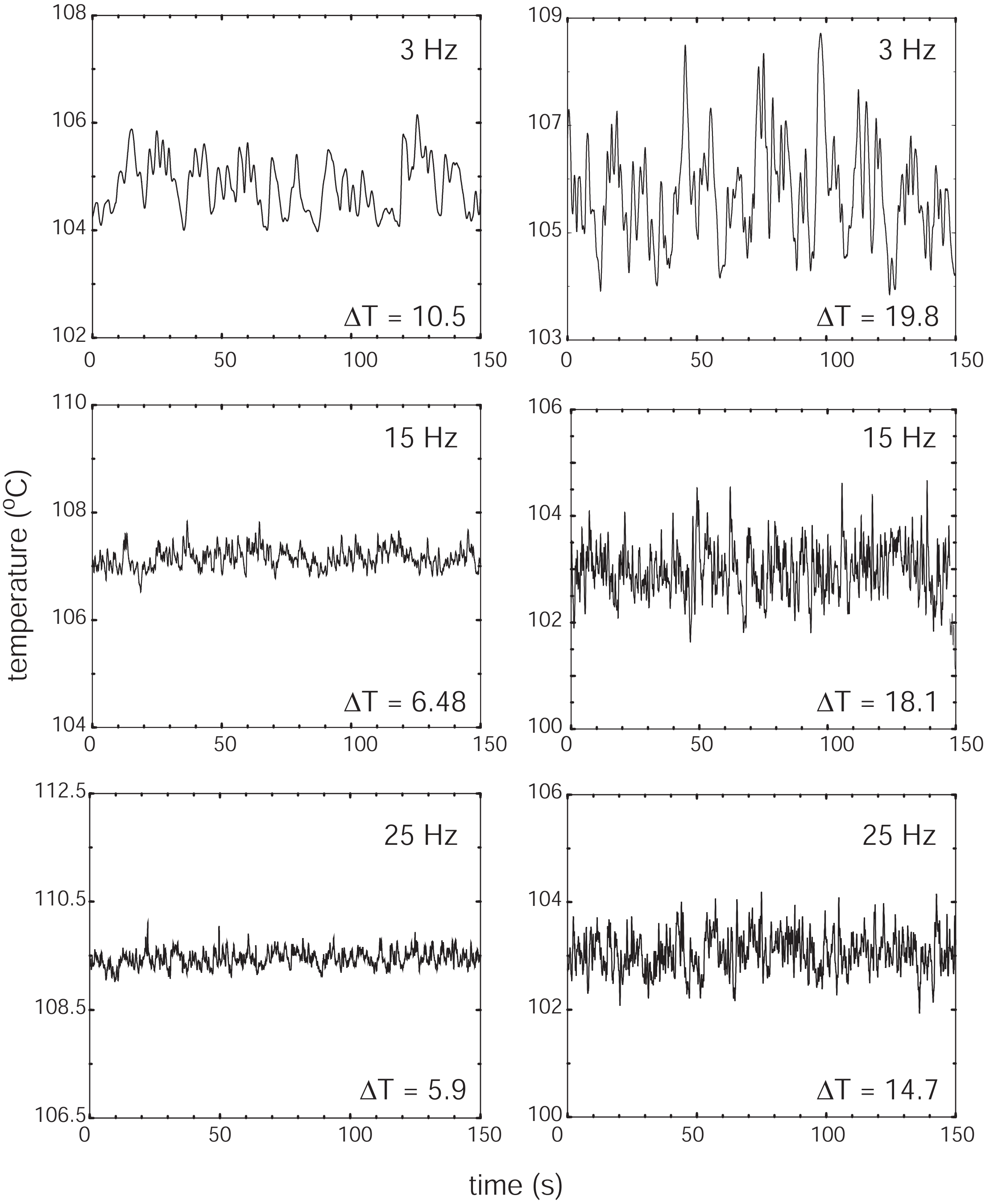

Figure 4.4: Typical time series are shown for rotations rates of 3 Hz (top), 15 Hz (middle), and 25 Hz (bottom), each with a low ΔT (left) and a high ΔT (right) example. These time series were acquired near the equator of the inner sphere.

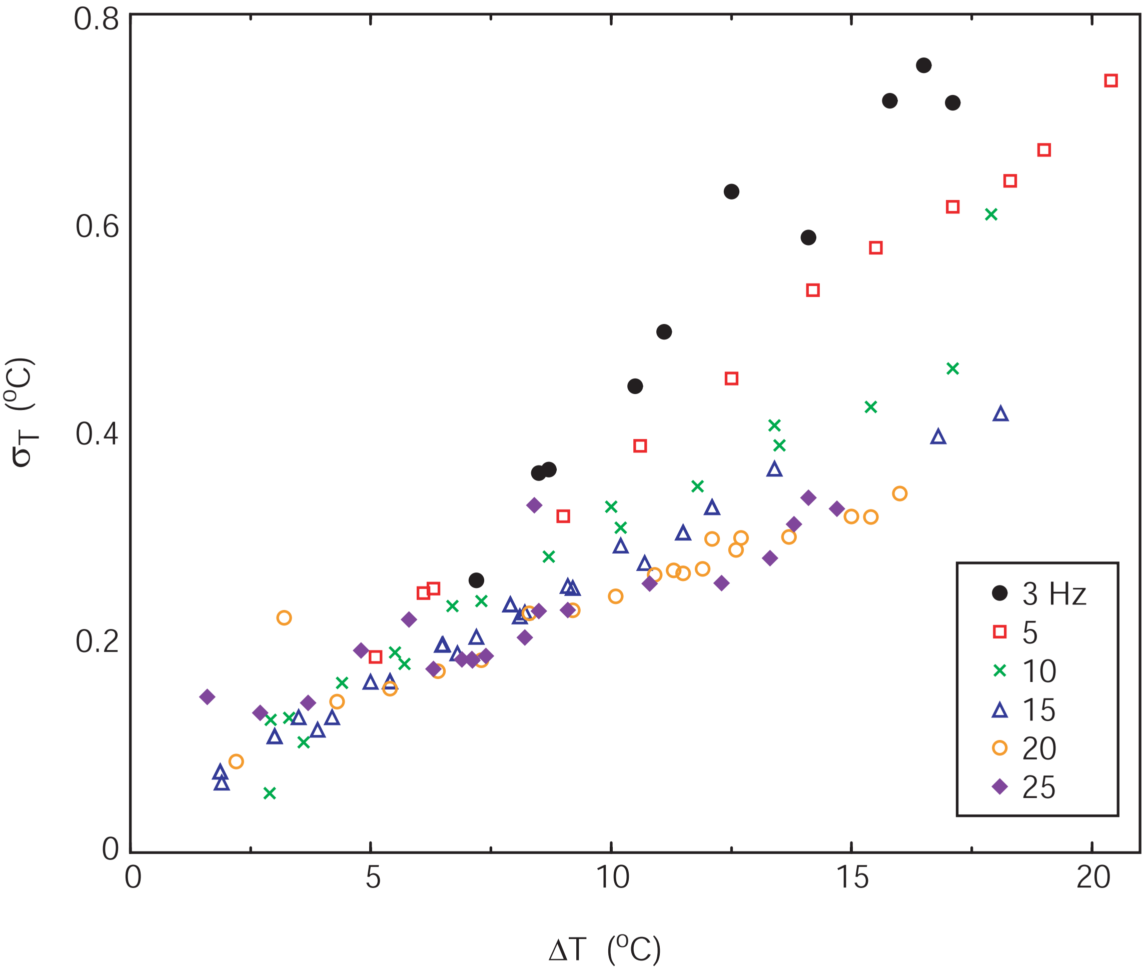

Figure 4.5: Standard deviation is plotted as a function of temperature drop for a range of rotation rates. The size of the fluctuations increases with ΔT and decrease as rotation is increased.

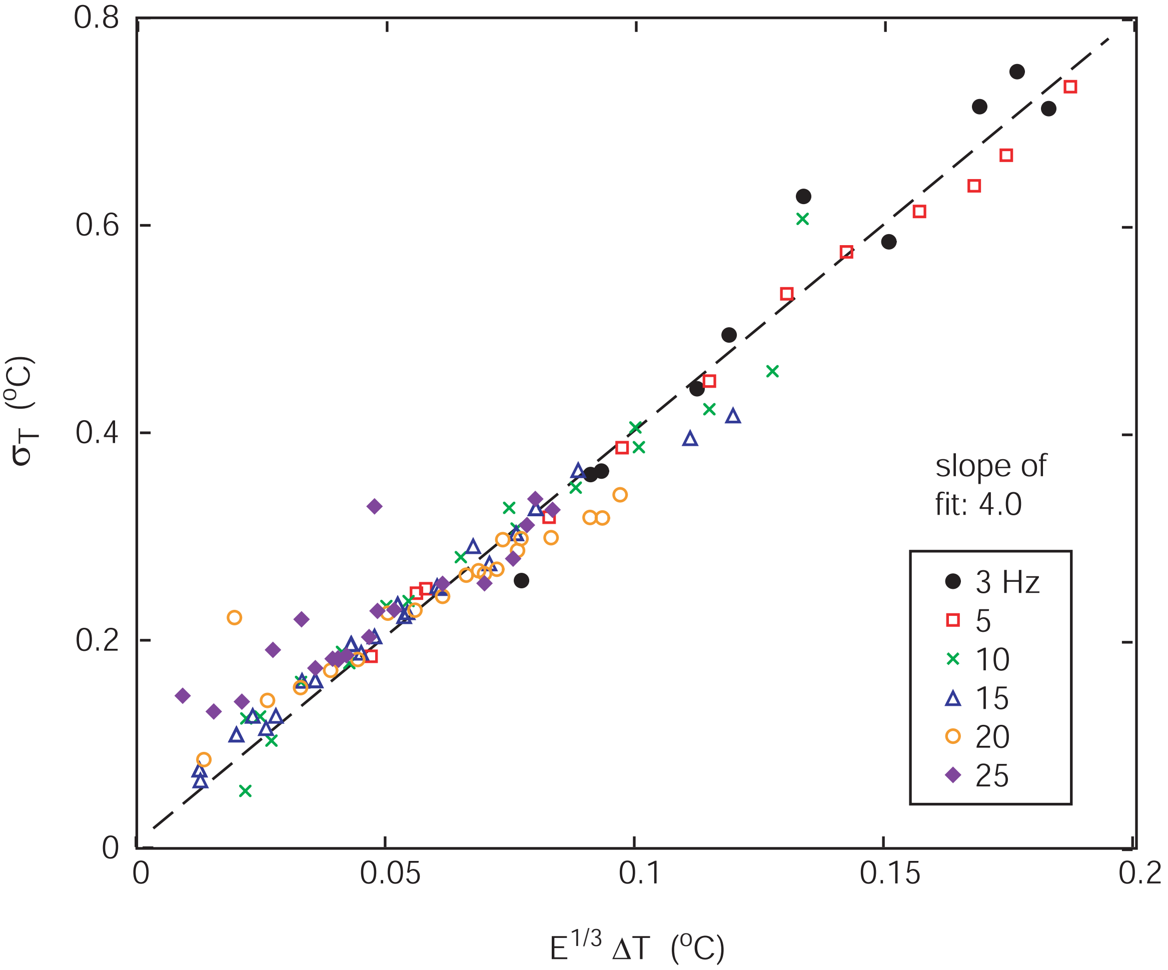

Figure 4.6: The standard deviation of temperature is related linearly to the temperature drop scaled by $E^{1/3}$. The dashed line is a linear fit with prefactor of 4.0.

likely, while extreme warm events are more likely than extreme cold events. This is probably because, near the inner sphere, the mean is close to the temperature of the inner sphere and events colder than the inner sphere temperature are impossible. The trend towards Gaussian statistics is probably a reflection of the stronger turbulence accompanying higher Ra at high rotation rates. The warm tail tail may show hints of a hard turbulence regime.

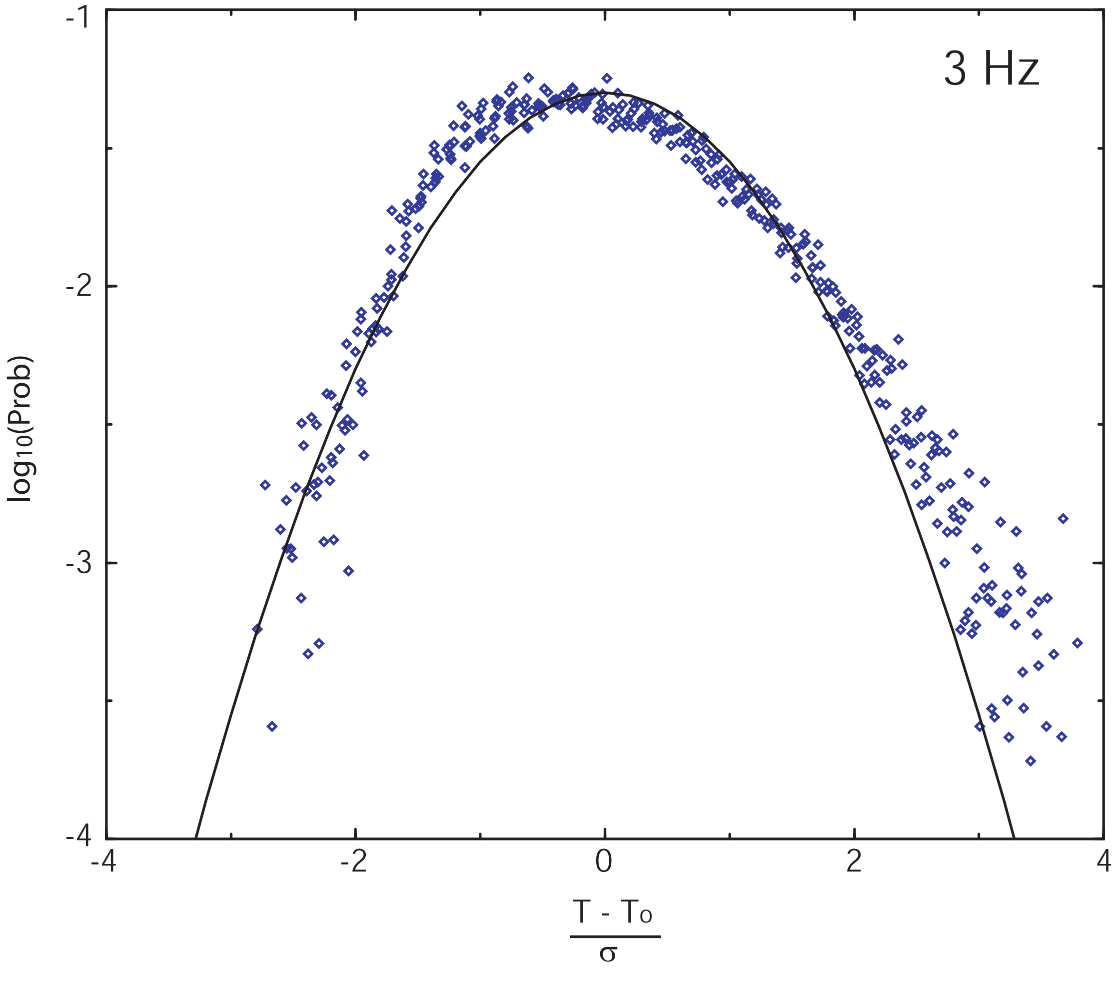

Figure 4.7: The points in the PDF are taken from many time series with different ΔT, but all with rotation rate of 3 Hz. The source time series were all scaled by their standard deviation.

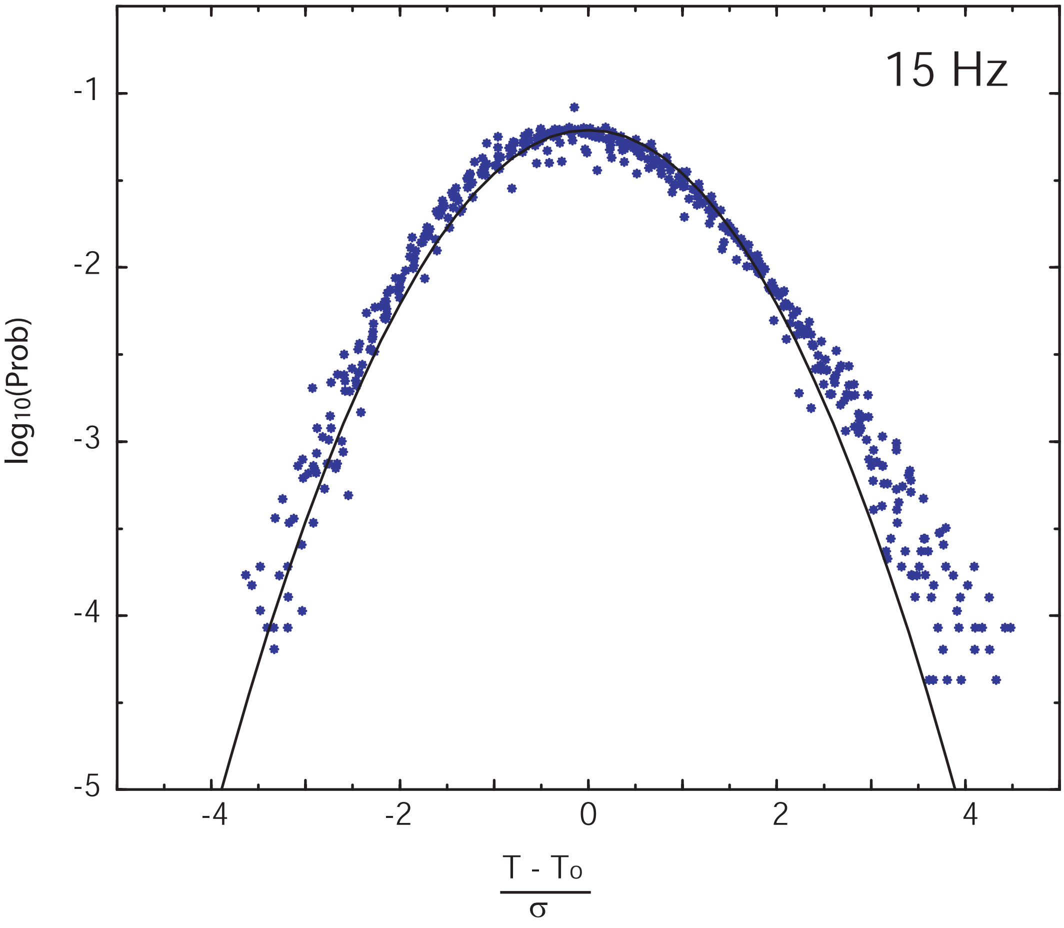

Figure 4.8: The points in the PDF are taken from many time series with different ΔT, but all with rotation rate of 15 Hz. The source time series were all scaled by their standard deviation.

4.5 **Zonal velocity**

As discussed in chapter 3, estimates of zonal velocities were obtained by computing average delay times between temperature time series acquired from azimuthally separated probes. The resulting velocities were retrograde with respect to rotation near the inner sphere where the measurements were taken. Velocities for different rotation rates are plotted against ΔT in fig. 4.9. Due to time resolution limitations, the method of obtaining velocity measurements fails for large ΔT and large rotation rates. These points are excluded from the presented data. Furthermore, data is only shown for values of ΔT greater than the predicted onset of centrifugal convection.

The velocity data may be presented in a dimensionless form with the following scalings. Velocity is divided by $D\Omega$ (i.e. Rossby number) and the temperature drop ΔT is replaced by $\alpha\Delta T_e$. The critical temperature drop and adiabatic temperature drop, as estimated in chapter 1, are subtracted from the full ΔT to form $\Delta T_e \equiv \Delta T - \Delta T_c - \Delta T_{adiabatic}$. In other words ΔT_e represents the temperature drop available to drive convection. The velocity, scaled in this way, is shown in fig. 4.10. The error bars on the points in fig. 4.10 come from uncertainty in time resolution (±0.01 s) and uncertainty in temperature difference measurements (±0.2 °C).

There are several possible explanations for a velocity that scales as $v \sim D\Omega\alpha\Delta T$. The simplest explanation stems from a balance between the buoyancy force and the Coriolis force in the Navier-Stokes equation,

$$\Omega^2 r\alpha\Delta T \sim 2\Omega \times v. \tag{4.7}$$

A heuristic justification for such a force balance comes from considering the motion of a convective plume under the influence of Coriolis forces. Buoyancy forces drive cold plumes away from the inner sphere. The initial radial trajectory of the plume is deflected by the Coriolis force into an azimuthal direction, which suggests azimuthal velocities experience the balance in eq. 4.7. A simple dimensional argument applied to eq. 4.7 yields,

$$\Omega^2 D\alpha\Delta T \sim \Omega U. \tag{4.8}$$

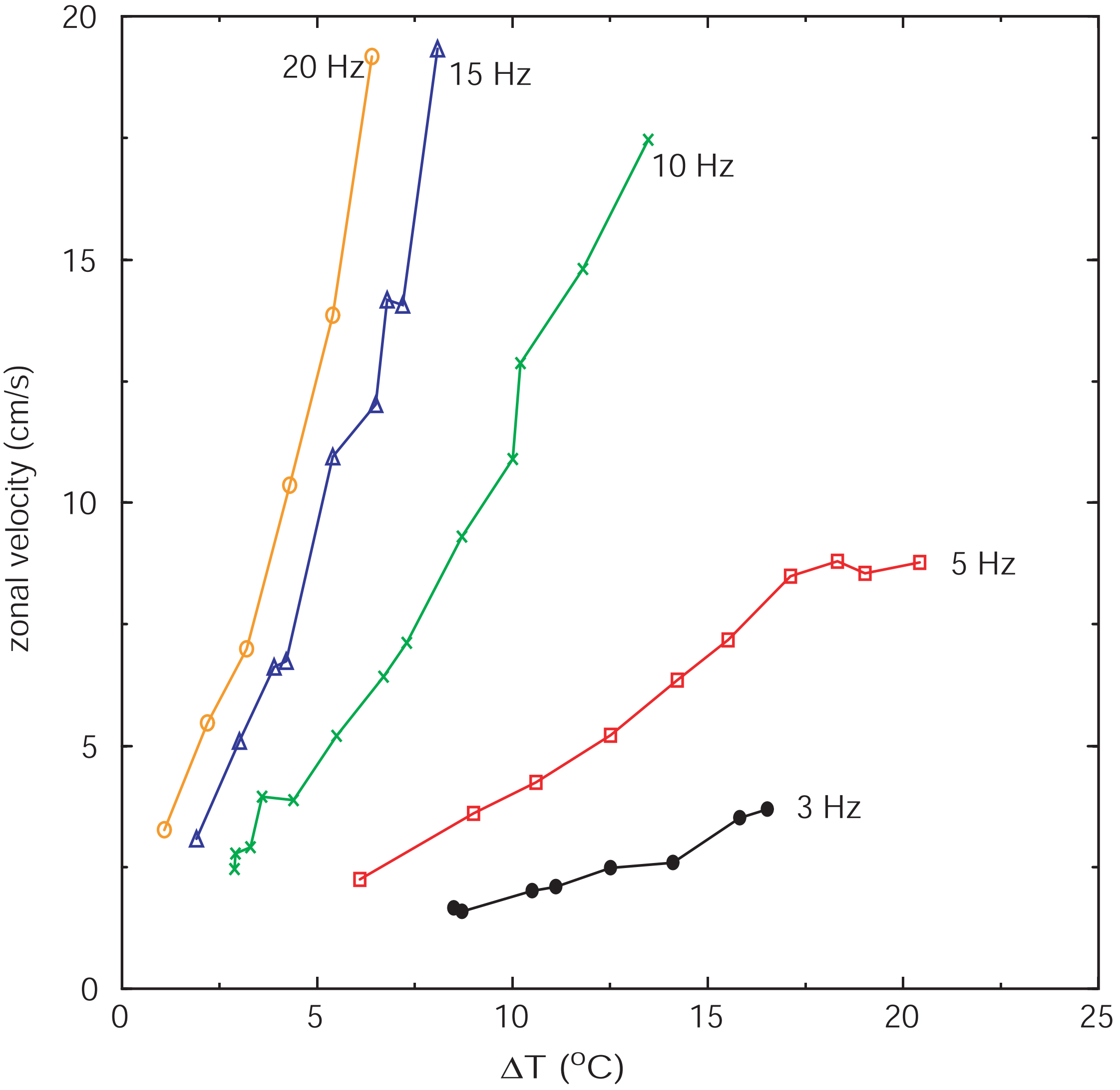

Figure 4.9: Measurements of retrograde zonal velocity for different rotation rates and temperature drops close to the inner sphere equator. Results are only shown for ΔT greater than the predicted onset of centrifugal convection for any given rotation rate.

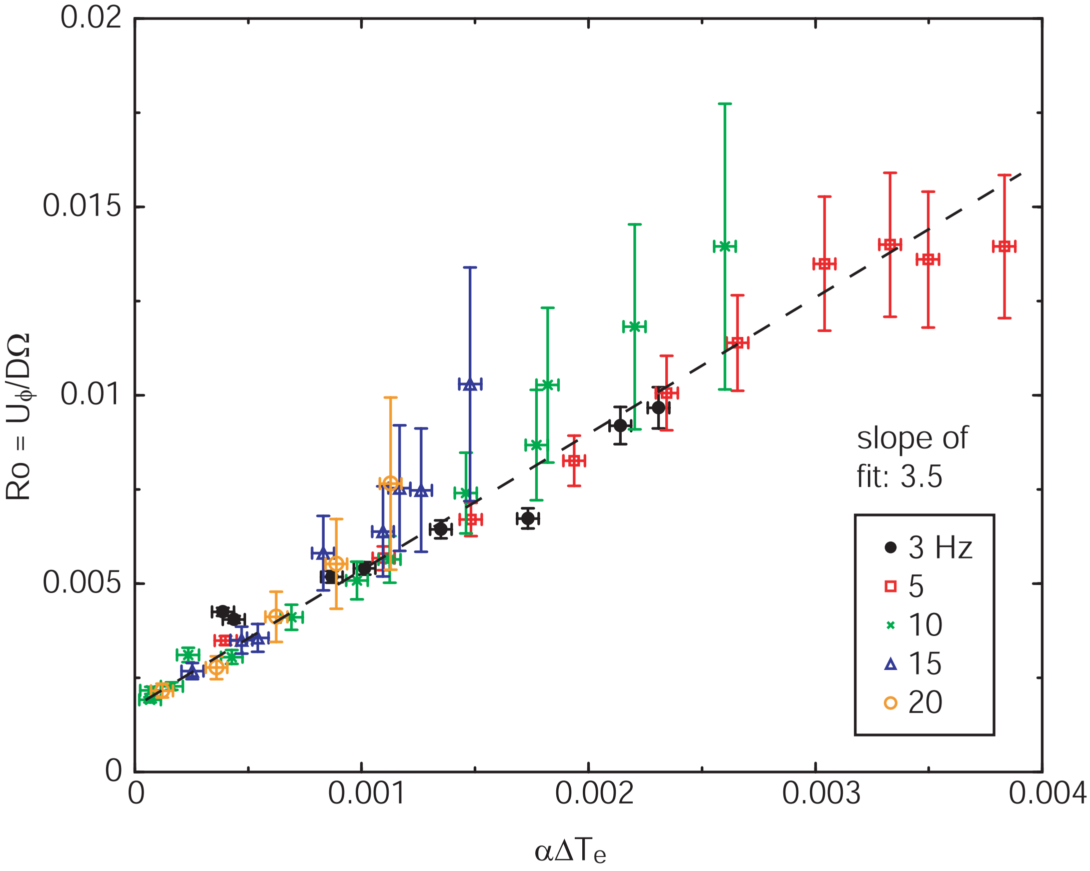

Figure 4.10: Rossby number is plotted against the dimensionless temperature drop $\alpha\Delta T_e$, where $\Delta T_e \equiv \Delta T - \Delta T_c - \Delta T_{adiabatic}$. The collapse and linear fit imply that $U_\phi \sim \Omega D \alpha \Delta T_e$.

One may then solve for velocity to obtain a scaling that is consistent with that used in fig. 4.10,

$$\frac{U}{\Omega D} \sim \alpha \Delta T. \tag{4.9}$$

This simple dimensional argument, is reminiscent of a more complex theory developed by Aubert et al. mentioned in chapter 1. They use the vertically-averaged vorticity equation, assuming that Coriolis, buoyancy, and inertial effects are in balance to derive scaling laws for radial velocity, typical vortex size, and temperature fluctuations. They also derive a scaling for zonal velocities given by

$$u_\phi \sim \left(\frac{Ra_Q}{Pr^2}\right)^{4/5} E^{9/10}, \tag{4.10}$$

Ignoring the Nusselt number dependence (as did Aubert et al. when applying their scalings to data from gallium convection), this may be put in terms of ΔT and Ω,

$$u_\phi \sim (\alpha \Delta T)^{0.8} \Omega^{0.7}. \tag{4.11}$$

Our data is plotted with this scaling in the subsection below.

Another mechanism which may be responsible for the zonal flows we observe is thermal winds. Thermal winds are driven by the misalignment of the centrifugal acceleration with the temperature gradient. For example, if one began to rotate a sphere of fluid with a spherical gradient in temperature, say hot at the center and cold at the surface, the heavier cold fluid near the poles would begin to move toward the equator. This initial motion would be deflected by Coriolis forces into a zonal flow. The equation governing a thermal wind in the presence of centrifugal acceleration is

$$(2\mathbf{\Omega} \cdot \nabla)\mathbf{v} = \alpha \nabla T \times \Omega^2 \mathbf{r_c}, \tag{4.12}$$

where r_c indicates cylindrical radius. If we assume a spherical, conductive radial temperature profile, the temperature gradient is $\Delta T D/r_s^2$, where r_s is spherical radius. Then, with the rotation axis aligned with the z axis, we have

$$2\Omega \frac{\partial v_\phi}{\partial z} = \alpha \frac{\Delta T D}{r_s^2} \Omega^2 r_c sin\theta, \tag{4.13}$$

where θ is the angle between a cylindrically radial and spherically radial directions. One can approximate an integral of this equation along a line of constant cylindrical radius from the bottom of the vessel up to the equator of the inner sphere as

$$v_\phi \approx \Omega D \alpha \Delta T, \tag{4.14}$$

the same scaling as derived above. Although it is not clear from our measurements, one could imagine ways to determine whether thermal winds or small scale convective motions are driving the zonal flows. Ultrasound or other velocimetry instrumentation could be used to measure the z-gradient of velocity. If the gradient matches eq. 4.13, thermal winds would be confirmed. Another technique which may shed some light, is to reverse the temperature gradient. Thermal winds should be present in this case as well. If they are of comparable magnitude, this would also confirm the thermal wind hypothesis.

Manneville and Olson took measurements of zonal flows in a very similar experimental device using water for the convecting fluid [43]. They found complicated banded structure in the zonal flow which depended upon latitude and Rayleigh number. They also observed a turn-over in the increase of fluid velocity as Rayleigh number was increased. The high ΔT data in our results may indicate similar behavior, but higher Rayleigh numbers would be required to fully explore this hypothesis in our experiments.

One should be cautious applying the above arguments to the Earth's core. For both the dimensional argument and for thermal winds, one factor of Ω comes from the buoyancy force. For the Earth, the buoyancy force is largely independent of rotation rate. Therefore, the scalings determined above must be put into a form using dimensionless numbers in order to compare to Earth.

$$U_\phi = 3.5 \frac{\kappa}{D} Ra E. \tag{4.15}$$

4.5.1 *Comparison to gallium experiments by Aubert et al.*

As mentioned in the introductory chapter, Aubert et al. have conducted convection experiments with liquid gallium in a rotating sphere [2]. They measured fluid velocities and developed scaling

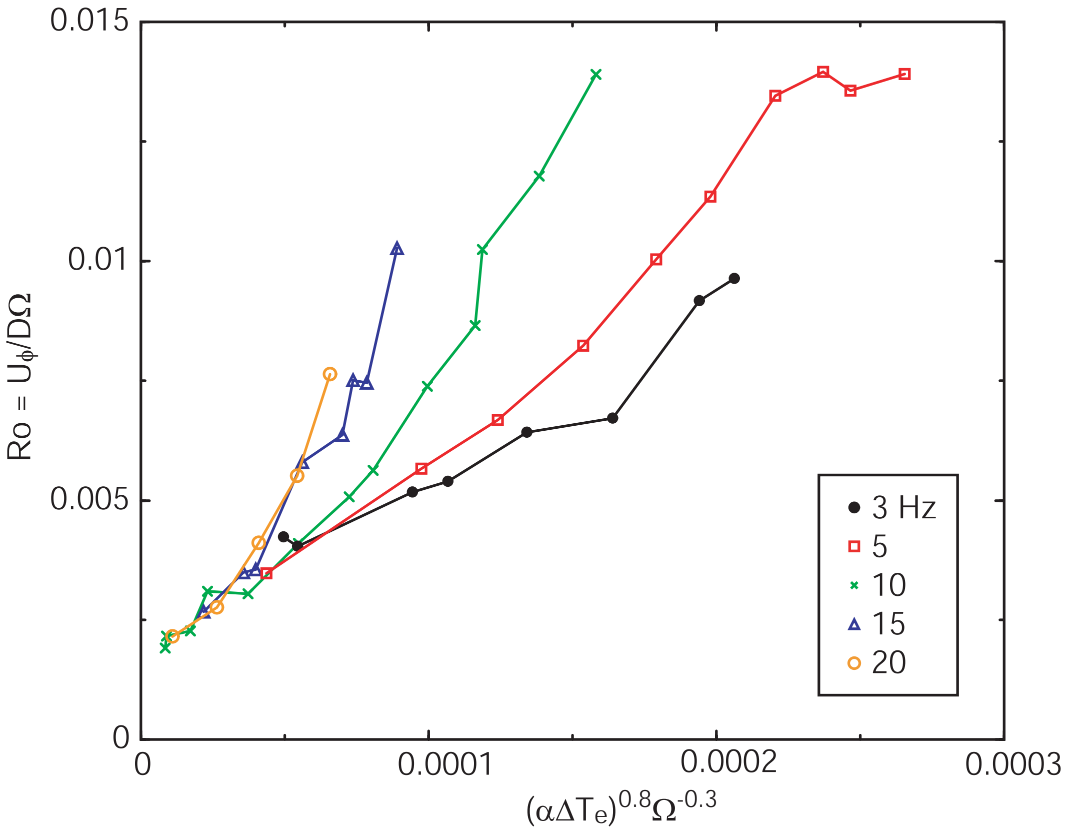

Figure 4.11: The zonal velocity scaling of Aubert et al. tested with our data shows a good fit for low ΔT, but fits less well for higher ΔT.

laws to explain their measurements. In this section I will compare the zonal velocities that we observed with the Aubert et al. scalings.

In fig. 4.11 our measurements of zonal velocity are plotted in the same way that Aubert et al. have presented their results in reference [2]. In other words, the Nusselt number is considered constant. If the Nusselt component of the Aubert scaling is retained, the prediction is

$$u_\phi \sim \left(\frac{RaNu}{Pr^2}\right)^{4/5} E^{9/10}. \qquad (4.16)$$

This scaling is tested in fig. 4.12. The data clearly do not fit this model. A reason may be that Aubert et al assumed $Nu - 1 \sim Nu$ in the derivation of their scaling laws.

There are clearly apparent discrepancies between our results and those of Aubert et al. Although similar, the apparatus and methods used by Aubert et al. were not identical to our own.

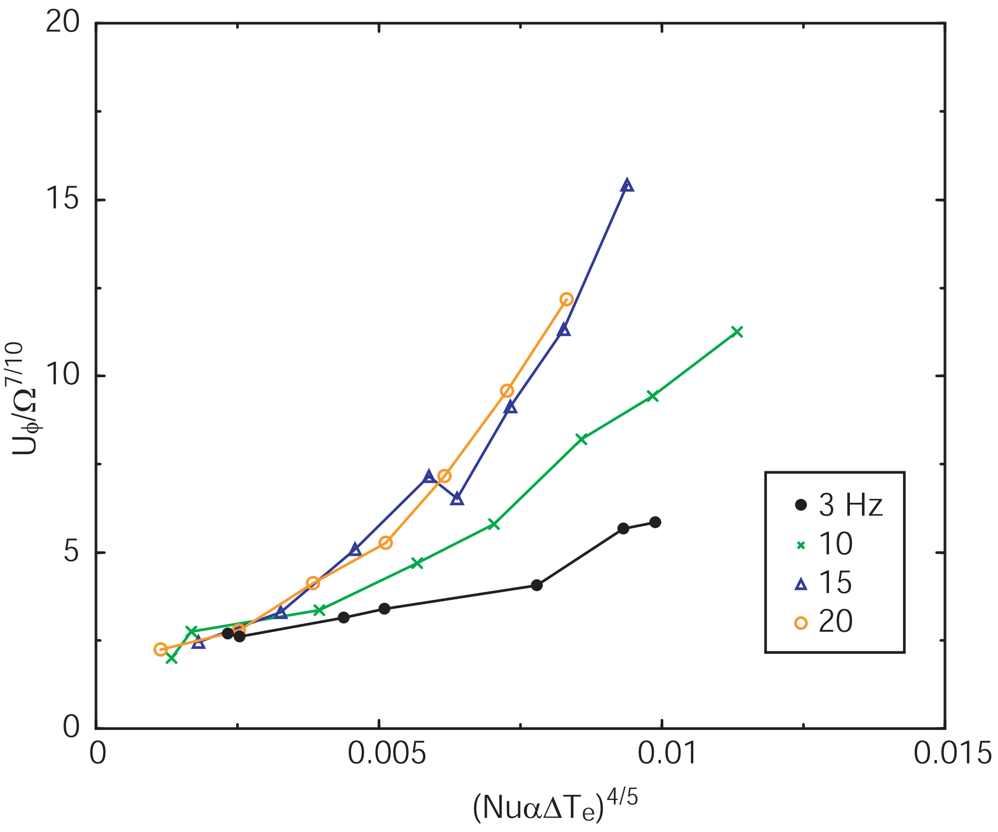

Figure 4.12: The zonal velocity scaling of Aubert et al. including Nusselt number dependence is tested with our data. The fit is poor.

Instead of an inner sphere, in their apparatus, cooling fluid passed through a cylindrical shaft extending from the top to the bottom of the outer spherical shell. One likely consequence of this different type of “inner core” is that the boundary layers at the tangent cylinder are different. In our experiment, geostrophy will cause a free-shear boundary along the tangent cylinder above and below the sphere. In Aubert’s, the “tangent cylinder” is the solid surface of the cooling channel, resulting in a shear (rather than a free-shear) boundary. Another difference between the setups is the nature of the coolant flow. Cooling fluid in our apparatus passed through the bottom shaft, through the inner sphere, and then returned also through the bottom shaft. Thus, the shaft above the sphere was not significantly cooler than the sodium, minimizing unwanted convection due to the shafts. In Aubert’s device, the cooling was pumped in at the north pole and out at the south pole. An additional difference is in the method of varying “inner core” temperature. In our setup, the coolant flowed at a constant and high flow rate (around 20 l/minute) and the temperature of the fluid is modulated. In the Aubert experiment, the flow rate was modulated in order to change the inner cylinder temperature. In our experience, this method less reliably produces a constant temperature inner boundary, because at low flow rates, the incoming fluid is much cooler than the outgoing fluid. A perhaps less important difference is that the radius ratio between the inner cylinder and their outer sphere was 0.36, a 10% difference compared to our inner to outer sphere radius ratio of 1/3. Finally, the Prandtl number of gallium (Pr=0.025) is different than that of sodium (Pr=0.01). We cannot accurately assay which of these differences might be responsible for the velocity scaling discrepancy.

4.6 **Heat transfer**

For two otherwise identical systems with low and high Prandtl numbers, the Nusselt number will always be larger for the high Pr system. In other words, heat transfer in low Prandtl number fluids is different from that in high Pr fluids in that more heat is transferred by conduction. In spite of this lower convective heat flux, the flow is often quite turbulent even very close to onset. In two different gallium convection experiments (also low Pr), Aubert, et al. [2]and Aurnou et al. [4], also observed turbulence very close to onset. We observe this character of convection in our experiments as well. In our experiments as well as the above mentioned low Pr experiments, the Nusselt number is never greater than 2. This contrasts sharply with high Pr experiments (water: Pr = 7, silicon oil Pr = 14) which often exhibit very high Nusselt numbers. For example, Sumita and Olson have obtained Nusselt numbers as high as 186 using silicon oil [62].

The total heat transfer was measured at a latitude of 45° using two temperature probes embedded at different depths in the outer wall of the vessel. The data for multiple rotation rates and ΔTs are shown in fig. 4.13. It is certain that there are variations in heat flux at different latitudes. Measurements have not yet been made to quantify this. Some evidence for latitude dependent heat transfer is discussed in the upcoming section on measurements with applied magnetic field.

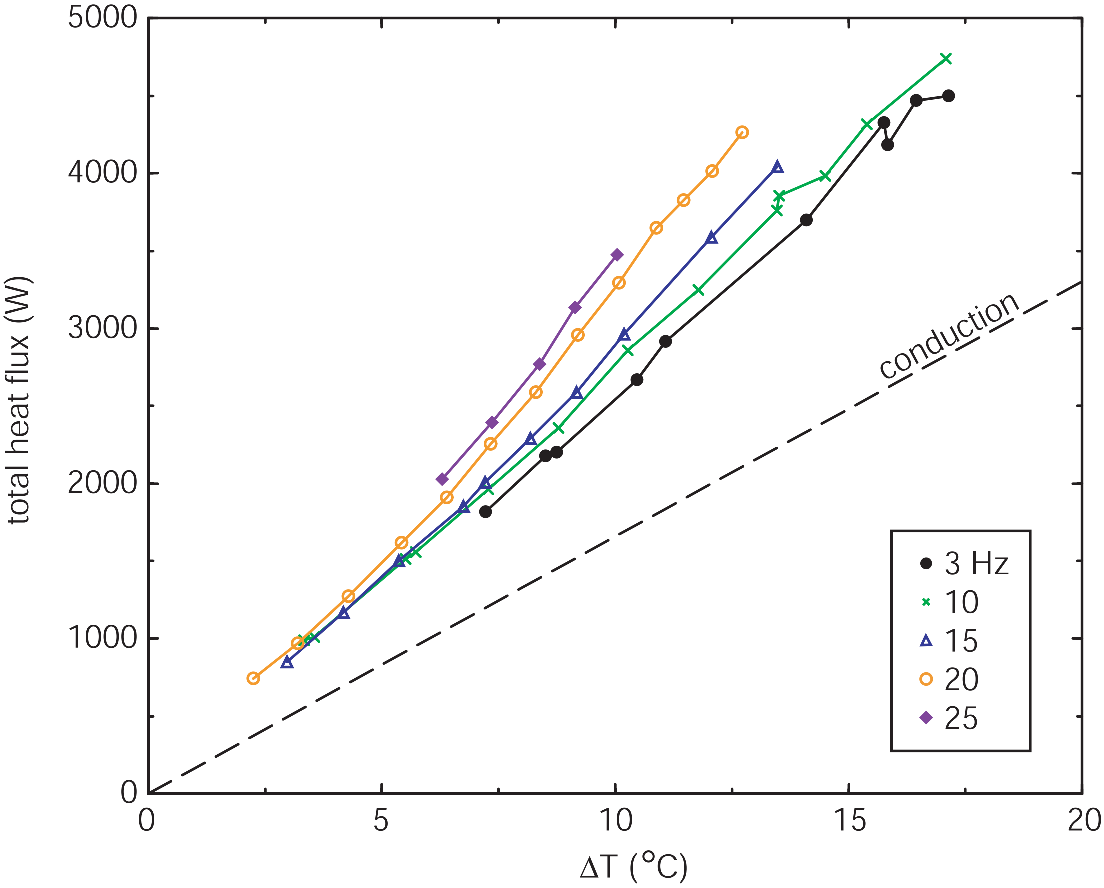

Figure 4.13: The total heat flux is plotted for different rotation rates and a range of temperature drops. The dotted line represents the heat that would be conducted if the sodium were stationary.

4.6.1 *Conduction*

The conductive heat flux for a given temperature drop may be estimated with a simple calculation. Assuming the system is in steady state and the fluid is stationary and of constant thermal conductivity, the temperature equation is simply Laplace's equation,

$$\nabla^2 T = 0. \tag{4.17}$$

The solution to Laplace's equation in a spherical geometry is

$$T(r) = A + \frac{B}{r}, \tag{4.18}$$

which is subjected to the boundary conditions $T(R_o) = T_o$ and $T(R_i) = T_i$. These boundary conditions imply that

$$T(r) = T_o + \frac{\Delta T R_i}{R_o - R_i}(1 - \frac{R_o}{r}). \tag{4.19}$$

Since $R_o = 3R_i$ this may be further reduced to give the conductive temperature profile,

$$T(r) = T_o + \frac{\Delta T}{2}(1 - \frac{R_o}{r}). \tag{4.20}$$

The conductive heat flux per unit area is then

$$\Phi = k\frac{\partial T}{\partial r}, \tag{4.21}$$

$$\Phi = k\frac{\Delta T}{2}\frac{R_o}{r^2}. \tag{4.22}$$

Then the total heat flux is

$$\begin{aligned} \Phi_{tot} &= 4\pi R_o^2 k\frac{\Delta T}{2}\frac{R_o}{R_o^2}, && (4.23) \\ \Phi_{tot} &= 2\pi k \Delta T R_o. && (4.24) \end{aligned}$$

The dashed line in fig. 4.13 represents this total conducted heat flux.

As discussed in the first section of this chapter, temperature measurements at midgap were used to approximate the radial temperature profile. The ratio

$$\frac{T(r_{midgap}) - T_i}{\Delta T} \tag{4.25}$$

is plotted in fig. 4.1. The conduction profile computed above predicts a value for this ratio given by

$$\frac{T(r_{midgap}) - T_i}{\Delta T} = \frac{T(2R_i) - T_i}{\Delta T} = 0.75. \tag{4.26}$$

This value is the dashed line in fig. 4.1. The temperature at the midgap probe never deviates more than 20% from the conductive profile.

4.6.2 *Convection*

As shown in fig. 4.13, the total heat flux is never more than twice the conductive heat flux. That is, the Nusselt number is never greater than 2 for any of our experiments. The difference between the total and the conducted heat flux is shown in fig. 4.14.

One may derive a relationship between the convective heat flux and the the control parameters using an argument based on viscous dissipation. The basic idea is to relate global dissipation to an estimate of local dissipation in order to estimate Nu(Ra, E, Pr). This argument was inspired by a theory primarily developed by Grossman and Lohse for Rayleigh-Beénard convection (e.g. [29], [56]).

Taking a volume average of the kinetic energy equation one may obtain the exact relation for the global viscous dissipation,

$$\epsilon_{global} = \frac{\nu^3}{D^4}(Nu - 1)RaPr^{-2}. \tag{4.27}$$

The derivation of this relation is carried out in detail in appendix A. Consider now the dissipation associated with convective velocity structures of spatial size $\delta \sim E^{1/3}D$ and typical velocity U,

$$\begin{aligned} \epsilon_{local} &\equiv \nu(\nabla \mathbf{v})^2 && (4.28) \\ &\sim \nu \frac{U^2}{\delta^2}\frac{\delta}{D} && (4.29) \\ &\sim \frac{\nu^3}{D^4}\frac{Re^2}{E^{1/3}}, && (4.30) \end{aligned}$$

Where the factor of δ/D is introduced to account for the fact that the region in which the dissipation occurs is some fraction of the whole volume. A similar means of estimating local dissipation was used with success by Grossman and Lohse [29]. Another way to interpret the local estimate is

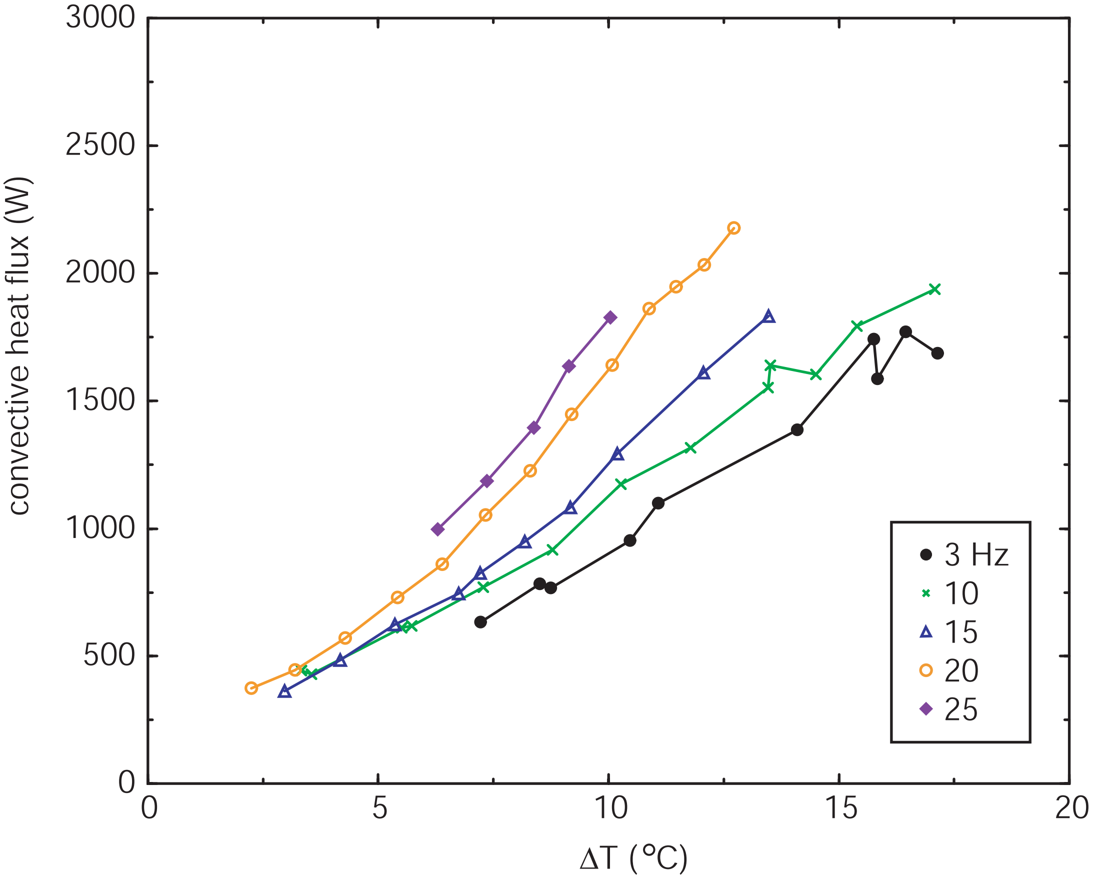

Figure 4.14: The convective heat flux is plotted for different rotation rates and a range of temperature drops.

that the dissipation is dominated by laminar viscous boundary layers of thickness $E^{1/3}D$. Aubert et al. have argued that dissipation should be dominant in boundary layers. Plaut and Busse [49] have observed in numerical simulations the presence of thermally modified Stewartson layers on the vertical boundaries of cylindrical centrifugal convection with thickness that scales like $E^{1/3}$. Whether the dissipation occurs in boundary layers or convective structures, we may equate the global and local dissipations to obtain

$$(Nu-1)RaPr^{-2} \sim Re^2E^{-1/3}. \tag{4.31}$$

We now assume that the typical velocities of the dissipative structures is $U \sim \Omega D\sqrt{\alpha \Delta T}$ and put the nondimensional numbers in terms of our control parameters Ω and ΔT, to obtain ,

$$(Nu-1)\Delta T \sim \Delta T \Omega^{1/3}. \tag{4.32}$$

The heat transfer due to convection is proportional to $(Nu-1)\Delta T$. Our measured convective heat flux is shown in fig. 4.15 plotted against $\Delta T \Omega^{1/3}$.

The scaling used for the convective velocity scale $U \sim \Omega D\sqrt{\alpha \Delta T}$ is known as the ballistic estimate. It may be derived from estimating the free fall velocity of a fluid parcel that is ΔT colder than its neighbors and subject to an acceleration $\Omega^2 D$ over a distance D. One may also arrive at this scaling from considering a balance of inertia and buoyancy forces in the Navier-Stokes equation,

$$\begin{aligned} (\mathbf{v}\cdot\nabla)\mathbf{v} &\sim \Omega^2\mathbf{r}\alpha\Delta T, && (4.33)\\ \frac{U^2}{D} &\sim \Omega^2 D\alpha\Delta T. && (4.34) \end{aligned}$$

One may solve for U to find the same scaling as the ballistic estimate. It is also of interest to note that the Aubert model discussed in the previous section predicts $v_{radial} \sim \sqrt{v_\phi E^{-1/2}}$. Although they observed a different scaling for v_ϕ, this relationship applied to our measurements of v_ϕ gives the radial velocity scaling $v_{radial} \sim \Omega^{0.75}\Delta T^{0.5}$, which is not extremely dissimilar from the ballistic estimate. Using their scaling law for u_ϕ, one obtains $v_{radial} \sim \Omega^{0.6}\Delta T^{0.4}$. It seems that their model systematically slightly under-predicts our estimates of velocities.

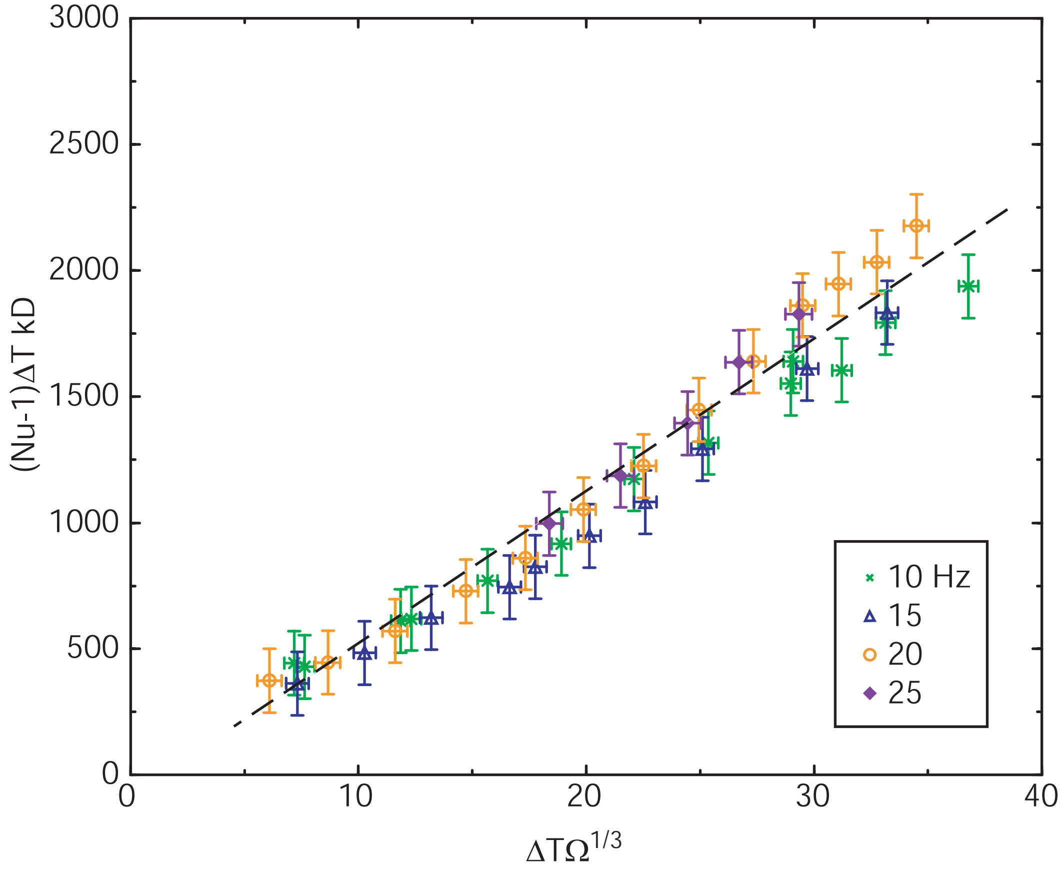

Figure 4.15: The convective heat flux is plotted against $\Delta T \Omega^{1/3}$.

4.7 Temperature power spectra

Both the heat flux and standard deviation scalings were explained with arguments using the predicted length scale for vortices at the onset of convection ($\delta \sim E^{1/3}D$). This begs the question; do we observe any periodicity as is also predicted close to onset? The time series in fig. 4.4 suggest that this is not the case. We may be certain by examining power spectra of the temperature fluctuations. Shown in fig. 4.16 are power spectra for two ΔTs at each of three different rotation rates. It is clear in the power spectra that the temperature signal is not periodic, showing broad band fluctuations with interesting structure down to the lowest rotation rates and ΔTs.

Several features are common to all temperature spectra that we measured. Most noticeable is the distinct drop in power law slope at high frequency. At frequencies above this knee the power law slopes of the spectra are constant and close to -5.7. Significantly, we find that the knee frequency at which the steep slope begins is

$$f_c = 2.0\Omega\sqrt{\alpha\Delta T}. \tag{4.35}$$

The power spectra shown in fig. 4.16 are plotted in fig. 4.17 scaled by their standard deviation and the knee frequency. Two-dimensional numerical simulations by Tran and Bowman suggest that the knee in the spectra marks the primary frequency at which energy is injected into the flow [64], [65]. In other words, the knee frequency is associated with convective motions. The fact that the knee frequency $f \propto \Omega\sqrt{\Delta t}$ suggests strengthens the arguments in the last section where we assumed $U_convective \sim \Omega\sqrt{\Delta T}$. The knee frequency is shown in fig. 4.18 for several rotation rates for increasing ΔT. We note that these data were extracted by hand for each of the power spectra. The frequency scaled by rotation rate is plotted in fig. 4.19. The dashed line in fig. 4.19 is proportional to square root of ΔT.

The slope of the high frequency part of the spectra is close to -17/3 as shown in fig. 4.17 and also in the compensated spectra in fig. 4.20. This slope may be explained using the temperature equation and some assumptions about the underlying velocity field. First, Taylor's hypothesis is assumed to hold since we have observed substantial azimuthal velocities for most values of our

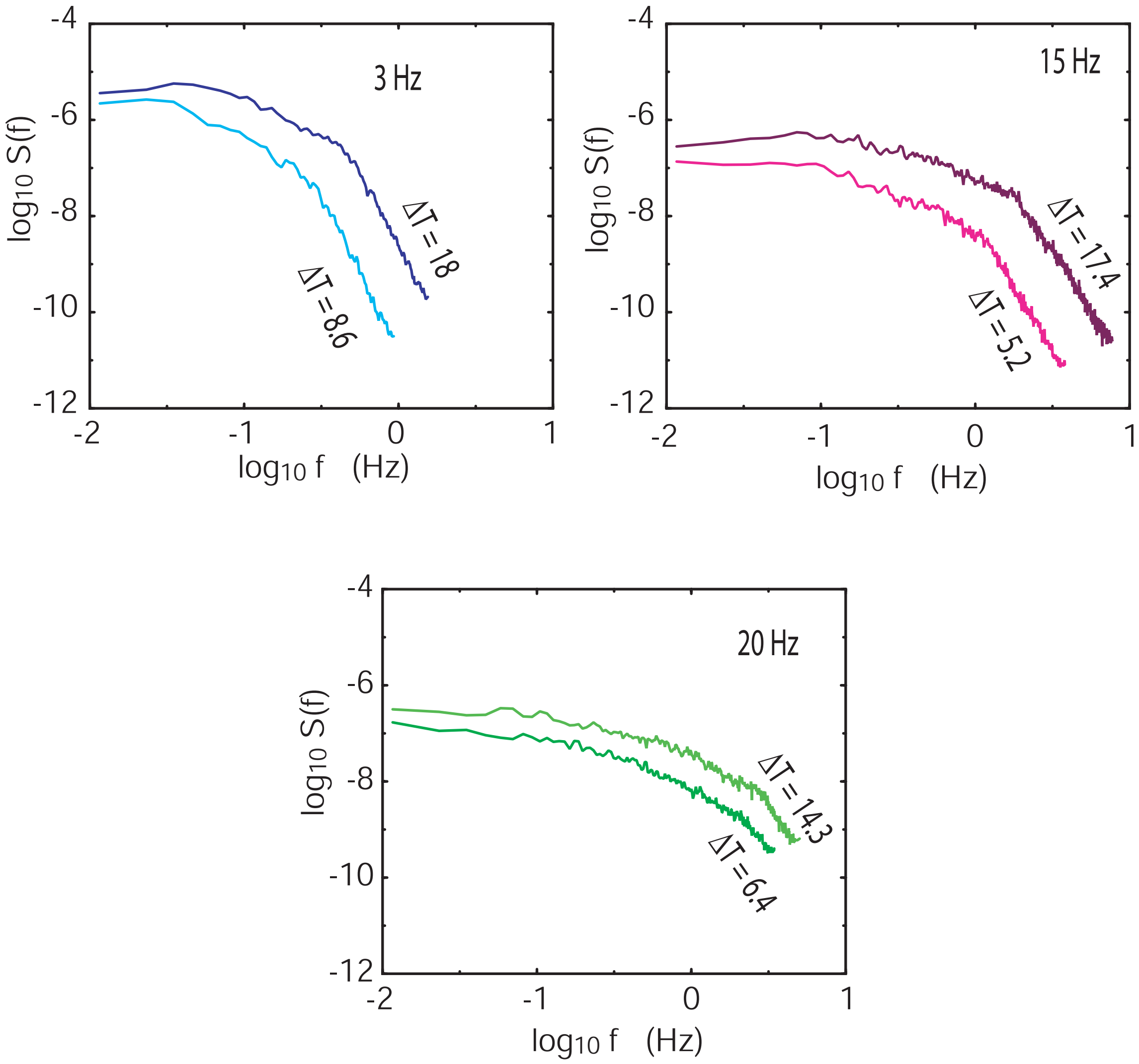

Figure 4.16: Temperature power spectra are shown for two ΔT at three rotation rates. All spectra show a distinct knee into a diffusive regime with a steep contant slope above this knee.

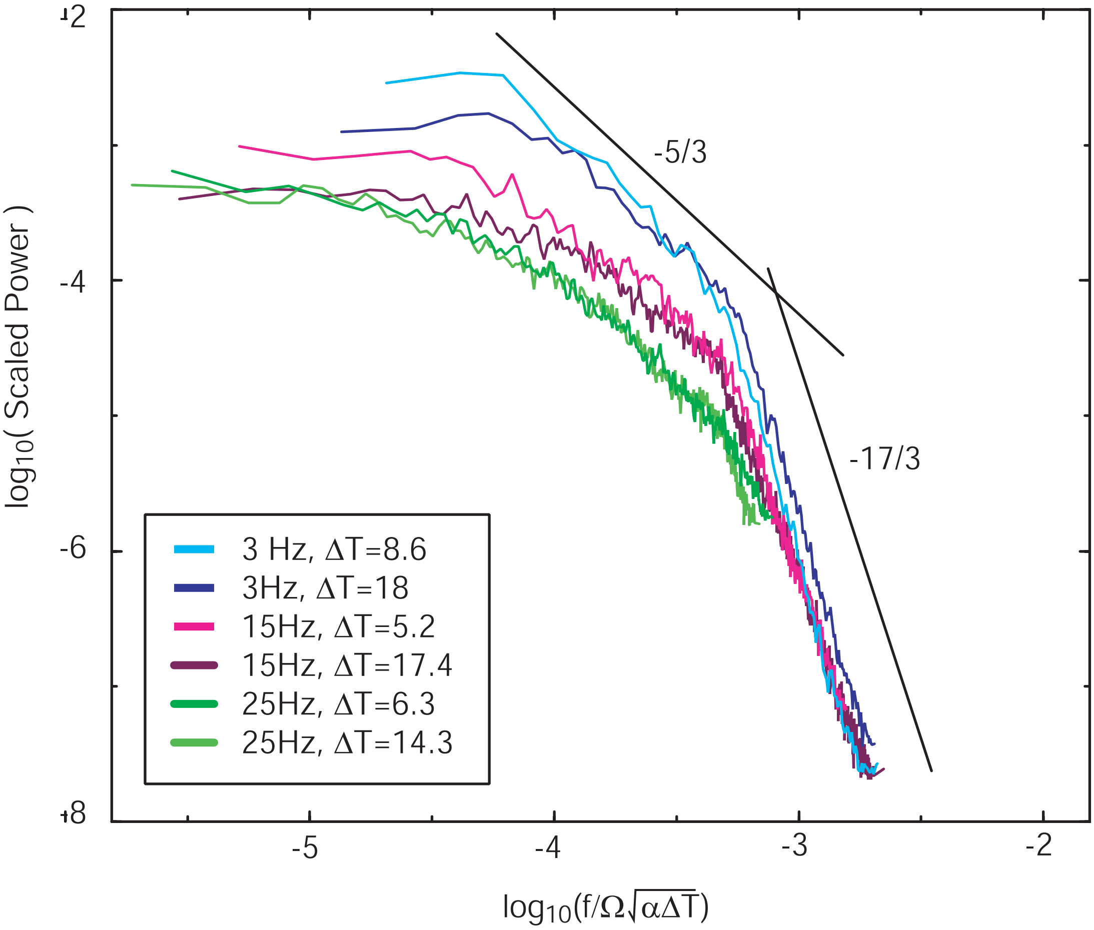

Figure 4.17: Temperature power spectra are shown scaled by their standard deviation and the knee frequency $\Omega\sqrt{\alpha\Delta T}$. There is apparently some amplitude dependence beyond that captured by the standard deviation.

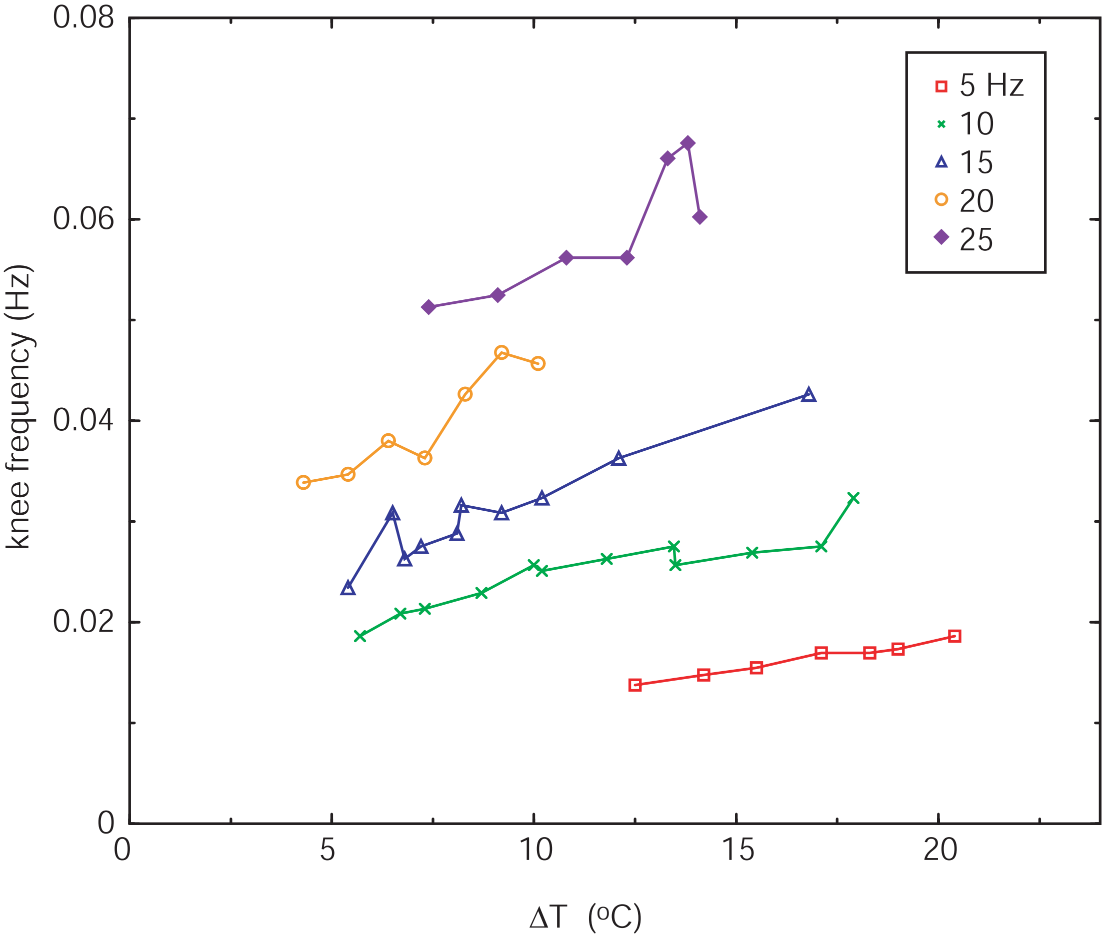

Figure 4.18: The knee frequency for many power spectra is shown as a function of rotation rate and ΔT. These data were extracted by hand from the power spectra.

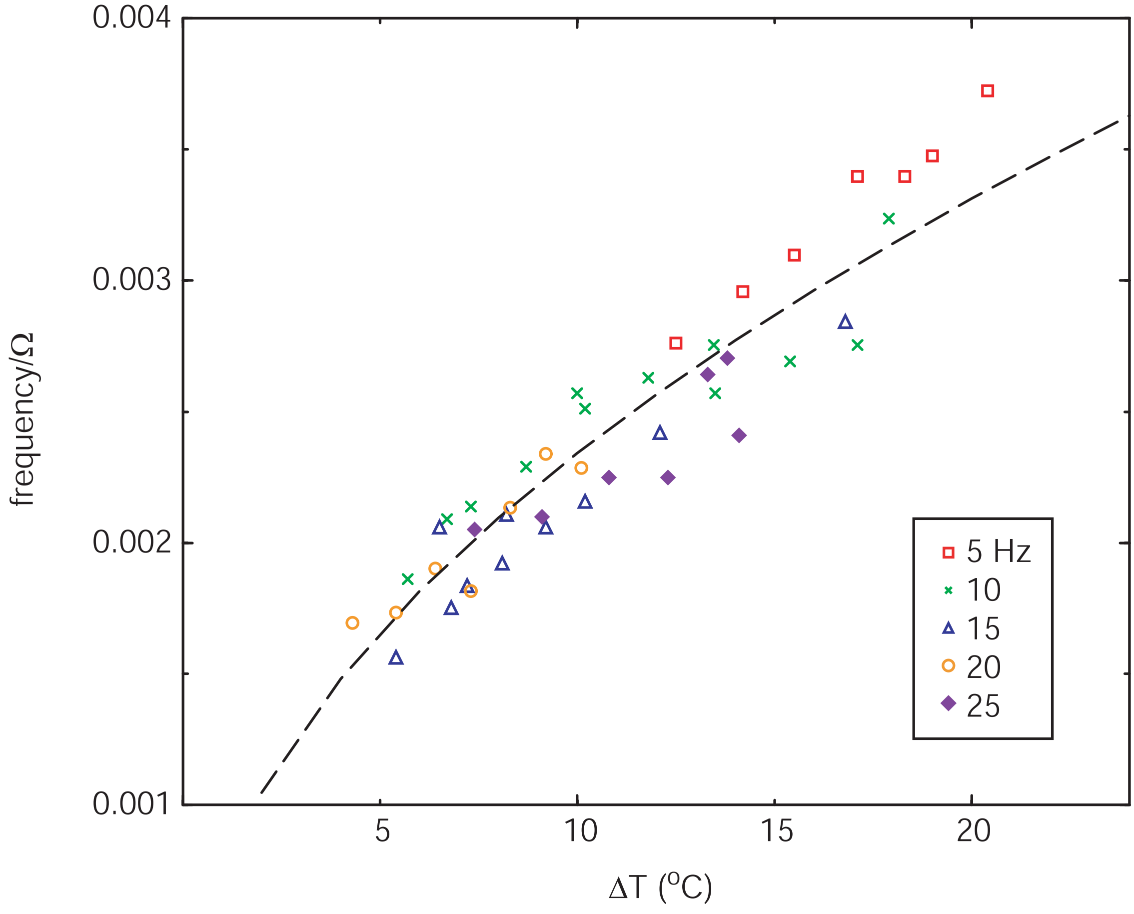

Figure 4.19: The knee frequency is shown scaled by the rotation rate. The dashed line is proportional to $\sqrt{\Delta T}$.

control parameters. In other words, it is assumed that temperature fluctuations are caused by advection of spatial temperature structures past the measurement point. This is the same assumption used to explain the standard deviation above. A second assumption is that the underlying velocity field has an energy spectrum with an inertial range that scales as $E(k) \sim k^{-5/3}$. If there is also a balance between advection and diffusion of temperature then from the temperature equation, we have,

$$(\mathbf{v} \cdot \nabla)T \sim \nabla^2 T. \tag{4.36}$$

If the velocity, whose scale given by $v = \sqrt{kE(k)} \sim k^{-1/3}$, is advecting the large scale temperature gradient, while the temperature is diffusing on length scales $1/k$, then we have

$$k^{-1/3}\frac{\Delta T}{D} \sim k^2 \Delta T', \tag{4.37}$$

where T' is the size of temperature fluctuations on a scale $1/k$. Then we solve for T' and use it to find the temperature variance spectral density $C(k)$,

$$\begin{aligned} C(k) &= (T')^2/k & (4.38)\\ C(k) &\sim \left(k^{-7/3}\frac{\Delta T}{D}\right)^2 \frac{1}{k} & (4.39)\\ C(k) &\propto k^{-17/3} & (4.40) \end{aligned}$$

Camussi and Verzicco [13] have observed high wavenumber slopes close to -17/3 in temperature spectra obtained in direct numerical simulations of Rayleigh-Bénard convection with mercury (low Pr). Similar to our results, they observed Kolmogorov-like turbulence in the velocity field and used this fact to collapse different spectra to one curve. They did not attempt to explain the -17/3 slope.

4.7.1 *Further speculations about power spectra*

At larger time scales than the diffusive regime discussed above, the power law slopes of the spectra range in value between -5/3 and 0. The -5/3 slope is observed mostly at low rotation rates and high ΔT. Compensated spectra with power divided by $f^{-5/3}$ are shown in fig. comp17. Sreenivassan [58] has reported that in shear flows the spectral slope of passive scalars approaches -5/3 as one

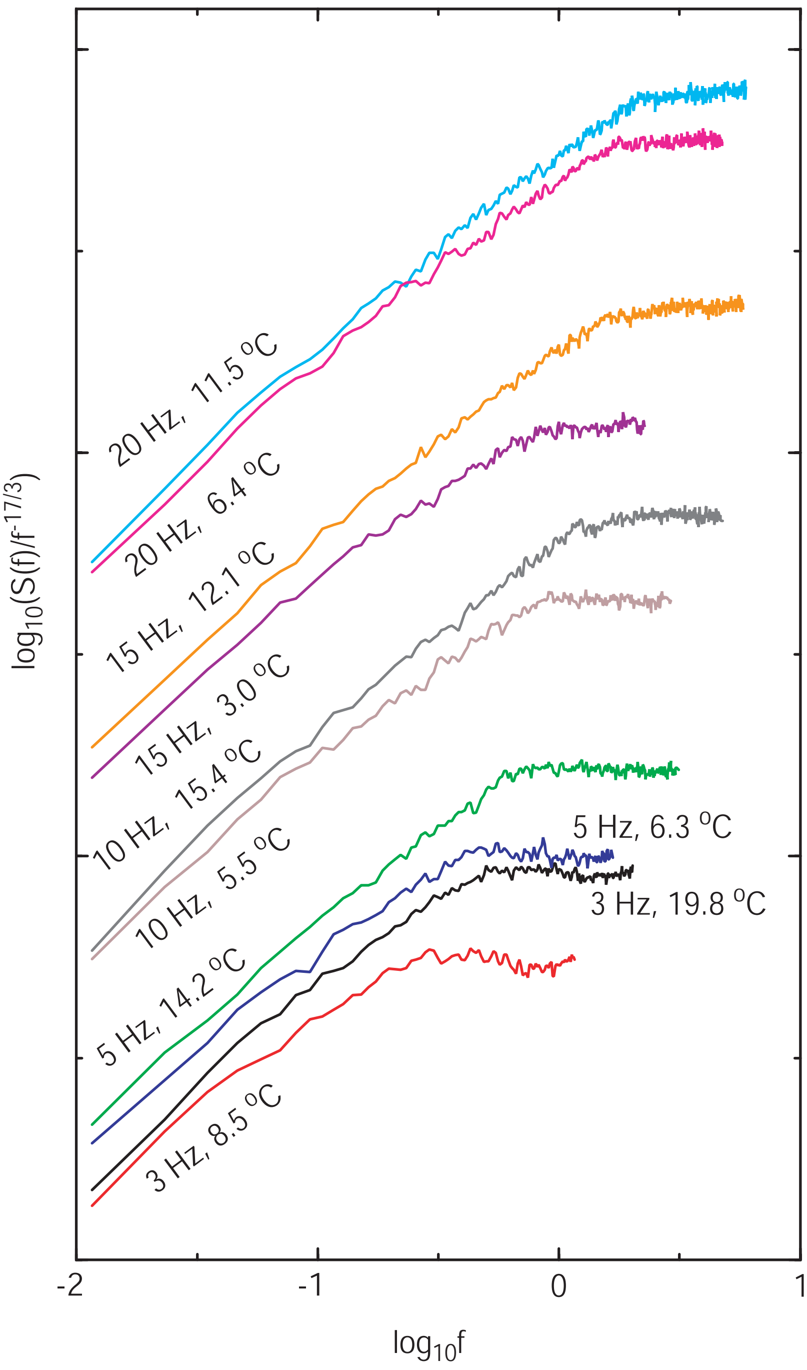

Figure 4.20: Compensated spectra are shown with the power divided by $f^{-17/3}$ for a range of rotation rates and ΔT. The curves have been shifted vertically for clarity.

increases the Reynolds number, but is shallower for lower Reynolds number. Ignoring effects due to Coriolis forces, this trend is opposite our observations. As we increase rotation rate, buoyancy forces are greater and our Reynolds number based on measured zonal flow increases, but the slope of the scalar spectrum becomes shallower. Measurements of temperature spectra from the atmosphere [45] show a large -5/3 regime. This result is intriguing because the atmosphere is in a similar force balance regime to our experiment.

Using a simple dimensional argument one may also derive a -5/3 scaling for the spectral slope of a passive scalar in a turbulent velocity field. If one assumes that the spectral density $C(k)$ of the variance of a passive scalar θ depends only on the rate of dissipation of variance χ, a time scale τ_θ and wavenumber k, then there is only one possible relationship which is dimensionally correct,

$$C(k) \sim \chi \tau_\theta k^{-1}. \tag{4.41}$$

Given an underlying velocity field, which has an energy spectrum given by $E(k) \sim k^{\beta}$ then the time scale τ_v of the velocity field $v(k)$ at a length scale $1/k$ is

$$\tau_v \sim \frac{1}{kv(k)}. \tag{4.42}$$

And since $v(k) = \sqrt{kE(k)}$ we have

$$\tau_v \sim \frac{1}{k\sqrt{k^{1-\beta}}}, \tag{4.43}$$

$$\tau_v \sim k^{-3/2+\beta/2}. \tag{4.44}$$

If we further assume that the time scale of the scalar is equal to that of the velocity, $\tau_\theta = \tau_v$, then

$$C(k) \sim \chi k^{-5/2+\beta/2}. \tag{4.45}$$

If $\beta = 5/3$ then the scaling for scalar spectrum is $C(k) \sim \chi k^{-5/3}$ as well.

In addition to an explanation for the -5/3 part of the observed spectra, the above argument may explain the shallower slopes as well. At larger length scales it is likely that the flow resembles the two-dimensional, geostrophic picture prescribed by the Taylor-Proudman theorem. Two-dimensional turbulence is often associated with an cascade of enstrophy from large to small

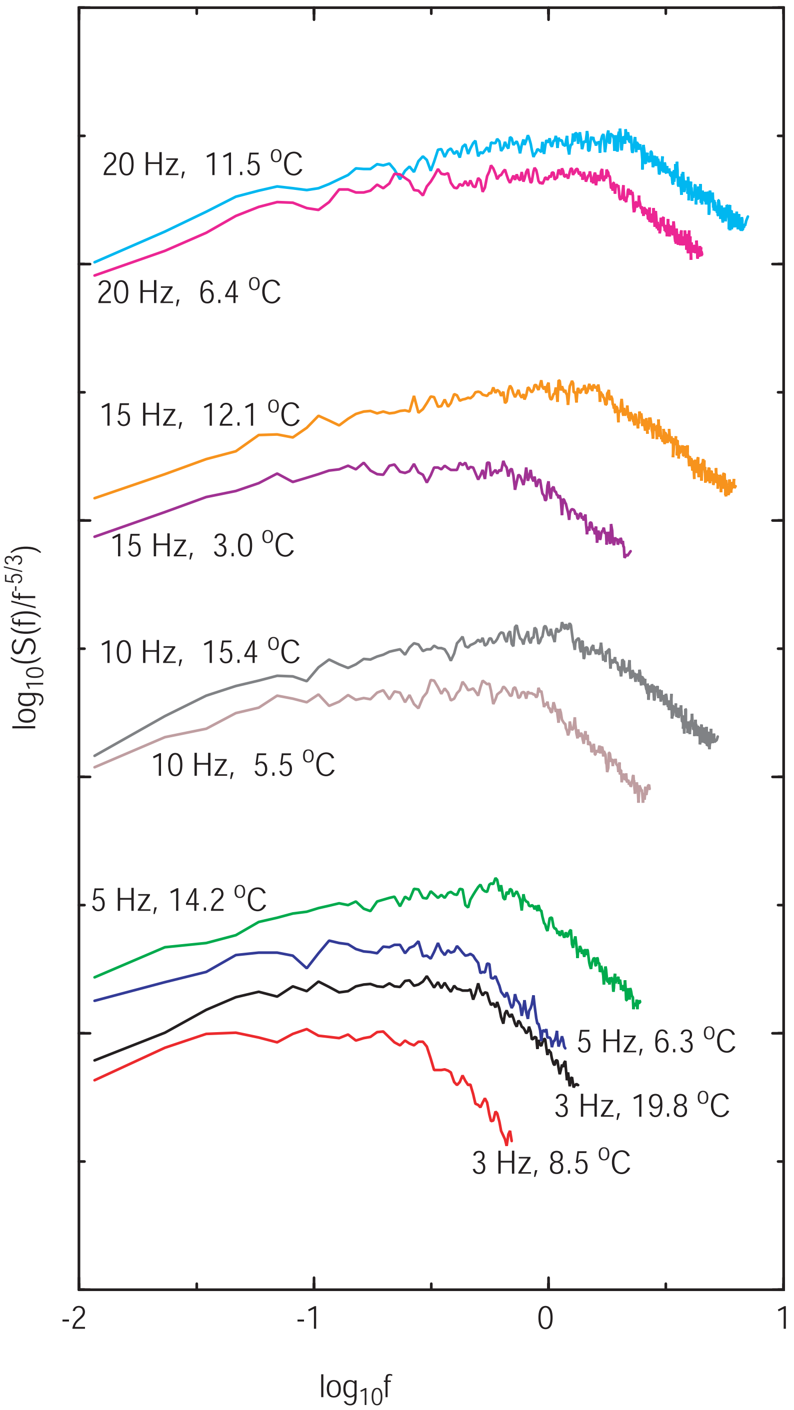

Figure 4.21: Compensated spectra are shown with the power divided by $f^{-5/3}$ for a range of rotation rates and ΔT. The curves have been shifted vertically for clarity.

scales, which is accompanied by a -3 slope in the energy spectrum [37], [6]. With $\beta = 3$ in the above argument, one obtains $C(k) \sim \chi k^{-1}$, which is similar to some of the shallower slopes we have observed. For example, fig. 4.22 shows compensated power spectra for a range of rotation rates and ΔT with the power divided by f^{-1}. The -3 and -5/3 slopes have also been observed in quasigeostrophic numerical simulations by Tung and Orlando [67].

Perhaps one should be cautious applying the above arguments to low Prandtl number fluids. It might be expected in such fluids that time scales in the temperature field would not be the same as the velocity since diffusion effects would play a role. However, our observations to a large extent indicate that the underlying velocity field does dictate time scales. Both in the scaling arguments for the standard deviations of temperature and the -17/3 slope of the diffusive part of the spectrum, the idea of velocity advecting temperatures was used with success.

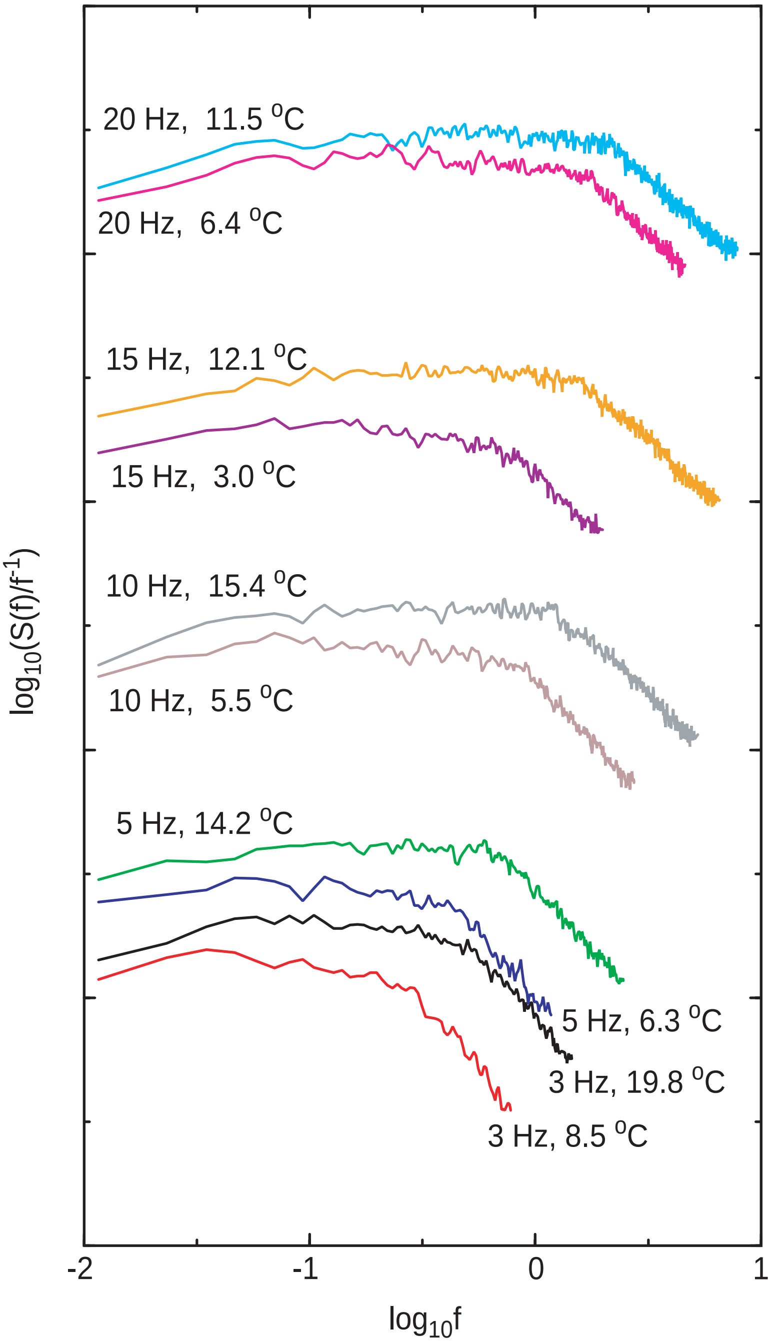

Figure 4.22: Compensated spectra are shown with the power divided by f^{-1} for a range of rotation rates and ΔT. The curves have been shifted vertically for clarity.

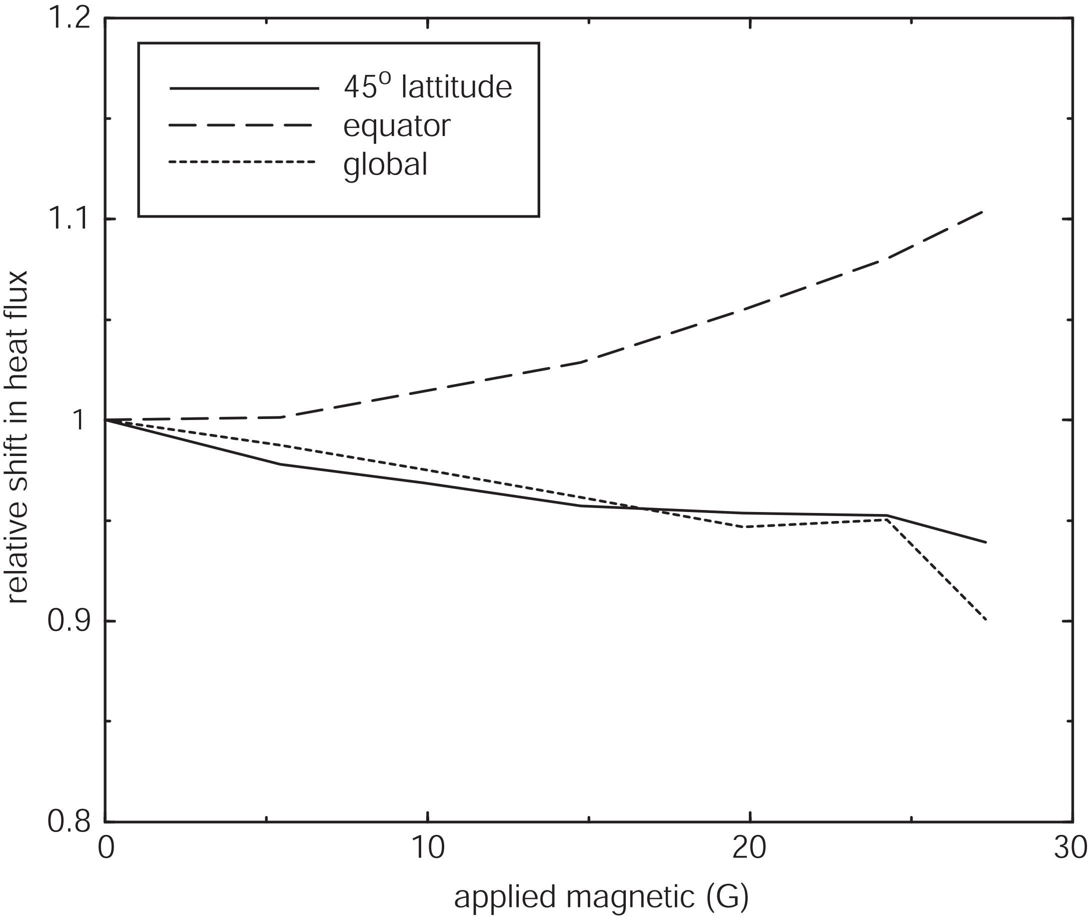

Figure 4.23: The relative shift in the total heat flux (dotted line), equatorial heat flux (dashed line), and 45° lattitude heat flux (solid line) are shown for increasing applied magnetic field. The data is taken at a rotation rate of 10 Hz and ΔT of 6.9 °C.

4.8 Magnetic field effects

Only a few experiments were conducted with applied magnetic fields. A pair of electric coils in a Helmholtz configuration, coaxial with the rotation axis, produced fields up to 30 Gauss (3 mT). The resulting change in dynamics manifested in altered heat flux. The total heat flux required to maintain a given ΔT was observed to drop with increased magnetic field. Furthermore, changes in spatial distribution of heat transfer changed. Heat flux increased near the equator and decreased at a polar angle of 45°. These results are summarized in fig. 4.23 where relative shifts are shown for total heat flux, equatorial heat flux, and 45° lattitude heat flux.

Magnetic fields have a similar effect as rotation on fluid flow when the fluid is electrically conducting. The magnetic field suppresses gradients in the velocity field which are in the same direction as the magnetic field; the flow tends toward 2-D. The observed behavior of changes in heat flux with applied magnetic field are consistent with this idea. If fluid motion is confined to planes perpendicular to the rotation axis then heat flux will be concentrated near the equator. Furthermore, the sloping boundaries of the spherical vessel combined with the tendency towards 2-D flow amounts to an overall suppression of flow. This is consistent with the decrease in global heat flux. This result will be discussed in the next chapter in the context of a saturation mechanism for the geodynamo as well as a possible mechanism for inhomogeneous formation of Earth's inner core.

Chapter 5

CONCLUSIONS AND PREDICTIONS

The convection experiments described in this dissertation were designed to model the outer core of Earth. Liquid sodium was subjected to a thermal gradient between rapidly co-rotating concentric spheres with radius ratio 1:3. The resulting centrifugally driven convection was highly turbulent, despite the fact that convective heat transfer was never more than that of conduction. With external magnetic fields applied, convective heat transfer was found to increase near the equator, while the total heat transfer decreased.

The velocity field of the liquid sodium was characterized by two scales: a large scale zonal flow and a smaller scale turbulent convective flow. The zonal flow was measured near the equator of the inner sphere and for all parameter values was retrograde with respect to rotation. The magnitude of the velocity was found to be consistent with a balance between Coriolis and buoyancy forces,

$$U_\phi = 3.5 \Omega D \alpha \Delta T. \tag{5.1}$$

The zonal flow may also have been driven by thermal winds. The Reynolds number based on this zonal flow ranged from 10^3 to 10^4.

The smaller scale convective velocities act to weakly mix the temperature gradient, resulting in a radial temperature profile which deviates from the conductive profile likely by less than 20 percent. Broad band power spectra and nearly Gaussian probability density functions of resulting temperature fluctuations indicate that the convective velocities are turbulent. These temperature fluctuations are swept by the zonal flow past temperature probes, which are fixed in the rotating frame. Measurements of these fluctuations suggest that the typical length scale for the convective velocities scales as $E^{1/3}D$. This results in temperature signals with standard deviation,

$$\sigma_T = 4.0 E^{1/3} \Delta T. \tag{5.2}$$

Heat flux and the power spectra of temperature fluctuations suggest a model of the small scale convective velocity determined by a balance between inertia and buoyancy forces,

$$U_{conv} \sim \Omega D\sqrt{\alpha\Delta T}. \tag{5.3}$$

This is the ballistic estimate for convective velocities.

Heat flux was found to increase with increasing rotation rate. At the highest rotation rates ($E = 5.5 \times 10^{-8}$) and largest temperature drops from the inner to outer sphere ($Ra = 2.0 \times 10^{9}$), the Rayleigh number was about 14 times critical. At this most extreme state of convection, the Nusselt number remained less than 2. Assuming that convective velocities are ballistic and length scales are $E^{1/3}D$, an argument based on dissipation was used to derive the following scaling,

$$(Nu - 1)\Delta T = 0.1E^{-1/3}\Delta T. \tag{5.4}$$

The convective heat transfer is proportional to $(Nu - 1)\Delta T$.

Power spectra of the temperature fluctuations exhibited a well-defined cross-over from inertial to diffusive time scales. The knee frequency for all parameter values was found to be

$$f_c = 2.0\Omega\sqrt{\alpha\Delta T}. \tag{5.5}$$

At frequencies smaller than this cross-over, power law slopes of spectra range between 0 and -5/3. Above the cross-over, in the diffusive regime, a constant slope of approximately -17/3 is observed. Summing up,

$$logS(f) = \begin{cases} s_0 \text{ to } s_1 - \frac{5}{3}log(f), & for \quad 0 < f \leq 2.0\Omega\sqrt{\alpha\Delta T} \\ s_2 - \frac{17}{3}log(f), & for \quad 2.0\Omega\sqrt{\alpha\Delta T} < f \leq \text{noisefloor} \end{cases} \tag{5.6}$$

where s_0, s_1, and s_2 are constant offsets. Both the -17/3 and -5/3 may be explained assuming that temperature fluctuations are due to a underlying velocity field with Kolmogorov-type energy spectra ($E(k) \sim k^{-5/3}$). The knee frequency is strong evidence that the dynamics at small scales is influenced by ballistic convective velocities.

5.1 Predictions for Earth's outer core

The experiments described here are like Earth's outer core in several ways. Both have turbulent velocity fields. This is revealed by the temperature fluctuations of the experiment and the broadband secular variation of Earth's magnetic field. Both the experiment and Earth's core have modest Nusselt number. Convective heat transfer in the experiment was never larger than the conductive heat transfer. In Earth's core, the heat conducted down the adiabat is thought to be responsible for most of the heat flux out of the core. Both systems have large scale retrograde zonal flows, although different in magnitude. The Rossby number based on zonal flow measurements for the experiment was between 10^{-2} and 10^{-3}, while the Earth's Rossby number based on the westward drift of the secular variation is of order 10^{-6}. (It is perhaps interesting to note that the Rossby number based on zonal flows on Jupiter are of order 10^{-2}.) The most important difference between the experiment and the Earth is likely the presence of a large magnetic field in Earth's core, the geodynamo. The Elsasser number for Earth's core is estimated near unity. During the few experiments with applied magnetic fields, our Elsasser number was only as large as 10^{-4}. For the sake of better understanding, let us set aside the differences between between the core and the experiment and explore the implications of our results for the Earth.

5.1.1 *Zonal flow and core Rayleigh numbers*

Let us first consider the zonal flow. The expression (eq. 5.1) for azimuthal velocity obtained in the experiment may be written in terms of dimensionless numbers,

$$U_\phi = 3.5\frac{\kappa}{D}RaE. \tag{5.7}$$

The westward drift of the secular variation is often associated with an azimuthal velocity of the liquid motion in the outer core; it about $5 \times 10^{-4} m/s$. If this zonal flow is caused by the same mechanisms responsible for that in our experiment then this implies that the Rayleigh number in the Earth's core is

$$Ra_{core}^{thermal} = \frac{D}{3.5\kappa}(5 \times 10^{-4}\ m/s)E^{-1}. \tag{5.8}$$

We use the estimates, $E \sim 10^{-15}$ (with $\nu \approx 10^{-6}\ m^2/s$ [22]), $\kappa \approx 5 \times 10^{-6}\ m^2/s$ [54] and the shell gap for the outer core, $D \approx 2 \times 10^6\ m$ to obtain

$$Ra_{core}^{thermal} = 6 \times 10^{22}. \tag{5.9}$$

One might guess that compositional convection is governed by similar physics. If Earth's zonal flow is driven by compositional convection, me may use a very similar argument to estimate the compositional Rayleigh number. In this case we replace κ with the compositional diffusion coefficient $D^{\xi} \approx 10^{-9}\ m^2/s$ [54] and arrive at,

$$Ra_{core}^{compositional} = 10^{25}. \tag{5.10}$$

These Ra estimates are both significantly lower than those made by Gubbins using an argument based on entropy [32]. He estimated $Ra^{thermal} \sim 10^{29}$ and $Ra^{compositional} \sim 10^{38}$.

5.1.2 *Convective flow velocity*

We may also derive an estimate for the turbulent convective velocities from our argument for convective heat flux. In the last chapter we established

$$(Nu - 1) Ra Pr^{-2} \sim Re^2 E^{-1/3}. \tag{5.11}$$

where the Reynolds number is based on convective velocities. If the Prandtl number is about 0.1, Nusselt number is between 1 and 10, and we use our estimate of $Ra \sim 10^{22}$ from above, then Earth's Reynolds number would be $Re \sim 10^7$ to 10^8. And since $Re \equiv U_{conv} D/\nu$ we can estimate the convective velocities in Earth's outer core,

$$U_{conv} \sim 10^{-4} \text{ to } 10^{-5}\ m/s, \tag{5.12}$$

which is about the same magnitude as the zonal flow, estimated from the westward drift. Our results suggest that this is also a reasonable estimate for convective velocities. This lends some some support to the idea that the ratio of toroidal to poloidal flow is optimally near unity for a dynamo [44].

5.1.3 *Time and length scales of convection*

Temperature power spectra from our experiments exhibit a dramatic change in power law slope at a distinct time scale determined by the ballistic frequency, $f_c = 2.0\Omega\sqrt{\alpha \Delta T}$. This is likely associated with the injection of energy into the flow by convective motions. There should exist a similar convective frequency in the outer core. The ballistic frequency in the Earth's core is

$$f \sim \Omega\sqrt{\alpha\Delta T} \approx 10^{-6}\ s^{-1}. \tag{5.13}$$

This yields a characteristic time for convective motions of

$$\tau_c \approx 1.7 \times 10^5 s \sim 2 \text{ days}. \tag{5.14}$$

If the frequency of fluctuations is due primarily to advection of a spatial temperature structures as we suspect in the experiment, then one may estimate a length scale associated with the cross-over frequency using the westward drift velocity:

$$\delta_c \sim \tau_c U_{drift} \sim 100\ m. \tag{5.15}$$

The observed cross-over frequency for the temperature power spectra seems to be governed by inertial and buoyancy effects and occurs at very small time and length scales. If there exists a similar cross-over in the magnetic field power spectrum this has implications for our understanding of the geodynamo. The minimum power required to drive the dynamo may be estimated by the Ohmic dissipation of the electric currents associated with the magnetic field. If there is significant power in the magnetic field down to length scales of order $100m$, this implies a large amount of Ohmic dissipation due to small scale magnetic fields. The more power there is dissipated, the larger the required energy sources to drive the geodynamo. Similar concepts were used by Roberts et al. to argue the case for the presence of radioactive potassium in Earth's outer core [53]. Their discussions were motivated by broad band magnetic field spectra observed in numerical dynamo simulations. Future experiments with larger applied magnetic fields should allow the measurement of magnetic field power spectra directly.

5.1.4 *Magnetic field and heat flux*

Our experiments support the idea that magnetic field suppresses convection on a global scale. This reinforces old ideas for a mechanism by which the geodynamo reaches a saturated average value of magnetic field. That is, the magnetic field grows until it suppresses convection sufficiently to stem further growth. Our experimental results also indicate that while the magnetic field decreases the total heat transfer, it may increase local heat transfer. If the local variations in heat transfer occur on large enough length scales, and long enough time scales, one might imagine that they would influence core-mantle thermal interactions and perhaps also persistent structures in the observable magnetic field (e.g. the Central Pacific low flux patch [36], [38]).

The applied magnetic fields in the experiments were close to constant in space and aligned with the rotation axis. This lead to a concentration of heat transport in the region that is coplanar with the inner sphere (i.e. the equatorial region). Although the magnetic field in Earth's core is certainly not as simple as the one applied for our experiments, the observed inhomogeneous heat flux suggests a mechanism for the seismically observed inhomogeneity of Earth's inner core. If there is a persistent structure to the magnetic field near the inner core, this will cause convection to occur more strongly in some regions than in others. The regions of the inner core surface where convection is most vigorous will grow most quickly. Although gravity ultimately forces it to become spherical, the inner sphere is likely formed by a process which is not spherically symmetric, due to

5.2 Future research suggestions

Three of the four years devoted to the research presented in this dissertation were spent designing, building, and debugging the apparatus and data acquisition systems. A great deal of science remains untapped in future experiments with this apparatus. I will list some suggested avenues and improvements for future research with the apparatus, starting with those that require the least modification to the apparatus.

- Add a thermally insulating layer of material (say, teflon) to the bottom shaft. This would reduce unwanted convection due to the bottom shaft being cooler than the sodium.
- Add more pairs of thermistors at different depths through the outer sphere wall at different positions. It would be interesting to map out the polar angle dependence of heat transfer and how it changes with the control parameters.

- Implement an accurate flow meter for the coolant fluid. In conjunction with measurements of the temperature difference between the fluid entering and exiting the inner sphere, the coolant flow rate would facilitate a measurement of global heat flux. It would be interesting to compare global heat flux measurements to local ones.

- More extensive study of applied magnetic field effects. Larger applied magnetic fields and more sensitive magnetic field sensors would both yield interesting physics. Perhaps there exists a similar inertia-diffusion cross-over in the magnetic field power spectrum, as we observed in the temperature power spectra. Also, with an Elsasser number closer to 1, there will surely be interesting dynamics to observe.

- Water or perhaps silicon oil experiments with the same device. With a higher Prandtl number fluid, one could reach higher Ra numbers than in any previous experiments. During preliminary test runs with water in this device, regular very slow oscillations ($\approx 300s$ period) were observed. It would be interesting to carefully explore these dynamics.

- Balance the sphere for higher rotation rates. The device was designed to operate at rotation rates up to 100 Hz. Reaching this speed would increase the Rayleigh number by a factor of 16 from the highest Ra thus far attained. In addition, possibly interesting effects due to fluid compression may exist at higher rotation rates.

- Ultrasound measurements of fluid velocity. If the apparatus is not rotated too rapidly, then there is no reason we should not be able to implement ultrasound measurements using slip rings to pass signals to and from the rotating frame. Direct velocity measurements would add to our results considerably.

Appendix A

GLOBAL DISSIPATION

In deriving the global dissipation it will be assumed that the vessel is cylindrical rather than spherical. This simplifies the argument and likely introduces only an order unity error as is typical for geometrical corrections. The cylindrical geometry has been used successfully to learn more about the spherical case in a number of analytical and numerical studies (e.g. [12], [49]). We also assume that the system is in steady state: volume averages are stationary in time. We will begin by deriving exact relations for global dissipation. The viscous dissipation $\epsilon_\nu \equiv \nu(\nabla \mathbf{v})^2$ may be rewritten,

$$\epsilon_\nu = \nu\nabla(\mathbf{v}\nabla\mathbf{v}) - \nu\mathbf{v}\cdot\nabla^2\mathbf{v}. \tag{A.1}$$

Then we may replace the second term on the righthand side $\nu\nabla^2\mathbf{v}$ from the Navier-Stokes equation to get,

$$\epsilon_\nu = \nu\nabla(\mathbf{v}\nabla\mathbf{v}) - \mathbf{v}\cdot\big[\partial_t\mathbf{v} + (\mathbf{v}\cdot\nabla)\mathbf{v} + \nabla p + 2\Omega\mathbf{e_z}\times\mathbf{v} + \Omega^2 r\alpha T\mathbf{e_r}\big]. \tag{A.2}$$

Now we take a volume average of each term,

$$\langle\epsilon_\nu\rangle_V = \langle\nu\mathbf{v}\nabla\mathbf{v}\rangle_A - \langle\mathbf{v}\cdot(\mathbf{v}\cdot\nabla)\mathbf{v}\rangle_V - \langle\mathbf{v}\cdot\nabla p\rangle_V - \langle 2\Omega\mathbf{v}\cdot(\mathbf{e_z}\times\mathbf{v})\rangle_V - \langle\Omega^2 r\alpha T v_r\rangle_V, \tag{A.3}$$

where $\langle\rangle_V$ indicates a volume average and $\langle\rangle_A$ is an average over the surface of the volume. The first term changes to an area integral with the divergence theorem and since the fluid velocity goes to zero at the walls this term is zero. The time derivative term vanishes since the system is in steady state. The Coriolis term also vanishes since $\mathbf{v}\perp\mathbf{e_z}\times\mathbf{v}$. The fact that the system is rotating has no effect on the total viscous dissipation except through the buoyancy force. This leaves only the advective, pressure, and buoyancy terms, which may be manipulated to yield,

$$\langle\epsilon_\nu\rangle_V = -\langle\mathbf{v}\frac{v^2}{2}\rangle_A - \langle\mathbf{v}p\rangle_A - \alpha\Omega^2\langle rTv_r\rangle_V. \tag{A.4}$$

The the derivative ∇ in the advective and pressure terms was moved to the left of all the velocity factors with the help of the incompressibility condition, $\nabla\cdot\mathbf{v} = 0$. With the derivative on the left, the divergence theorem was again applied and allows us to eliminate both of the area integrals for the same reasons as used before. This leaves only one remaining integral of the buoyancy force,

$$\langle\epsilon_\nu\rangle_V = \frac{\alpha\Omega^2}{D^3}\int_r r\left(\int_A T v_r \mathrm{d}A\right)\mathrm{d}r. \tag{A.5}$$

The area integral is over surfaces of constant radius and is equal to the convective heat flux Q_{conv} up to factors of ρ and c_p,

$$\langle\epsilon_\nu\rangle_V = \frac{\alpha\Omega^2}{D^3}\int_r r\frac{Q_{conv}}{\rho c_p}\mathrm{d}r. \tag{A.6}$$

Recall the definition of definition of the Nusselt number,

$$\begin{aligned} Nu &\equiv \frac{Q_{conv}+Q_{cond}}{Q_{cond}}, && \text{(A.7)}\\ \Longrightarrow Q_{conv} &= (Nu-1)Q_{cond}, && \text{(A.8)}\\ Q_{conv} &= (Nu-1)kD\Delta T, && \text{(A.9)} \end{aligned}$$

where the total conducted heat is $Q_{cond} = kD\Delta T$ and k is the thermal conductivity. Integrating and replacing Q_{conv}, eq. A.6 becomes approximately

$$\begin{aligned} \langle\epsilon_\nu\rangle_V &\approx \frac{\alpha\Omega^2}{D^3}(Nu-1)\frac{k\Delta T D^2}{c_p\rho D}\frac{D^2}{2}, && \text{(A.10)}\\ &= \alpha\Delta T\Omega^2 D^4(Nu-1)\frac{\kappa}{D^4}, && \text{(A.11)}\\ &= Ra(Nu-1)\frac{\kappa^2\nu}{D^4}. && \text{(A.12)} \end{aligned}$$

Then the relation for global viscous dissipation is

$$\langle\epsilon_\nu\rangle_V = \frac{\nu^3}{D^4}RaPr^{-2}(Nu-1). \tag{A.13}$$

A similar procedure is followed to derive the value for global thermal dissipation $\langle\epsilon_T\rangle_V \equiv \langle\kappa(\nabla T)^2\rangle_V$. As before, we recast the dissipation with some simple vector algebra, $(\nabla T)^2 = \nabla\cdot(T\nabla T) - T\nabla^2 T$, and the temperature equation to get

$$\langle\epsilon_T\rangle_V = \langle\kappa\nabla\cdot(T\nabla T)\rangle_V - \langle T\partial_t T\rangle_V - \langle T(\mathbf{v}\cdot\nabla)T\rangle_V. \tag{A.14}$$

The time derivative is zero since volume averages are stationary. With the divergence theorem applied to the first term and moving the spatial derivative to the left in the last term, we have

$$\langle\epsilon_T\rangle_V = \langle\kappa(T\nabla T)\rangle_A - \langle\mathbf{v}\frac{T^2}{2}\rangle_A. \tag{A.15}$$

The last term vanishes with the vanishing velocity on the boundary. It is instructive to break up the surface area integral of the remaining term into the contributions of the outer, inner, top, and bottom surfaces,

$$\langle\kappa(T\nabla T)\rangle_A = \frac{1}{D^3}\int_{outer} T\partial_r T \mathrm{d}A - \frac{1}{D^3}\int_{inner} T\partial_r T \mathrm{d}A + \frac{1}{D^3}\int_{top} T\partial_z T \mathrm{d}A - \frac{1}{D^3}\int_{bottom} T\partial_z T \mathrm{d}A. \tag{A.16}$$

It is assumed that the top and bottom are thermally insulated well enough that the thermal gradient $\partial_z T$ is close to zero, making the top and bottom contributions negligible. It is also assumed that temperatures are constant, T_i and T_o on the inner and outer surfaces. This is one way that the model does not represent the experiment well, as the outer boundary in the experiment is closer to a constant heat flux boundary condition. Recognizing that the integral of the normal temperature gradient integrated over a surface is the total heat flux through that surface divided by k, we have

$$\begin{aligned}\langle\epsilon_T\rangle_V &= \kappa\frac{T_o}{kD^3}(Nu)Q_{cond} - \kappa\frac{T_i}{kD^3}(Nu)Q_{cond} && \text{(A.17)}\\ &= \kappa\frac{\Delta T}{kD^3}\frac{Nu\Delta T D^2 k}{D}, && \text{(A.18)}\end{aligned}$$

where $\Delta T = T_o - T_i$ and Q_{cond} is replaced as before. The global average of thermal dissipation is then

$$\langle\epsilon_T\rangle_V = \kappa\frac{\Delta T^2}{D^2}Nu. \tag{A.19}$$

Appendix B

CONTROL AND DATA PROCESSING CODE

B.1 **Shell scripts**

This shell script is used to change binary data to ASCII. The program takes as input the files written by the Labview program, *stod.vi*, which receives data from the PIC chip on the rotating assembly. The script is called *ariv14*.

```
#!/bin/tcsh
while (1)
if (‘ls -l  | head -n2 | tail -1 | awk ’{print $5}’‘ <= "3840") then
sleep 1
else
    set dat = ‘ls -1 |head -1‘
    seri $dat > temp
    set zeit = ‘head -1 temp | awk ’{print "rot"int($1)}’‘
    set hot0 = ‘awk ’{sum+=$2;n++}END{print sum/n}’ temp‘
    echo $hot0 > tdat
        set hot1 = ‘awk ’{sum+=$3;n++}END{print sum/n}’ temp‘
        echo $hot1 >> tdat
        set hot2 = ‘awk ’{sum+=$4;n++}END{print sum/n}’ temp‘
        echo $hot2 >> tdat
        set hot3 = ‘awk ’{sum+=$5;n++}END{print sum/n}’ temp‘
        echo $hot3 >> tdat
        set hot4 = ‘awk ’{sum+=$6;n++}END{print sum/n}’ temp‘
        echo $hot4 >> tdat
        set hot5 = ‘awk ’{sum+=$7;n++}END{print sum/n}’ temp‘
        echo $hot5 >> tdat
        set hot6 = ‘awk ’{sum+=$8;n++}END{print sum/n}’ temp‘
        echo $hot6 >> tdat
        set hot7 = ‘awk ’{sum+=$9;n++}END{print sum/n}’ temp‘
```

```
        echo $hot7 >> tdat
        set hot8 = `awk '{sum+=$10;n++}END{print sum/n}' temp`
        echo $hot8 >> tdat
        set hot9 = `awk '{sum+=$11;n++}END{print sum/n}' temp`
        echo $hot9 >> tdat
    cp tdat  ../depot
    mv temp ../$1/$zeit
    rm -f $dat
endif
end
```

This next script is used to compute delay times used for computing azimuthal velocities. It is called *dotautall*.

```
#!/bin/tcsh
set list = `ls -1 fixts* | sort -n -k1.6`
foreach i ($list)
echo $i '\c'
set mean4 = `awk '{print $4}' $i | meanvar`
set mean5 = `awk '{print $5}' $i  | meanvar`
awk '{print ($4-'$mean4[1]')/'$mean4[3]'}' $i | avenb 8 | scale -af > junk
awk '{print ($5-'$mean5[1]')/'$mean5[3]'}' $i  | avenb 8 | scale -af> junk2
tautest3 junk junk2 -40 40 1512 16 > junk3
awk '$3<1.5{print $2}' junk3 | scale -af | invar1 7 > junk4
awk '$2>0.01{print $1,$2}' junk4 | draw -mc | gplot
awk '$2>0.01{print $1,$2}' junk4 | awk '{sumn+=$2; sumn2+=$2*$2; sumn3+=$2*$2*$2;
    sum1+=$1*$2; sum2+=$1*$2*$2; sum3+=$1*$2*$2*$2}END{print
    sum1/sumn,(sum2/sumn2),(sum3/sumn3)}'
end
```

B.2 Labview code

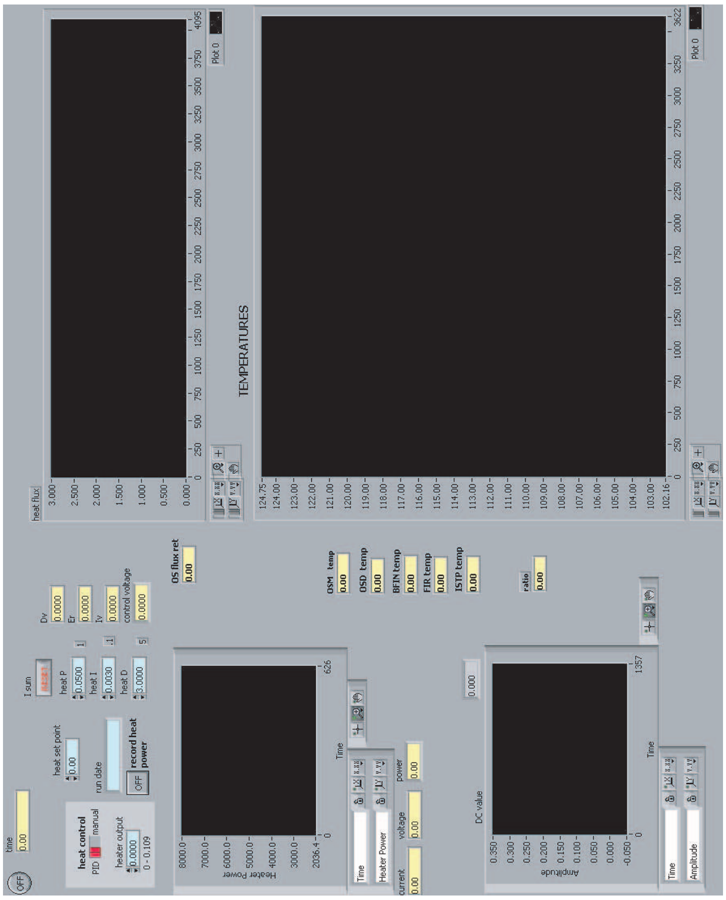
time 0.00

heat control PID manual

heater output 0.0000

0 - 0.109

heat set point 0.00

run date

record heat power OFF

I sum RESET

heat P 0.0500

heat I 0.0030

heat D 3.0000

Dv 0.0000

Er 0.0000

Iv 0.0000

control voltage 0.0000

OS flux ret 0.00

OSM temp 0.00

OSD temp 0.00

BFIN temp 0.00

FIR temp 0.00

ISTP temp 0.00

ratio 0.00

power 0.00

voltage 0.00

current 0.00

DC value 0.000

Figure B.1: Front panel of Labview program (Temp022504.vi) used to monitor temperatures and control the heating system.

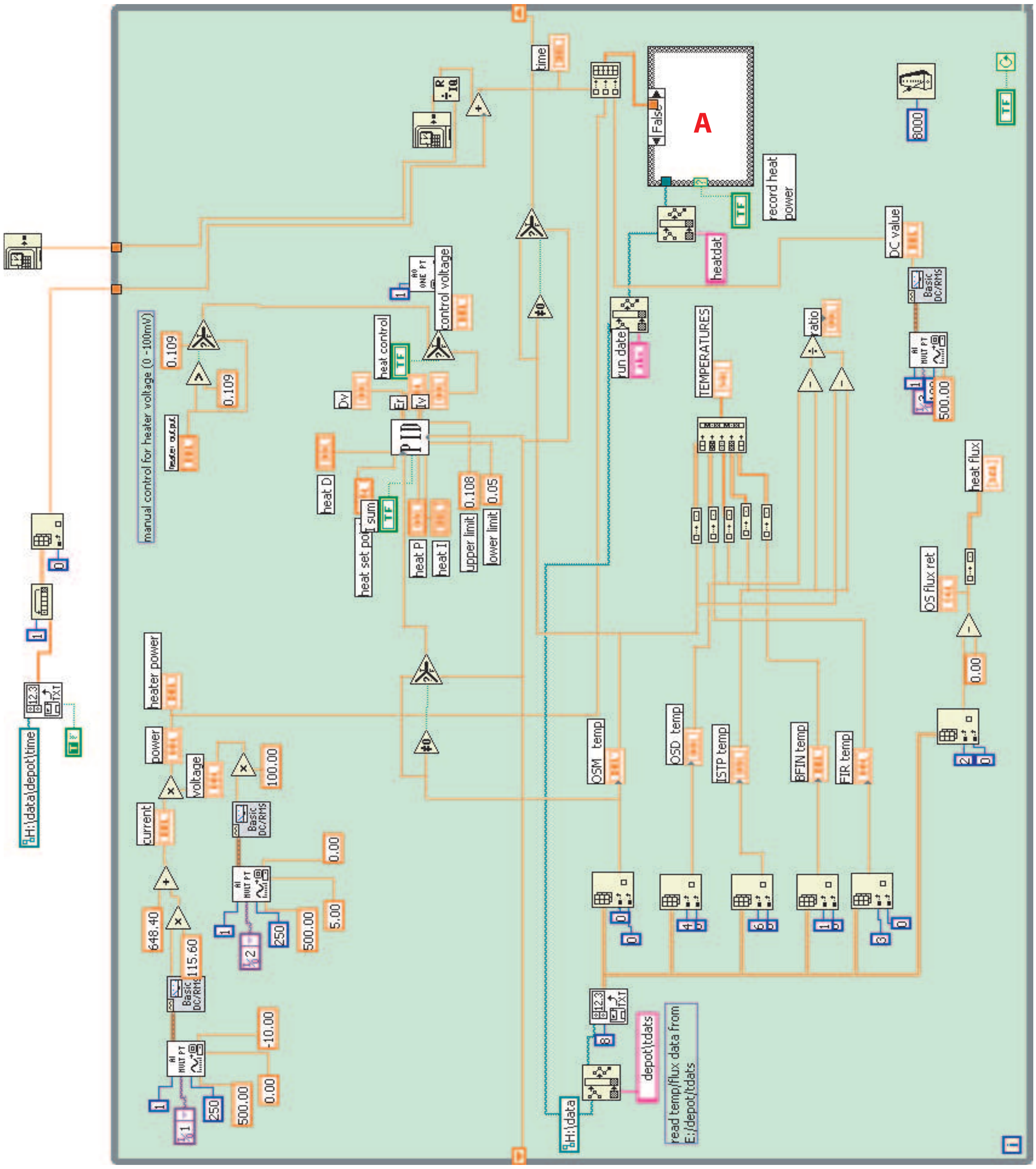

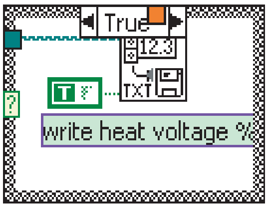

other case for TF box A

Figure B.2: Code diagram of Labview program (Temp022504.vi) used to monitor temperatures and control the heating system.

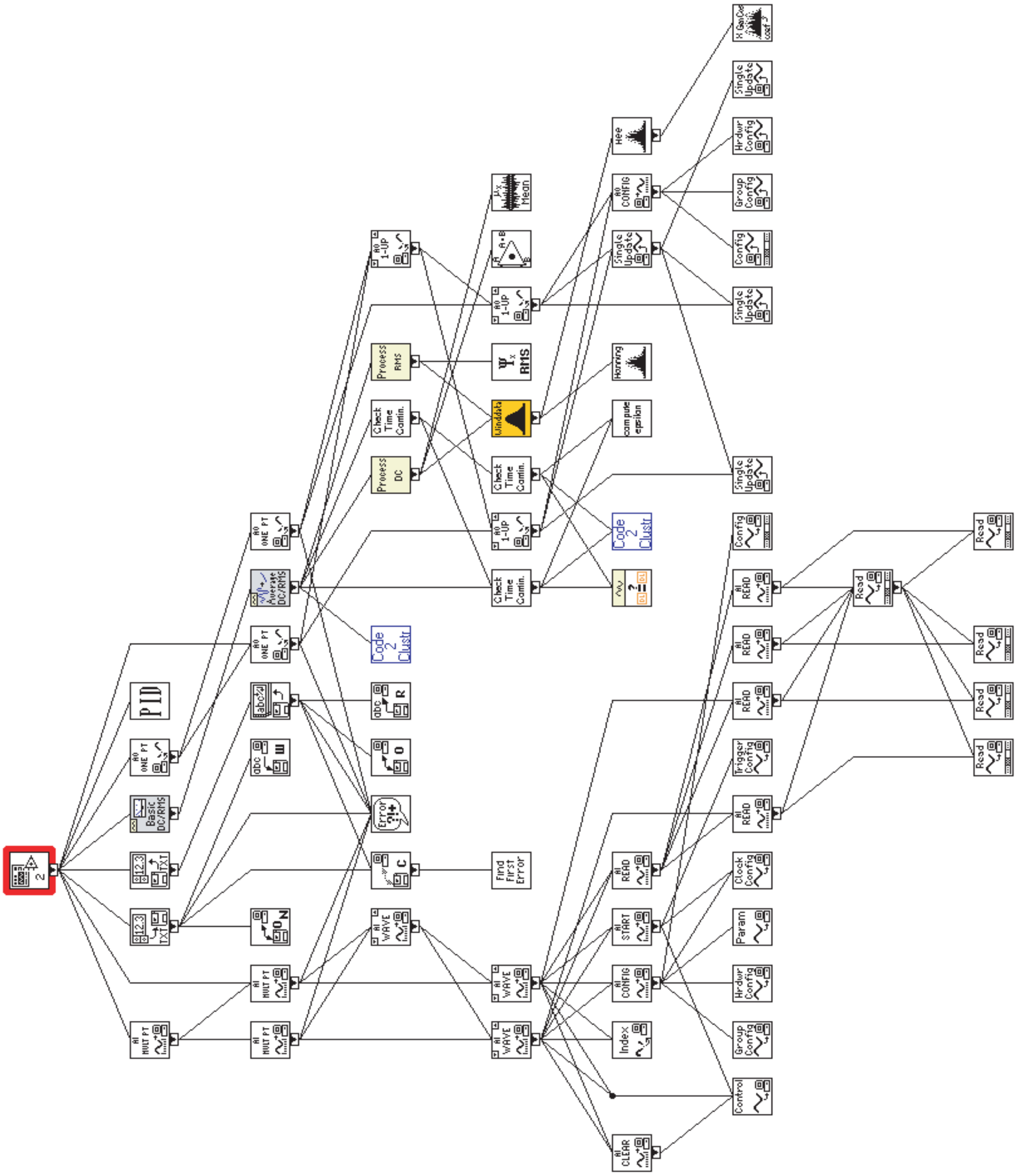

Figure B.3: VI hierarchy of Labview program (Temp022504.vi) used to monitor temperatures and control the heating system.

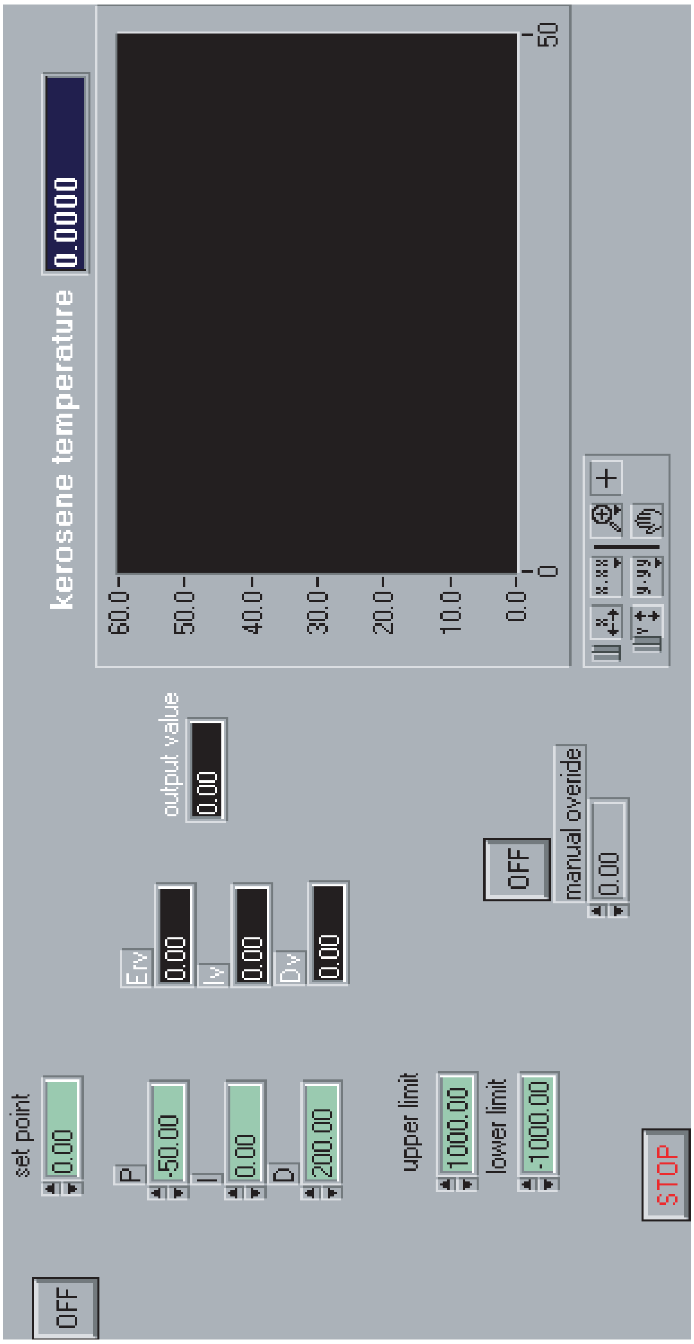

kerosene temperature 0.0000

set point 0.00

P -50.00

I 0.00

D 200.00

upper limit 1000.00

lower limit -1000.00

E.rv 0.00

Iv 0.00

Dv 0.00

output value 0.00

manual overide 0.00

Figure B.4: Front panel of Labview program (coolcontrol041204.vi) used to monitor temperatures and control the cooling system.

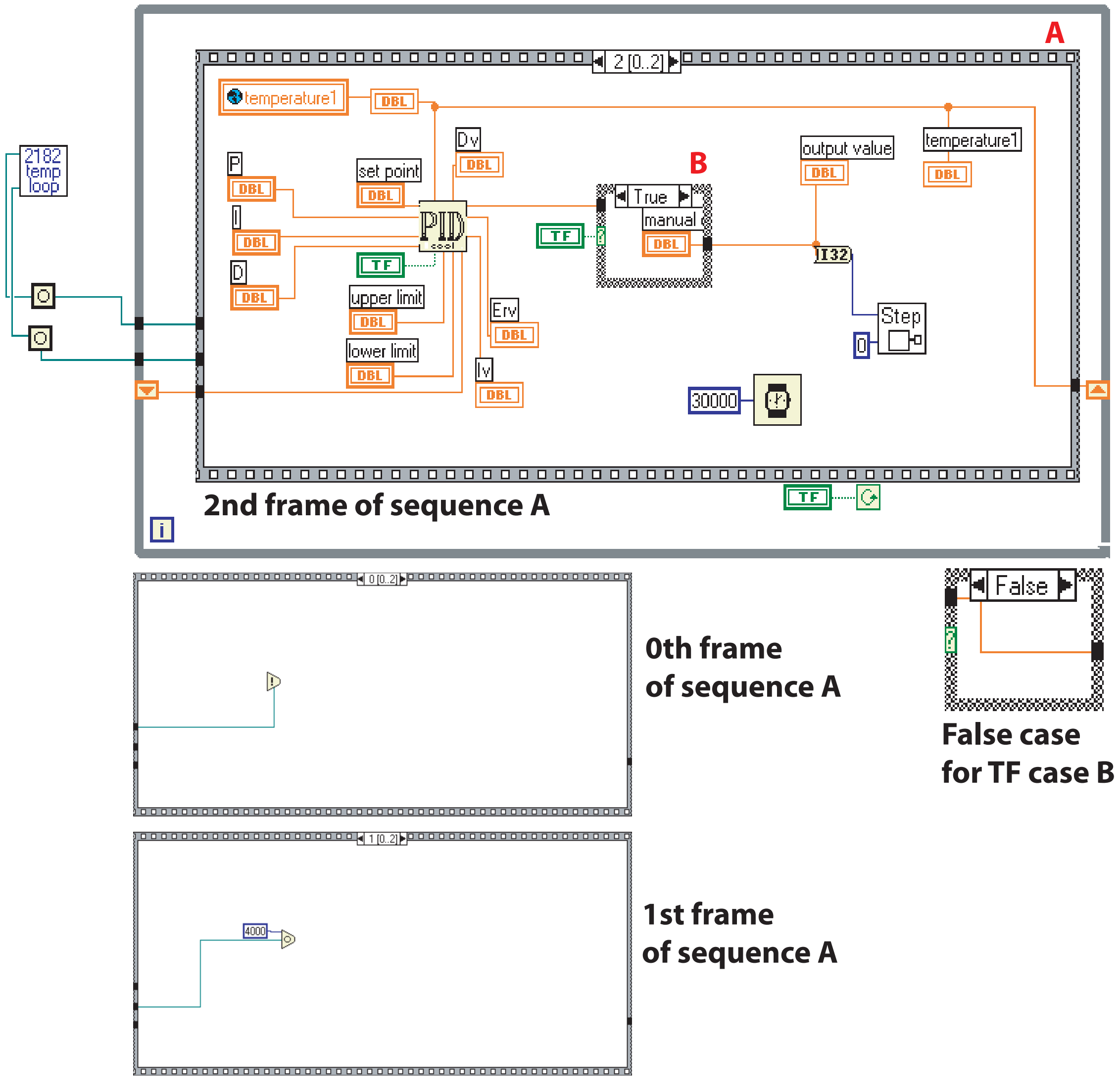

Figure B.5: Code diagram of Labview program (coolcontrol041204.vi) used to monitor temperatures and control the cooling system.

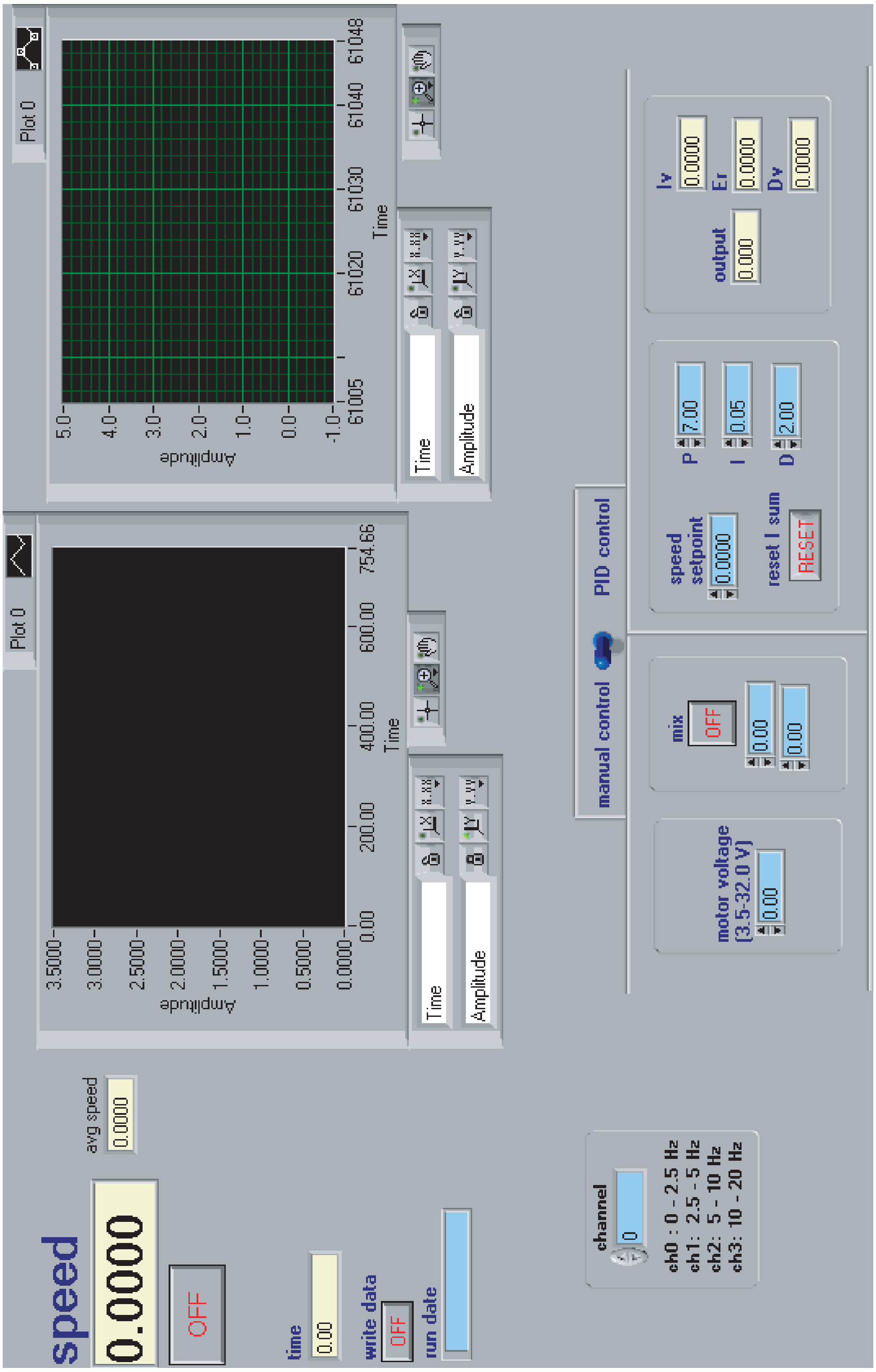

Figure B.6: Front panel of Labview program (rot011204.vi) used to monitor and control rotation rate of the sphere.

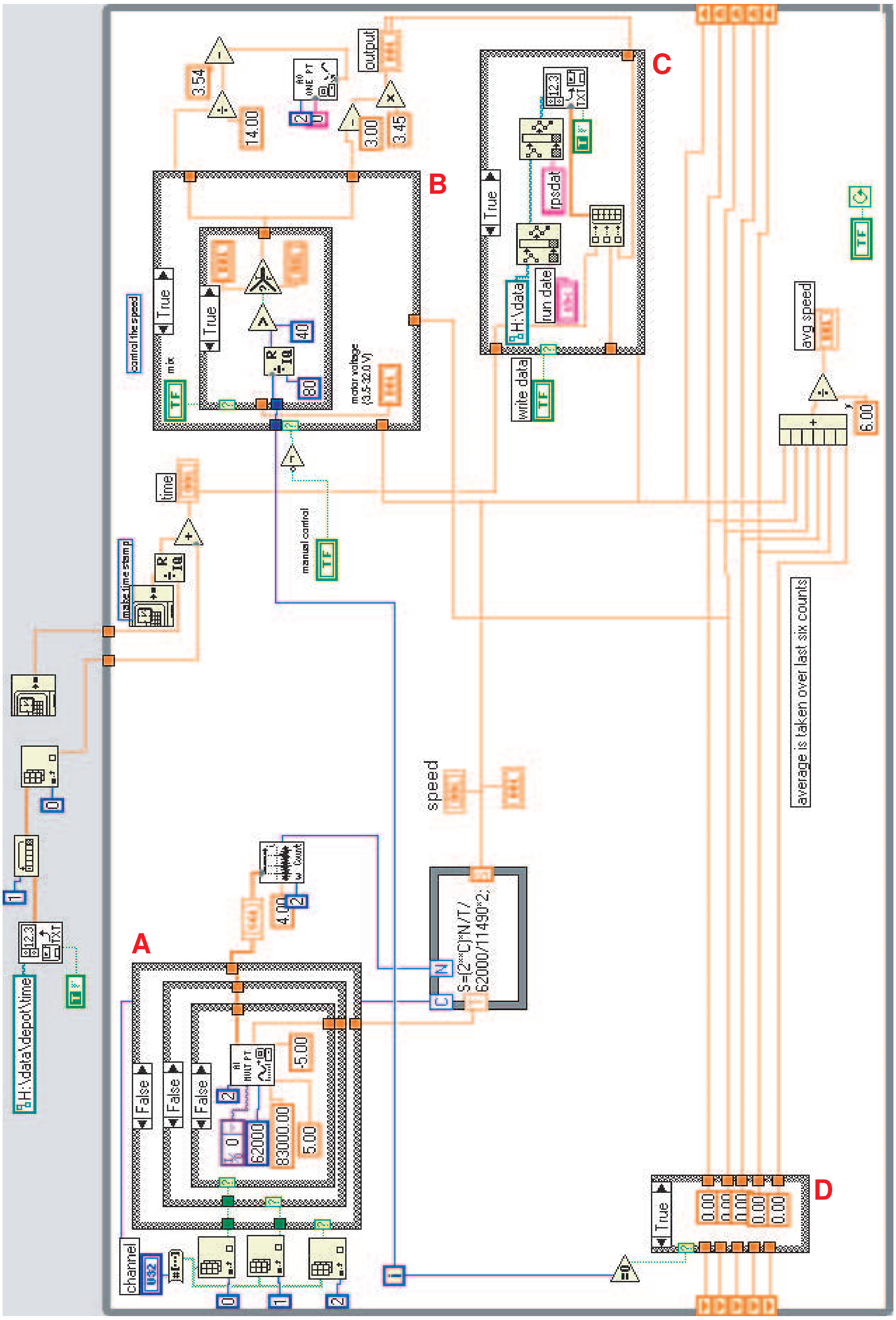

Figure B.7: Code diagram (part 1) of Labview program (rot011204.vi) used to monitor and control rotation rate of the sphere.

TF case A: This set of nested case statements just switches between which channel of the rotation rate counter is read. Channel 0 is for slow rotation rates. Channel 1 counts half the pulses of Channel 0, and therefor is for rotation rates twice as large. Channel 2 halves the count again, etc.

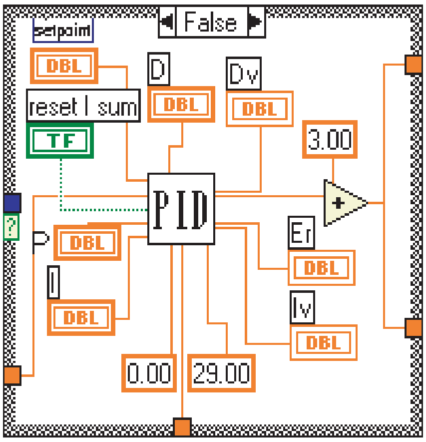

TF case B: This is the case for PID control rather than manual control.

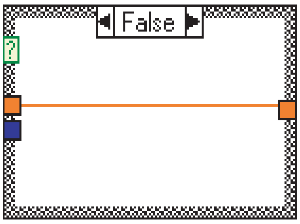

TF case C: This is the case for when data is not written to file.

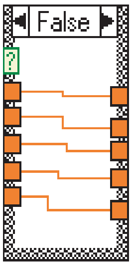

TF caseD: When true the history is all set to zero.

Figure B.8: Code diagram (part 2) of Labview program (rot011204.vi) used to monitor and control rotation rate of the sphere.

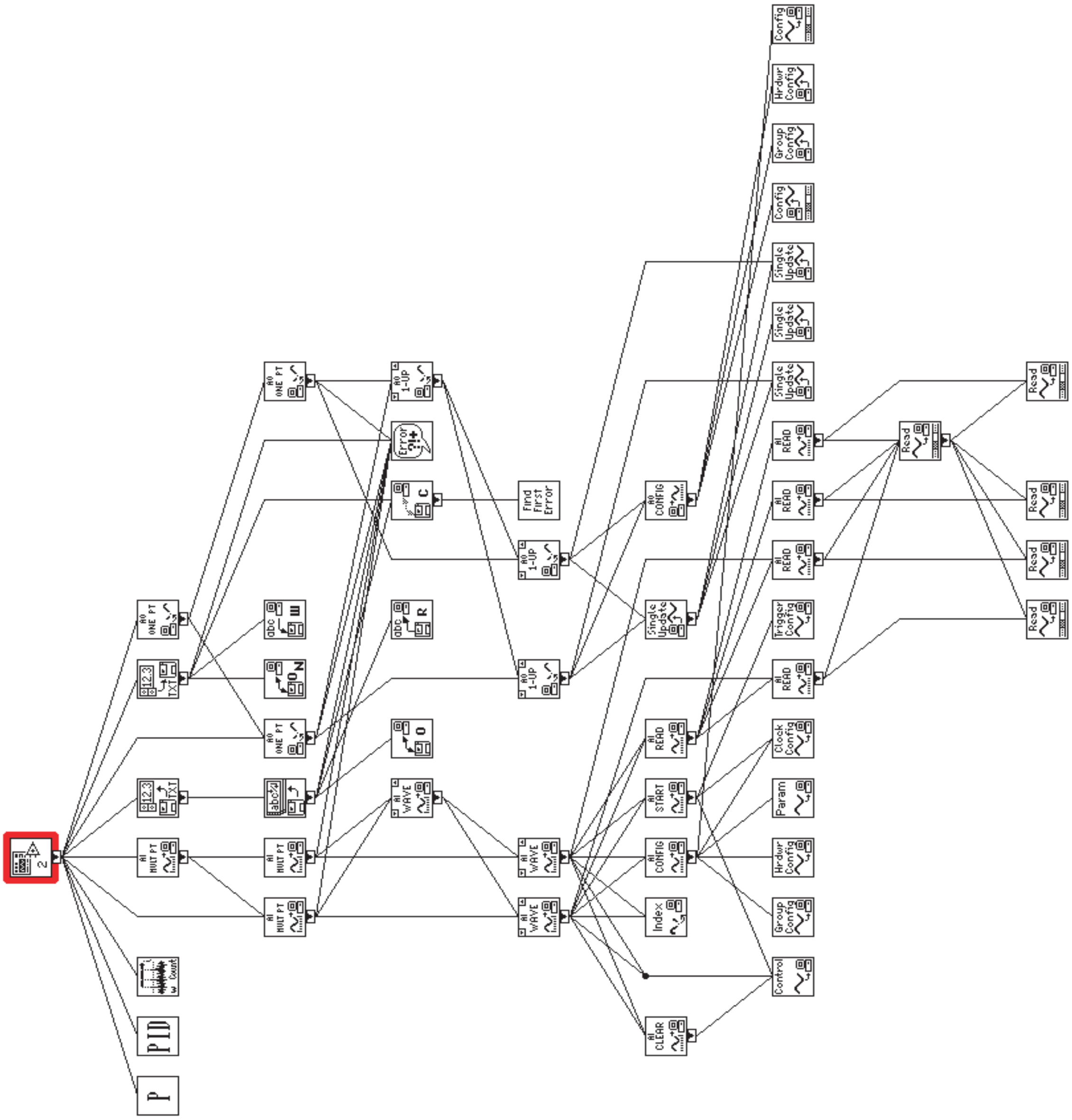

Figure B.9: VI hierarchy of Labview program (rot011204.vi) used to monitor and control rotation rate of the sphere.

Figure B.10: Front panel of Labview program (stod0061704.vi) used to acquire the serial digital data coming from the measurement probes on the rotating assembly.

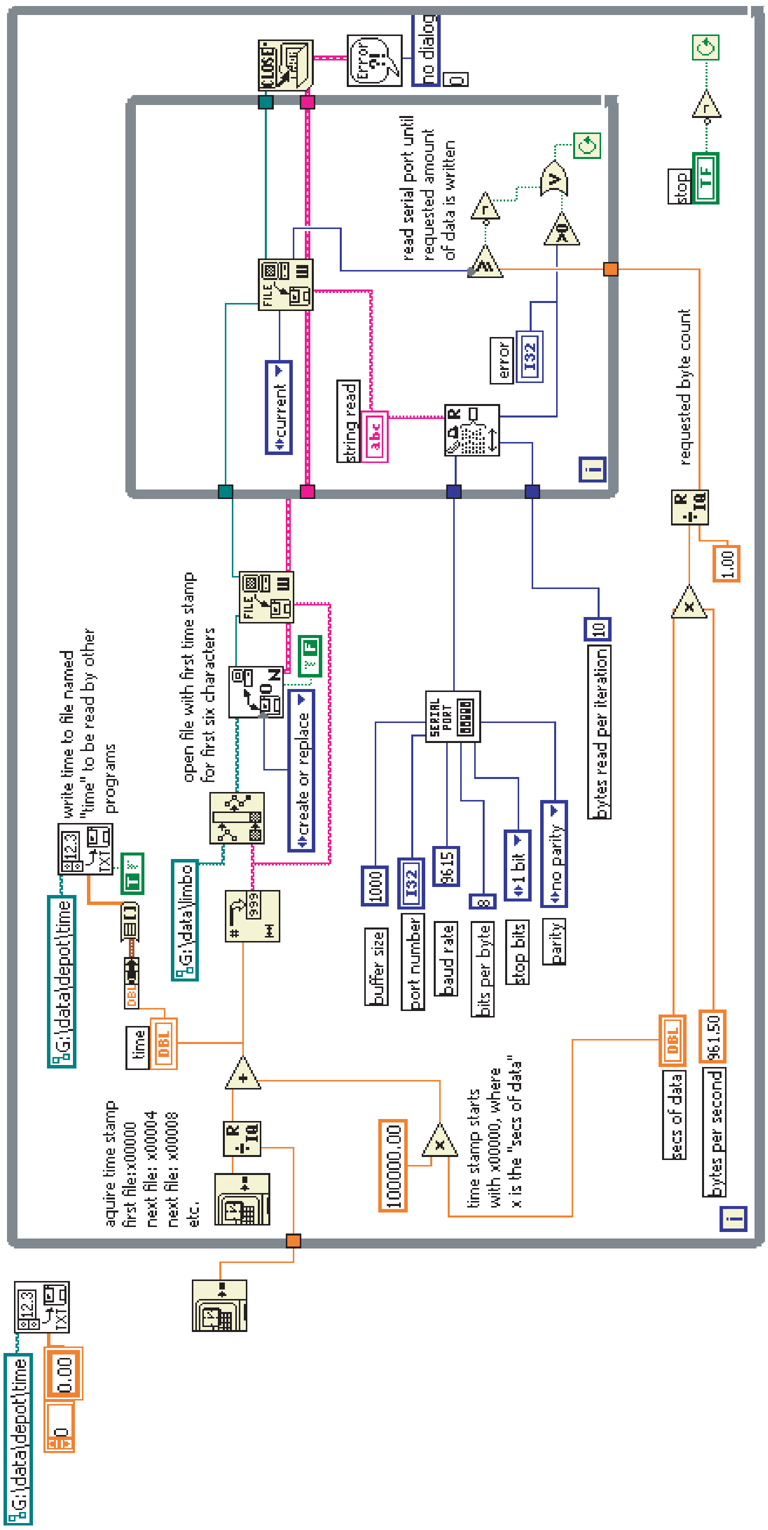

Figure B.11: Code diagram of Labview program (stod0061704.vi) used to acquire the serial digital data coming from the measurement probes on the rotating assembly.

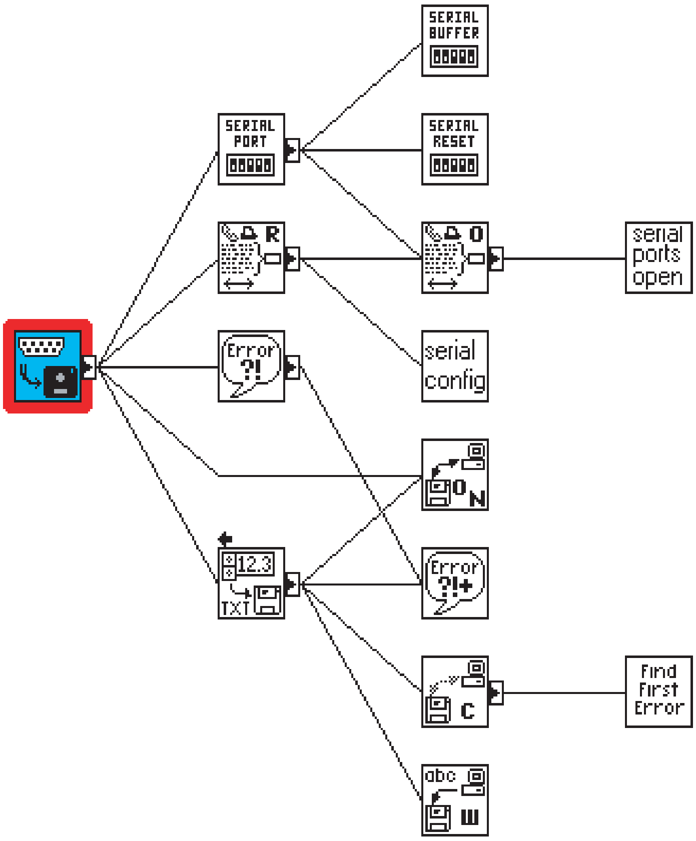

Figure B.12: VI hierarchy of Labview program (myPID2.vi) used to acquire the serial digital data coming from the measurement probes on the rotating assembly.

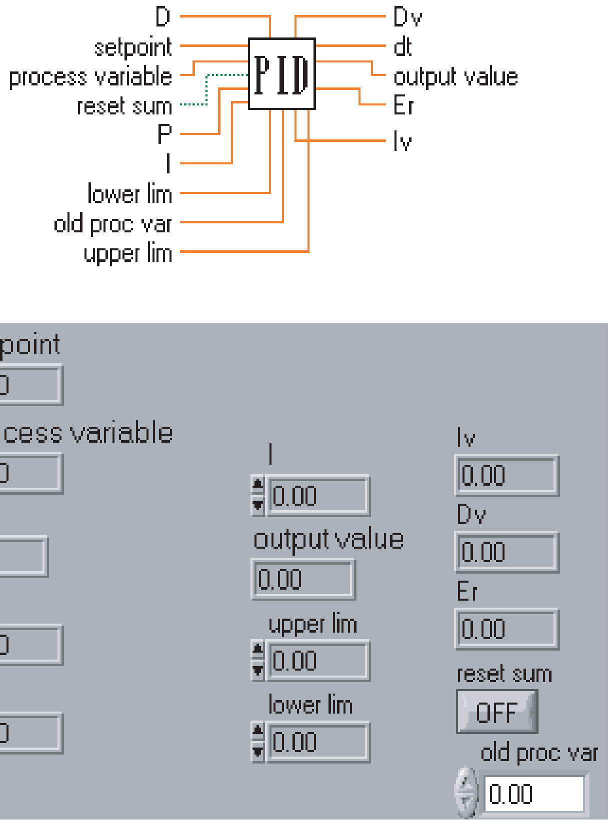

setpoint 0.00
process variable 0.00
dt 0.00
P 0.00
D 0.00
I 0.00
output value 0.00
upper lim 0.00
lower lim 0.00
Iv 0.00
Dv 0.00
Er 0.00
reset sum OFF
old proc var 0.00

Figure B.13: Front panel of Labview program (myPID2.vi) used in the above Labview codes to control heater and motor power supplies and the coolant control valve.

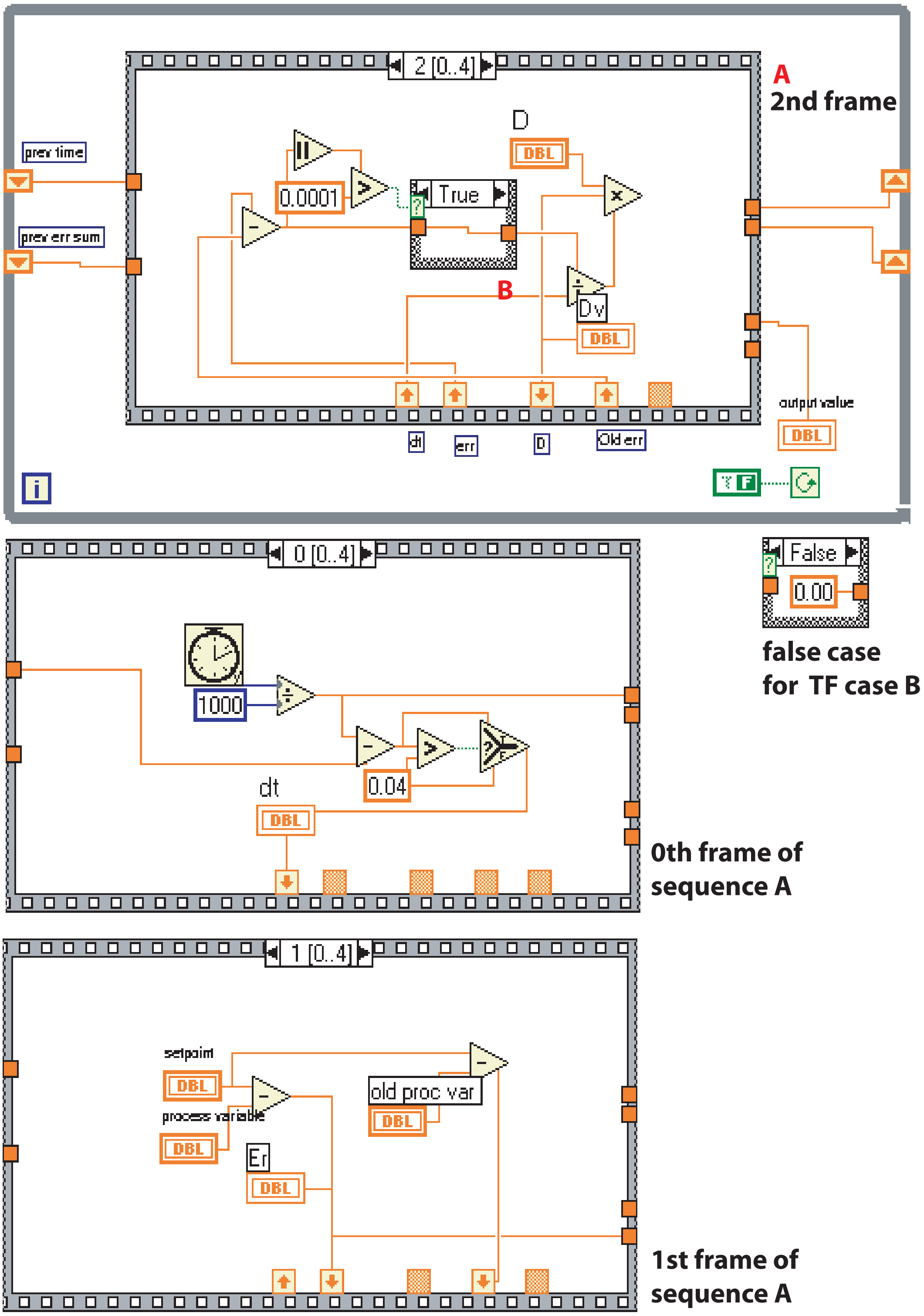

Figure B.14: Code diagram of Labview program (myPID2.vi) used in the above Labview codes to control heater and motor power supplies and the coolant control valve.

B.3 C code

This program was used to extract the data coming from the PIC chip. As transmitted by the PIC chip the data is a continuous stream of bits with this format: start bit, 8 bits, stop bit. These 8 bit chunks between the start and stop bits are of two types: one has a 4 bit label and the low 4 bits of the signal, the other is the high 8 bits of the signal. See the PIC code in next section for more detail. The code below extracts the full 12 bit signal and puts it into ten columns based on label value. This code is called *dplnew.c*.

```
#include <stdio.h>

#include <math.h>

main(argc, argv)

int argc;

char *argv[];

{

    char words[16384],tmp;

    float start, field;

    int i,j,n;

    FILE *fpi,*fpo;

    if  ((fpi=fopen(argv[1],"r"))==NULL) {

        fprintf(stderr,"File opened is stdin for input\n");

        fpi=stdin;

    }


    start=atof(argv[1]+1);

    for (i=0; !feof(fpi); i+=2) {

        fread(&tmp,1,1,fpi);

        words[i+1]= (tmp&0xf);

        words[i]= (tmp>>4);
```

```
    }
    n=i-2;
    for (i=0; i<n; i++) {
        if ( words[i]==0 && words[i+4]==1 && words[i+8]==2 &&
        words[i+12]==3 && words[i+16]==4 && words[i+20]==5 &&
        words[i+24]==6 && words[i+28]==7 && words[i+32]==8 &&
        words[i+36]==9 ) {
            if(i%2==0){
                printf("%4.3f ",start+(5.0*i)/9600.0);
            }else{
                printf("%4.3f ",start+(5.0*i-1)/9600.0);
            }
            for (j=0; ((i+j+3<16384)&&(j<40)); j+=4) {
                field=words[i+j+3]+16*words[i+j+2]
                    +256*words[i+j+1];
                printf("%g ",5.0*field/4095.0);
                /*printf("%g ",field);*/
            }
            printf("\n");
        }
    }
    exit(0);
}
```

This next program is called by the script, *dotautall*, used to compute the delay between two time series. This delay time is used to estimate zonal velocities from temperature time series of closely spaced temperature probes. The code is named *tautest3.c.*

```
#include <stdio.h>
```

```
#include <math.h>

#define abs(x) ((x) < 0.0 ? -(x) : (x))

#define size 64

unsigned int b[32];

main(argc, argv)

int argc;

char *argv[];

{

    FILE *fpi,*fpi2,*fpo;

    double x,y,sum=0,mean,dxdu;

    float dataa[524288],datab[524288];

    double a,d,x0,epsilon,min,max,sumx,sumy,sumz,sumx2,sumxy,slopek;

    double sumu,sumd;

    int location,i,j,k=0,l=0,m,n,r,t,inorder,unbound;

    int p[size][size],pa[size],pb[size];

    int tsum,tmin,tmax,tstep,Nt;

    float mina,minb,maxa,maxb;

    float s;

    if  ((fpi=fopen(argv[1],"r"))==NULL) {

        fprintf(stderr,"File opened is stdin for input\n");

        fpi=stdin;

    }

    if  ((fpi2=fopen(argv[2],"r"))==NULL) {

        fprintf(stderr,"File opened for fpi2 is  stdin for input\n");

        fpi2=stdin;

    }

    tmin=atoi(argv[3]);
```

```
tmax=atoi(argv[4]);

tstep=1;

location=atoi(argv[5]);

m=atoi(argv[6]);

min=20000; max= -20000;

for (n=0; fread(&s,sizeof(float),1,fpi)==1; n++) {

    dataa[n]=(float)(s);

    if (dataa[n]<min) min=dataa[n];

    if (dataa[n]>max) max=dataa[n];

}

mina=min; maxa=max;

min=20000; max= -20000;

for (n=0; fread(&s,sizeof(float),1,fpi2)==1; n++) {

    datab[n]=(float)(s);

    if (datab[n]<min) min=datab[n];

    if (datab[n]>max) max=datab[n];

}

for (i=0; i<size; i++) {pa[i]=0; pb[i]=0;}

for (i= -tmin; i<n-tmax-m; i++) {

min=20000; max= -20000;

    for (t=tmin; t<tmax; t+=tstep) {

        Nt=0; sum=0;

        for (j=0,sum=0; j<m; j++)

            sum+=abs(dataa[i+j]-datab[i+j+t]);

        if (sum<min) {min=sum; tsum=t;}

    }

    if (tsum<tmax-1) printf("%d %d %g\n",i,tsum,min);
```

```
    }

}
```

B.4 PIC code

This is the code which is burnt into the 16C773 PIC microcontroller. The burning is facilitated with software and hardware furnished by Microchip. The software is called MPLAB. The hardware is a small box with 40 pin dip socket, which plugs into the serial port of the PC running the MPLAB software. When burning the chip be sure to set the configuration bits as prescribed at the end of the following code.

```
   LIST    p=16C774

    INCLUDE  <p16C774.inc>


    CLRF    0x7F

start


    ;*********    d/a init   **************


    MOVLW   0x81        ;Set AD clock to Fosc/32, turn on converter

    MOVWF   ADCON0      ;Select ch0


    ;*********   channel selection   ************


    BTFSC   0x7F,0

    BSF ADCON0, CHS0

    BTFSC   0x7F,1

    BSF ADCON0, CHS1

    BTFSC   0x7F,2

    BSF ADCON0, CHS2

    BTFSC   0x7F,3

    BSF ADCON0, CHS3


    ;*********   d/a conversion   ****************
```

```
    MOVLW   0x19        ;Wait for S&H to settle

    MOVWF   0x21        ;Set 0x21 to 25

wait0   DECFSZ  0x21, 1     ;Count down from 25 (75 inst. cycles)

    GOTO    wait0


    BSF ADCON0, GO  ;Start conversion

wait1   BTFSC   ADCON0, GO  ;Wait for conversion to finish

    GOTO    wait1




    ;*********   USART output   ****************


    BSF STATUS, RP0 ;Select bank 1

    BSF TXSTA, BRGH ;High speed baud rate

    MOVLW   0x81        ;Set baud rate to 9600 bps

    MOVWF   SPBRG

    BCF TXSTA, SYNC ;Set to asyncronous mode

    BSF     TXSTA, TXEN ;Enable transmit

    BCF STATUS, RP0 ;Select bank 0

    BSF RCSTA, SPEN ;Enable serial ports


wait2   BTFSS   PIR1, TXIF  ;Make sure TXREG is empty

    GOTO    wait2


    BSF STATUS, RP0 ;Select bank 1

    MOVF    ADRESL, 0   ;Move ADRESL to output

    ADDWF   0xFF, 0     ;Put channel label on empty first four bits
```

```
    BCF STATUS, RP0 ;Select bank 0
    MOVWF   TXREG

    BCF STATUS, RP0 ;Select bank 0
wait3   BTFSS   PIR1, TXIF  ;Make sure TXREG is empty
    GOTO    wait3

    MOVF    ADRESH, 0   ;Move ADRESH to output
    MOVWF   TXREG



    ;*********   increment channel   ****************


    MOVLW   0xF6
    ADDWF   0x7F, 1
    INCFSZ  0x7F, 1
    SUBWF   0x7F, 1

    GOTO    start
    END



;Configuration Bits  HS,on,off,off,disabled,2.5v
```

BIBLIOGRAPHY

[1] O. L. Anderson and A. Duba, Experimental melting curve of iron revisited. *J. Geophys. Res.* **102**, 22659 (1997).

[2] J. Aubert, D. Brito, H.-C. Nataf, P. Cardin, and J.-P. Masson, A systematic experimental study of rapidly rotating spherical convection in water and liquid gallium. *Phys. Earth Planetary Interiors* **128**, 51 (2001).

[3] J. Aubert, N. Gillet, and P. Cardin, Quasigeostrophic models of convection in rotating spherical shells. *Geophys. Geochem. Geosystems* **4**, article no. 1052 (2003).

[4] J. M. Aurnou and P. L. Olson, Experiments on Rayleigh-Bénard convection, magnetoconvection and rotating magnetoconvection in liquid gallium. *J. Fluid Mech.* **430**, 283 (2001).

[5] A. Azouni, E. W. Bolton, and F. H. Busse, Convection driven by centrifugal buoyancy in a rotating annulus *Geophys. Astrophys. Fluid Dyn.* **34**, 301 (1986).

[6] G. K. Batchelor , Computation of the energy spectrum in homogeneous two-dimensional turbulence. *Phys. Fluids Suppl. II* **12** 233 (1969).

[7] E. H. Bishop, R. E. Powe, and J. A. Scanlan, Natural convection heat transfer between concentric spheres. *Int. J. Heat Mass Transfer* **13**, 1857 (1970).

[8] S. I. Braginsky and P. H. Roberts, 1. Equations governing convection in Earth's core and the geodynamo. *Geophys. Astrophys. Fluid Dynamics* **77**, 3 (1995).

[9] B. A. Buffett, H. E. Huppert, J. R. Lister, and A. W. Woods, On the thermal evolution of the Earth's core. *J. Geophys. Res.* **101** 7989 (1996).

[10] F. H. Busse, Thermal instabilities in rapidly rotating systems. *J. Fluid Mechanics* **44**, 441 (1970).

[11] F. H. Busse, 3. Convective flows in rapidly rotating spheres and their dynamo action. *Phys. Fluids* **14**, 1301 (2002).

[12] F. H. Busse, Convective flows in rapidly rotating spheres and their dynamo action. *Phys. of Fluids* **14** 1301 (2002).

[13] R. Camussi and R. Verzicco, Convective turbulence in mercury: Scaling laws and spectra. *Phys. Fluids* **10** 516 (1998).

[14] P. Cardin and P. L. Olson, An experimental approach to thermochemical convection in the Earth's core. *Geophys. Res. Lett.* **19**, 1995 (1992).

[15] P. Cardin and P. L. Olson, Chaotic thermal convection in a rapidly rotating spherical shell: consequences for flow in the outer core. *Phys. Earth Planetary Interiors* **82**, 235 (1994).

[16] S. Cioni, S. Horanyi, L. Krebs, and U. Müller, Temperature fluctuation properties in sodium convection. *Phys. Rev. E* **56** R3753 (1997).

[17] C. R. Carrigan and F. H. Busse, Laboratory simulation of thermal convection in rotating planets and stars. *Science* **191**, 83 (1976).

[18] C. R. Carrigan and F. H. Busse, Convection induced by centrifugal buoyancy [Earth core]. *J. Fluid Mech* **62**, 579 (1974).

[19] C. R. Carrigan and F. H. Busse, An experimental and theoretical investigation of the onset of convection in rotating spherical shells. *J. Fluid Mech* **126**, 287 (1983).

[20] J. A. Chamberlain and C. R. Carrigan , An experimental investigation of convection in a rotating sphere subject to time varying thermal boundary conditions. *Geophys. Astrophys. Fluid Dyn.* **8**, 303 (1986).

[21] S. Cordero and F. H. Busse, Experiments on convection in rotating hemispherical shells: transition to a quasi-periodic state. *Geophys. Res. Lett.* **19**, 733 (1992).

[22] G. A. de Wijs, G. Kresse, L. Vocadlo, D. Dobson, D. Alfe, M. J. Gillian, and G. Price, The viscosity of liquid iron at the physical conditions of the Earth's core. *Nature* **392**, 805 (1998).

[23] A. M. Dziewonski and D. L. Anderson, Preliminary reference Earth model. *Phys. Earth and Planet. Interiors* **25**, 297 (1981).

[24] W. Gilbert, *On the magnet.*, first English ed. (London, 1900).

[25] N. Gillet and C. Jones, *personal comunication* (2004)

[26] N. Gillet, *personal comunication*(2004).

[27] G. A. Glatzmaier and P. L. Olson, Highly supercritical thermal convection in a rotating spherical shell: centrifugal vs. radial gravity. *Geophys. Astrophys. Fluid Dynamics* **70**, 113 (1993).

[28] J. P. Gollub, J. Clarke, M. Gharib, and O. N. Mesquita, Fluctuations and transport in a stirred fluid with a mean gradient. *Phys. Rev. Lett.* **67** 3507 (1991).

[29] S. Grossman and D. Lohse, Scaling in thermal convection: a unifying theory. *J. Fluid Mech.* **407** 27 (2000).

[30] S. Grossman and D. Lohse, Thermal convection for large Prandtl numbers. *Phys. Rev. Lett.* **86** 3316 (2001).

[31] S. Grossman and D. Lohse, Prandtl and Rayleigh number dependence of Reynolds number in turbulent thermal convection. *Phys. Rev. E* **66** Article No. 016305 (2002).

[32] D. Gubbins, The Rayleigh number for convection in the Earth's core. *Phys. Earth Planet. Interiors* **128**, 3 (2001).

[33] J. E. Hart, S. Kittelman, and D. R. Ohlsen, Mean flow precession and temperature probability density functions in turbulent rotating convection. *Phys. Fluids* **14** 955 (2002).

[34] K. Hata, Y. Takeuchi, M. Shiotsu, and A. Sakurai, Natural convection heat transfer from a horizontal cylinder in liquid sodium. Part 1. Experimental results. *Nuclear Engineering and Design* **193**, 105 (1999).

[35] M. Jaletzky, *PhD Dissertation*, University of Bayreuth (1999).

[36] P. Kelly and D. Gubbins , The geomagnetic field over the past 5 million years. *Geophys. J. Int.* **128** 315 (1997).

[37] R. H. Kraichnan , Inertial ranges in two-dimensional turbulence. *Phys. Fluids* **10** 1417 (1967).

[38] C. L. Johnson and C. G. Constable , Persistently anomalous Pacific geomagnetic fields. *Geophys. Res. Lett.* **25** 1011 (1998).

[39] S. Labrosse, J.-P. Poirier, and J.-L. LeMouël, On cooling of Earth's core. *Phys. Earth Planet. Int.* **99** 1 (1997).

[40] R. A. Langel and R. H. Estes, A geomagnetic field spectrum. *Geophys. Res. Lett.* **9**, 250 (1982).

[41] J. Larmor, How could a rotating body such as the sun become a magnet? *Brit. Assn. Adv. Sci. Rep.* **1919**, 159 (1919).

[42] S. Lorenzani and A. Tilgner, Fluid instabilities in precessing spheroidal cavities. *J. Fluid Mech.* **447**, 111 (2001).

[43] J.-B. Manneville and P. Olson , Banded convection in rotating fluid spheres and the circulation of the Jovian atmosphere. *Icarus* **122** 242 (1996).

[44] L. Marie, J. Burgette, F. Daviaud, and J. Leorat , Numerical study of homogenous dynamo based on experimental von Karman type flows. *Euro. Phys. J. B* **33** 469 (2003).

[45] G. D. Nastrom and K. S. Gage , A climatology of atmospheric wavenumber spectra of wind and temperature observed by commercial aircraft. *J. Atmos. Sci.* **42** 134 (1985).

[46] H.-C. Nataf, chapter 7 in book edited by C. Jones, A. Soward, and K. Zhang *Earth's core and lower mantle* (Taylor and Francis, London, 2003).

[47] R. W. Ohse, editor *Handbook of thermodynamic and transport properties of alkali metals.* (Blackwell Scientific, Oxford, 1985).

[48] P. L. Olson, chapter 1 in book edited by C. Jones, A. Soward, and K. Zhang *Earth's core and lower mantle* (Taylor and Francis, London, 2003).

[49] E. Plaut and F. H. Busse, Low-Prandtl number convection in a rotating cylindrical annulus. *J. Fluid Mech.* **464** 345 (2002).

[50] J.-P. Poirier, *Introduction to the Physics of the Earth's Interior* (Cambridge University Press, New York, 1991).

[51] S. B. Pope and M. R. Overholt, Direct numerical simulation of a passive scalar with imposed mean gradient in isotropic turbulence. *Phys. Fluids* **8** 3128 (1996).

[52] P. H. Roberts, On the thermal instability of a rotating- fluid sphere containing heat sources. *Phil. Trans. R. Soc. London A* **263**, 93 (1968).

[53] P. H. Roberts, chapter 5 in book edited by C. Jones, A. Soward, and K. Zhang *Earth's core and lower mantle* (Taylor and Francis, London, 2003).

[54] P. H. Roberts and G. A. Glatzmaier, Geodynamo theory and simulations. *Rev. Mod. Phys.* **72**, No. 4., 1081 (2000).

[55] B. I. Shraiman and E. D. Siggia, Heat transport in high-Rayleigh number convection. *Phys. Rev. A* **42** 3650 (1990).

[56] E. D. Siggia, High Rayleigh number convection. *Ann. Rev. Fluid Mech.* **26** 137 (1994).

[57] S. V. Starchenko and C. A. Jones, 1. Typical velocities and magnetic field strengths in planetary interiors. *Icarus* **157**, 426 (2002).

[58] K. R. Sreenivasan, The passive scalar spectrum and the Obukov-Corrsin constant. *Phys. Fluids* **8** 189 (1996).

[59] I. Sumita and P. L. Olson, A laboratory model for convection in Earth's core driven by a thermally heterogeneous mantle. *Science* **286**,1547 (1999).

[60] I. Sumita and P. L. Olson, Rotating thermal convection experiments in a hemispherical shell with heterogeneous boundary heat flux: implications for the Earth's core. *J. Geophys. Res.* **107**, ETG5-1-18 (2002).

[61] I. Sumita and P. L. Olson, Laboratory experiments on high Rayleigh number thermal convection in a rapidly rotating hemispherical shell. *Phys. Earth Planetary Interiors* **117**, 153 (2000).

[62] I. Sumita and P. L. Olson, Experiments on highly supercritical thermal convection in a rapidly rotating hemispherical shell. *J. Fluid Mech.* **492**, 271 (2003).

[63] S. T. Thoroddsen and C. W. Van Atta, Experiments on homogeneous turbulence in an unstable stratified fluid. *Phys. Fluids* **10** 3155 (1998).

[64] C. V. Tran and J. C. Bowman, On the dual cascade in two-dimensional turbulence. *Physica D* **176** 242 (2003).

[65] C. V. Tran and J. C. Bowman, Robustness of the inverse cascade in two-dimensional turbulence. *Phys. Rev. E* **69** Article No. 036303 (2004).

[66] P. Tsai, Z. A. Daya, S. W. Morris, Aspect-ratio dependence of charge transport in turbulent electroconvection. *Phys. Rev. Lett.* **92** Article No. 084503 (2004).

[67] K. K. Tung and W. W. Orlando, The k^{-3} and $k^{-5/3}$ energy spectrum of atmospheric turbulence: Quasigeostropic two-level model simulation. *J. Atmos. Sci.* **60** 824 (2003).

[68] Z. Warhaft, Passive scalars in turbulent flows. *Ann. Rev. Fluid Mech.* **32** 203 (2000).

[69] E. D. Williamson and L. H. Adams, Density distribution in the Earth. *J. Washington Acad. Sci.* **13**, 413 (1923).

[70] K. Zhang and G. Schubert, Magnetohydrodynamics in rapidly rotating spherical systems. *Annu. Rev. Fluid Mech.* **32**, 409 (2000).